AXIAL COLLAPSE OF THIN-WALLED, MULTI-CORNER SINGLE- AND MULTI-CELL TUBES

By

Ali Najafi

A Thesis
Submitted to the Faculty of
Mississippi State University
in Partial Fulfillment of the Requirements
for The Degree of Master of Science
in Aerospace Engineering
in the Department of Aerospace Engineering

Mississippi State, Mississippi

August 2009

AXIAL COLLAPSE OF THIN-WALLED, MULTI-CORNER SINGLE- AND MULTI-CELL TUBES

By

Ali Najafi

Approved:

Masoud Rais-Rohani Professor of Aerospace Engineering (Director of Thesis)	Mark F. Horstemayer Professor of Mechanical Engineering (Committee Member)
James C. Newman, Jr. Professor of Aerospace Engineering (Committee Member)	Thomas E. Lacy Professor of Aerospace Engineering (Committee Member)
Pasquale Cinnella Professor of Aerospace Engineering Graduate Coordinator of the Department of Aerospace Engineering	Sarah A. Rajala Dean of the Bagley College of Engineering

Name: Ali Najafi

Date of Degree: August 8, 2009

Institution: Mississippi State University

Major Field: Aerospace Engineering

Major Professor: Dr. Masoud Rais-Rohani

Title of Study: INVESTIGATION OF AXIAL COLLAPSE OF THIN-WALLED MULTI-CORNER TUBES MADE OF DUCTILE MATERIAL

Pages in study: 131

Candidate for Degree of Master of Science

Nonlinear explicit finite element (FE) simulations are used to study the axial collapse behavior of multi-corner. single- and multi-cell crush tubes under quasi-static and dynamic loading conditions. It is shown that the higher hardening modulus and yield stress increases the crush force and its resulting energy absorption. Moreover, the multi-cell tubes are found to have complicated collapse modes because of the geometrical complexity of the corner region unlike single-cell tubes. it was also shown that the stress wave propagation has a significant effect on the formation of crush modes in the tubes without imperfections whereas this effect can be ignored in tubes with imperfection or trigger mechanism. An analytical formula for the prediction of mean crush force of multi-corner multi-cell tubes is derived based on the super folding element theory. The analytical predictions for the mean crush force are found to be in good agreement with the FE solutions. Results also show a strong correlation between the cross-sectional

geometry and the crash behavior with the method of connecting the inner to the outer walls having large influence on the energy absorption.

DEDICATION

To My Beloved Parents and Sisters

ACKNOWLEDGMENTS

Foremost, I would like to express my sincere gratitude and appreciation to Dr. Masoud Rais-Rohani for the kind and enduring assistance and guidance through the course of this research.

I would like to express my appreciation to Dr. James C. Newman, Jr., Dr. Thomas E. Lacy, and Dr. Mark F. Horstemeyer for serving as graduate committee members. I would like to gratitude to Dr. Douglas J. Bamman for his exceptional lectures on continuum mechanics and finite deformation inelasticity. I would like to thank Dr. Christopher Eamon for his comments on the finite element simulations and for his nonlinear finite element class. I would like to thank Dr. Tomasz Wierzbicki for providing me his pioneer works and reports on this research topic. I was very fortunate to have Mr. Mohammad Rouhi as a friend and colleague. Our extensive discussions throughout this research inspired me a lot. I would like to thank Dr. Frank Abdi for giving me the opportunity to work with his research and development group in AlphaSTAR Corporation (ASC). Especially, I would like to thank Dr. Dade Huang and Mr. Mohit Garg in ASC. Additionally, I want to thank the Center for Advanced Vehicular Systems and Dr. Paul Wang for the resources and opportunities provided to me.

The funding provided for this study by the US Department of Energy under Grant No. DE-FC26-06NT42755 is gratefully acknowledged.

TABLE OF CONTENTS

LIST OF TABLES

LIST OF FIGURES

CHAPTER I

INTRODUCTION

Motivation

Safety is one of the most important criteria in design of vehicle structures. In general, a crashworthy vehicle must meet the impact energy management criteria that require the passenger compartment structure to sustain crash loads without excessive deformation while absorbing and dissipating the kinetic energy of impact. Some automotive structural components such as the side rails (figure 1.1) play a vital role in absorbing the bulk of impact energy in the full- and offset-frontal crash conditions (Chung 1996). With the goal of minimizing injury to the vehicle occupants, as defined by the head injury criteria (Mahmood 2000), the design of side rails requires a proper balance between intrusion distance and peak acceleration. While the component has to be stiff enough to limit intrusion, it has to accommodate sufficient plastic deformation to attenuate the impulsive force and associated acceleration transferred to the occupants. In addition, the requirement for energy absorption must be balanced by other design criteria such as weight efficiency.

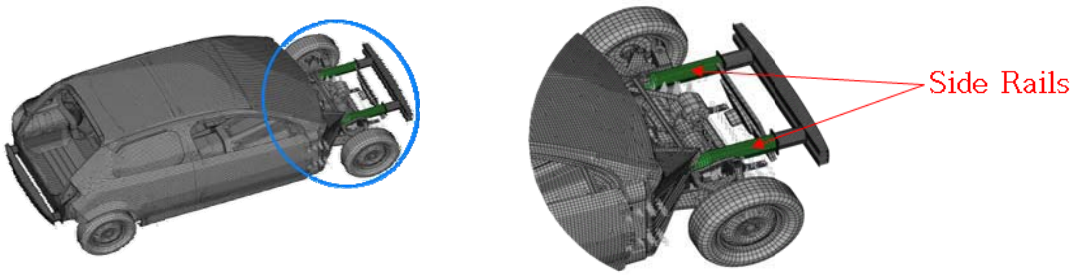

Figure 1.1

Side-rail of the PNGV design concept (Rais-Rohani 2006)

Aluminum alloys are extensively used in various forms, such as extrusion and forming, mainly because of their high strength-to-weight ratio. Due to the low density of aluminum alloys compared to steel, large amount of weight can be reduced by replacing the steel component with aluminum alloys. Therefore, in modern cars, aluminum alloys are employed in the front and rear bumper beams, side rails, longitudinal, and in other structural components such as pillars, frames, engine cradle, and chassis (Kokkula 2005). Besides the engineering properties of the material, the geometric attributes of the side rail can have a significant impact on its collapse characteristics. By controlling the form and rate of plastic deformation during impact, it would be possible to increase energy absorption and reduce peak acceleration. In its generic form, a side rail can be represented as a thin-walled prismatic tube whose geometric attributes are limited to its cross-sectional shape and dimensions. Since multi-corner tubes can serve as efficient energy absorbing components, a detail evaluation of the structural and material behavior of multi-corner tubes in both single- and multi-cell configuration would be beneficial. This is the main motivation for the present study.

Literature review

Over the past thirty years, numerous experimental, analytical, and numerical studies have been conducted to gain better understating of the crush mechanism of thin-walled tubular components and evaluation of their characteristics in terms of the buckling, mean crush force, folding deformation, and energy dissipation associated with progressive plastic collapse under static and dynamic axial compression. These studies have principally focused on prismatic tubes made of steel and aluminum alloys with some having foam-filled cavities (Chen 2001, Kim 2002, Abramowicz 2003, Karagiozova 2008, Jones 2003, Reid 1996).

Analytical methods originated from the pioneering works of Alexander (Alexander 1960) on cylindrical tubes and those of Wierzbicki, Abramovicz and Jones (Wierzbicki 1983, Abramowicz 1989, Jones 1983) on multi-corner tubes. Experimental studies by Abramowicz and Jones (Abramowicz 1984) on square tubes made of mild steel showed the existence of various crush mode shapes including two symmetric and two asymmetric modes. Motivated by the kinematics of crush observed in experimental studies, the analytical methods consider the mechanics of progressive collapse associated with the bending and membrane deformation in the component. Through careful examination of the collapsing response, Wierzbicki and Abramowicz (Wierzbicki 1983, Abramowicz 1989) proposed a super folding element (SFE) model whereby a corner portion of the cross-section is represented in terms of eighteen separate members whose characteristics are described in terms of the three principal folding mechanisms: *inextensional*, *quasi-inextensional*, and *extensional* deformations. The key aspect of SFE is the recognition of the formation and propagation of various hinge lines that define the boundaries of the

constituent members. SFE was used to predict the mean crush force of multi-corner tubes and to show that there is no considerable difference between the crush force in asymmetric and symmetric collapse modes (Abramowicz 1984). Jones (Jones 1998) also concluded that because of the small difference between the two different classes of mode shapes, either mode could occur in physical experiments. It is worth mentioning that wall thickness can also affect the crush mode (Reid 1986), (Lu 2003). Because of the difference in deformation patterns, tubular tubes with medium side-to-thickness ratio show a *compact* crush mode whereas in the thin-walled tubes, the mode is *non-compact* (Lu 2003).

Although both static and dynamic tests have been used to measure the collapse response of multi-corner crush tubes, the effect of dynamic load on the material properties is often ignored in analytical solutions. In 1989, Abramovicz and Weirzbicki (Abramowicz 1989) modified the SFE model to capture the strain rate effect in strain rate sensitive materials through the work of Calladine and English (Calladine 1984), which explicitly showed the relation between the initial velocity of impact and strain rate based on some engineering assumptions. They used the empirical relationship that was previously proposed by Symonds (Symonds 1965) based on testing of steel tubes at various strain rates. This phenomenological relationship, which modifies the yield stress for different strain rates, has also been incorporated into many nonlinear finite element analysis (FEA) codes such as LS-DYNA for including the effect of strain rate on classical plasticity models. Langseth and Hopperstad (Langseth 1996) performed extensive experiments on different heat-treated square aluminum tubes under both static and dynamic loadings, and showed that in static testing, most of the mode shapes are

symmetric whereas in dynamic cases, the mode shape tends to vary during the crush deformation. They also observed that the mean crush force for dynamic cases are higher than the static ones, and concluded that by introducing imperfection, the ratio between dynamic and static mean crush force can be kept constant. Hansen et al. (Hanssen 2000) experimentally showed that the dynamic effect, causing an increase in the mean crush force of strain-rate-insensitive aluminum, is because of inertial force arising from the acceleration of tube walls introduced by dynamic loading. In 1998, Jones (Jones 1998) classified the crush behavior into *static plastic buckling* (which considers the post-buckling of thin-walled tubes under static or quasi-static loads), *dynamic progressive buckling* (where all the crush progression is confined to one end of a dynamically crushed tube), and *dynamic plastic buckling* (where shell is wrinkled over the entire length). The last two classes of crush are distinguished by the initial impact velocity and the mass ratio between the impactor and the tube. Although the distinction between these two classes also depends on the material and geometric properties of the tube, the dynamic plastic buckling (Lindberg 1987) occurs for impact velocities higher than 100 m/s and mass ratio of 600. In most of the studies related to automotive crashworthiness, the behavior is in the range of dynamic progressive buckling due to the use of trigger mechanism. The problem is more complicated for tubes without trigger mechanism where there is interaction between elastic/plastic buckling, stress wave propagation and the folding initiation (Karagiozova 2004a,b).

By the late 1980's and the development of nonlinear FEA codes such as LS-DYNA and PAM-CRASH, it became possible to analyze the crash phenomenon (Abramowicz 2003,

Otubushin 1998) as a non-smooth, highly nonlinear problem based on the explicit time integration technique (Belytschko 2000). Most of the element models used in these codes originally developed by Belytschko et al. (Belytschko 2000) and Hughes et al. (Hughes 1981), (Hughes 2000) with subsequent modifications aimed at correcting the problem of zero energy (hourglass modes), enhancing the computational efficiency, and objectivity of stress rate, to pass a wide range of patch tests. In the case of contact-impact analysis for dynamic progressive buckling simulations, the penalty method is often used for rigid-body and self-contact calculations (Belytschko 1991) (Wriggers 2002). To include material nonlinearity, many previous studies have used classical elastic-plastic models with kinematic and/or isotropic hardenings (Simo 1998). These methods can also include the Cowper-Symonds (Symonds 1965) model to account for strain rate sensitive materials (Halquist 1998, 2006).

One way to control the crush zone and plastic deformation of tubes is through the design of multi-cell cross-sections. Component production using the extrusion process makes it possible to easily manufacture various prismatic components with multi-cell, multi-corner cross-sectional configurations. Previous studies by Santosa (Santosa 1997, 1999), Chen and Wierzbicki (Chen 2001), Kim (Kim 2002), and Zhang, et al. (Zhang 2006), (Zhang 2007) show that multi-cell rectangular profiles with more corners can enhance the energy absorption capacity of tubes. Chen and Wierzbicki (Chen 2001) modified the mean crush force formulation of simple multi-cell rectangular tubes to account for the addition of foam material used to fill the open spaces inside the tube. Their method resulted in an analytical equation for the mean crush force based on the division of the cross-section into a number of flange elements, the cross sectional area,

and the plastic flow stress. Their results indicated that the foam-filled tubes generally had (~30%) higher specific energy absorption (SEA) than the corresponding empty-cell tubes while the addition of interior walls (double and triple cell models) increased the SEA value by about 15% in comparison to the single cell model. Zhang et al. (Zhang 2006, 2007) introduced a simple and efficient way for mean crush force calculations based on SFE deformation results obtained from FE simulations. They divided the multi-cell rectangular cross section into a number of 2-flange corners, 4-flange cruciform, and 3-flange T-shaped elements, and estimated the combined contributions of these elements to the internal energy and the mean crush force. Zhang and Suzuki (Zhang 2005) studied the effect of different types of longitudinal and transverse stiffening of square tubes. They also developed an equation for mean crush force by accounting for stiffener effects and modifying the thickness parameters appearing in previous studies.

Multi-cell tubes can serve as energy absorbing components in automotive structures. However, there have been very few studies on the energy absorption characteristics of multi-corner multi-cell tubes. In this research, the mechanics of crush in single-cell columns is investigated in detail. By increasing the demand of lightweight and crashworthy material in automotive industries, a detail understanding of the deformation and its effect on the energy absorption mechanism is investigated here. The effect of inelastic behavior is examined numerically. Both quasi-static and dynamic loading are considered in this investigation and the main differences are pointed out. In dynamic loading conditions, the relation between crush mode and basic mechanism of energy absorption in multi-cell tubes is investigated. Crush mode resulting from the imperfection or stress wave propagation and the resulting relation between folding modes and energy

absorption are described. Based on the observation of deformation mode in finite element analysis, analytical equation for multi-corner multi-cell tubes with acute and obtuse corner angles is developed and results are compared with finite element analysis.

Terminology of crush response

Figure 1.2 depicts the crush response of axially loaded prismatic energy absorbing components and the list of key parameters that will be used in the proceeding chapters. The energy absorption behavior of a crush tube can be represented by the plot of crush force (P) versus crush distance δ. As shown in the figure, the effective crush distance, δ_{eff} is the total crush distance such that any further deformation requires a substantial increase in the force as material behaves as a rigid bulk. The total energy absorbed in this process E_{int}can be calculated by integration of the area under the load displacement curve up to δ_{eff}. The mean value of crush force, $P_m$can be calculated from the ratio of internal energy by effective crush distance.

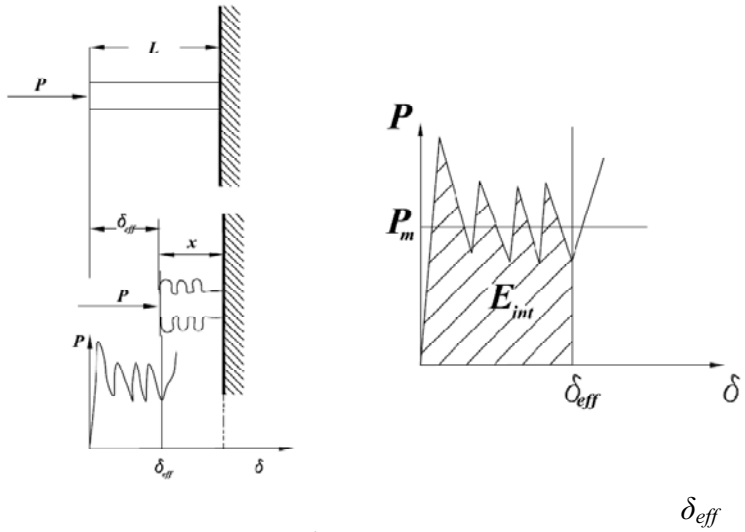

Figure 1.2

Axial crush response of thin-walled tubes

Figure 1.3(a) shows a typical deformation pattern of an axially crushed square single-cell thin-walled tube. Deformation mode can be identified by cutting a corner section as shown in figure 1.3(b). The deformation pattern can be explained by two major modes: asymmetric and symmetric as shown in figures 1.3(c) and 1.3(d). Asymmetric mode occurs when two webs joined at a corner collapse asymmetrically such that one web is deformed inward while the other is deformed outward. In symmetric mode, both webs are deformed outward and form a symmetric pattern with respect to the corner line. In some cases, these modes can be mixed and create a complex shape as will be described in subsequent chapters.

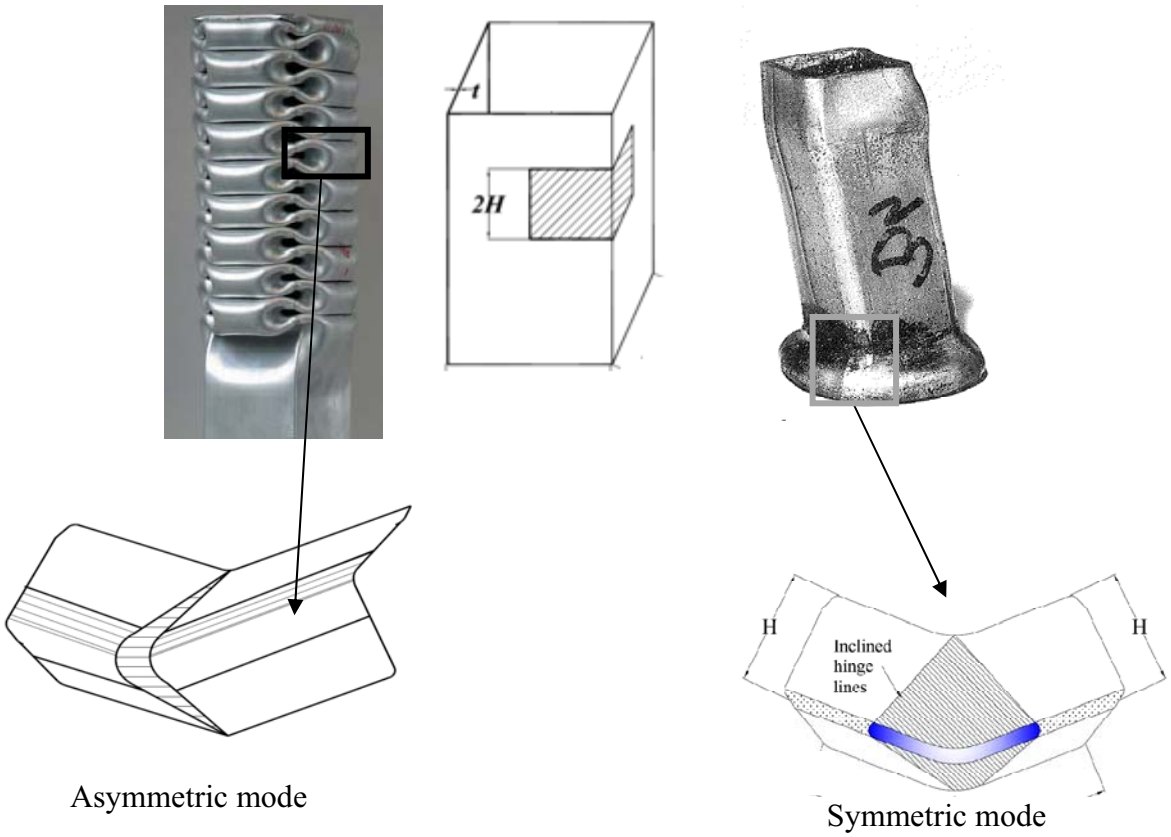

Figure 1.3

General deformation pattern of axially compressed tube

Scope of present study

The objective of this thesis is to study the basic factors that can affect the energy absorption behavior of multi-corner crush tubes including cross-sectional geometry under both quasi-static and dynamic loading conditions. Both numerical and analytical study are performed, with the former conducted using explicit code LS-DYNA.

The content presented in this thesis includes: the description of a series of quasi-static FEA simulations in chapter 2 to analyze the influence of material behavior, failure, contact definition, element formulation, trigger mechanism, and crush force for a number

of simple square tubes. Since the performance of energy absorbing components is usually more crucial under dynamic loads, the effect of dynamic loads is also investigated based on two loading cases corresponding to a constant velocity and a time varying velocity condition.

In chapter 3, the effect of cross-sectional geometry on the crush characteristics of multi-corner, multi-cell tubes is discussed. In all of the previously cited investigations, the cross-sectional shapes considered were limited to either single cell (circular, rectangular, hexagonal, or rhomboidal) or multi-cell tubes with identical (rectangular or hexagonal) cell properties, whereas this study investigates multi-cell tubes with more complicated multi-corner shapes including the combination of acute, obtuse and right angles as well as multiple nonidentical flanges (Najafi 2008).

In chapter 4, SFE model of Abramowics and Wierzbicki (Abramowicz 1989) is extended and its extension (Jones 1983), Wierzbicki 1983, Hayduk 1984, Wierzbicki 1994a, Wierzbicki 1994b) to investigate the crush characteristics of multi-cell tubes consisting of three different types of three-flange elements characterized by a combination of two-angle corners with either two obtuse or two acute angles separating the three flanges. A closed form equation for prediction of mean crush force is developed. The values of mean crush force based on different analytical equations as well as FEA simulations are compared.

Chapter 5 contains thesis summary and conclusions along with some recommendations for future work.

CHAPTER II

FINITE ELEMENT ANALYSIS OF SQUARE TUBES UNDER AXIAL COMPRESSION

Progressive collapse of thin-wall structures is a complex problem with many physical interactions. Most of the experimental studies conducted previously have tried to find a way to decouple and simplify the collapse response and develop a theory to describe the physics of energy absorption (Hiermaier 2008). The complexities are mainly due to the dynamic properties of material, material failure behavior, buckling instability in thin-walled structures, contact due to impact, contacts between adjacent folds, the boundary and initial condition of the problem and geometrical properties. Dynamic behavior of the material is a very complicated area of research which includes the physics of solids, atomistic structure and dislocation dynamics, grain size and orientation, and many other physical and microstructural based phenomena. Examination of a material from macroscopic point of view shows that most of the macroscopic properties such as hardening, recovery, strain rate sensitivity, yield point. are contributing to the overall behavior of energy absorption of structures. Computational implementation of even a basic phenomenological model can be very complicated when considering rate

sensitivity, temperature, yield mechanism and anisotropy. Buckling instability in the thin walled structures imposes additional difficulty, especially in dynamic cases due to the presence and interactions of the elastic and plastic waves (Karagiozova 2008). The purpose of this chapter is to review some key theoretical features in nonlinear FEA that are applicable to the analysis of energy absorbing components such as crush tubes. The FE simulation of square single-cell tubes using LS-DYNA is discussed below.

2.1 Boundary value problem in structural mechanics

The solution of a boundary/initial value problem requires a model of a structure with known material properties and behavior along with certain loading and boundary conditions. The transformation of the physical problem to a well defined mathematical problem requires rational assumptions and simplifications that lead to ordinary or partial differential equations governing the behavior of the idealized structure. The numerical approaches used to solve these differential equations in the context of finite element analysis involve numerical approximations that can result in numerical errors. Some of these errors can be minimized by using a more accurate element formulation, refining the mesh, and adjusting time steps, all of which tend to increase the simulation time. A common practice to check and verify the finite element results is to repeat the analysis with different mesh size and time step in the transient dynamic FEA in search of a model where all the results tend to converge.

To solve a boundary value problem such as crushing of a thin-walled tube, kinematic and kinetic relations, thermodynamic principles, and constitutive equations needed as summarized below:

- Kinematics, including the definition of deformation gradient and the relation between strain and displacement

$$E = \frac{1}{2}(F^T F - I) \tag{2.1}$$

where F and I are deformation gradient and 2nd rank identity tensor respectively.

- Balance laws

The conservation of mass states that the mass in a closed system stays constant and for the Lagrangian formulation (Holzapfel 2000)

$$\rho_0 = \det F \, \rho \tag{2.2}$$

where ρ_0 and ρ are density in reference and current configurations, respectively.

The Eulerian balance of linear momentum and the balance of angular momentum are shown in equation 2.3 and 2.4, respectively

$$div\, \sigma^T + \rho b - \rho \dot{v} = 0 \tag{2.3}$$

$$\sigma = \sigma^T \tag{2.4}$$

where σ, b and v are stress, body force and velocity, respectively. Equation 2.4 shows that stress matrix is symmetric.

- Thermodynamic principles

Because of the isothermal adiabatic assumption, the heat equation will be ignored in this study and, the fist law of thermodynamics in current configuration is written as

$$\rho \dot{e} = \sigma^T (grad \boldsymbol{v}) \tag{2.5}$$

where $\dot{e}$ is the rate of internal energy

Due to the assumption above, the second law of thermodynamics can be written as

$$-\rho \dot{\psi} + \sigma L \geq 0 \tag{2.6}$$

where ψ is the free energy that shows the energy available for work. In the isentropic process, $\psi = e$

- Constitutive equations

In this study, the constitutive models are multi-linear isotropic hardening model with J2 plasticity. The linear form of the model is described below (Simo 2000)

$$\sigma = E(\varepsilon \quad - \varepsilon_p) \tag{2.7}$$

$$f(\sigma, \alpha) = |\sigma| - [\sigma_Y + K\alpha] \tag{2.8}$$

$$\dot{\varepsilon}_p = \gamma \, sign\,(\sigma) \tag{2.9}$$

$$\dot{\alpha} = \gamma \tag{2.10}$$

$$\frac{\sigma_y}{\sigma_r} = \left(1 + \frac{\dot{\varepsilon}}{D}\right)^p \tag{2.11}$$

where equation 2.7 shows the stress-strain relationship for elastic part, equation 2.8 represents the yield surface with linear isotropic hardening variable K. Equations 2.9 and 2.10 shows the flow rule and 2.11 is the Cowper-Symonds strain rate relations (Symonds 1965).

These equations become 19 unknowns and 19 equations for a three dimensional elastic body; and for simple constitutive equation, as previously described, the number of unknowns and equations become more. This system of differential equations should be solved in conjunction with appropriate initial and boundary conditions.

A single governing equation can be obtained by substituting the above equations into the momentum equations. The momentum equation cannot be discretized directly by finite element method. The finite element model representing the body contains a finite number of degrees of freedom, and the implication is that the requirement for equilibrium

cannot be satisfied exactly at every point in the continuum (in which is called the strong sense). In order to discretize this equation, a weak form or virtual form is needed. Weak formulation of equilibrium is used where global equilibrium for the body as a whole is imposed even though this does not necessarily ensure pointwise equilibrium (Dunne 2005). The principle of virtual work or virtual displacement, which is equivalent to the momentum equation and traction boundary condition is used as the basis of the FEA in displacement based analysis of solids. The derivation of this equation and the detail descriptions appears in many finite element text books (Reddy 1993, Bathe 1995, Hughes 2000). The discrete equations are derived from the principle of virtual work by using finite element interpolation functions for the test and trial functions. Most of the problems in solid mechanics are based on Lagrangian mesh. The momentum equation resulting from this discretization can be written in the form

$$M\ddot{u} = f^{ext} - f^{int} \tag{2.12}$$

One way to solve this problem is through the explicit time integration method. The most widely used explicit method is the central difference method with a diagonal or lumped mass matrix (Belytschko 2000). Diagonal mass matrix helps to reduce the computational cost of inverting the mass matrix. Starting at time t=0, acceleration, velocity and displacement can be calculated based on this method.

2.2 Explicit solver

The selection of integration method depends on the type of partial differential equation (PDE), the smoothness of the data and the response of interest. For parabolic PDEs, implicit methods are generally preferred (Belytschko 2000). In the case of collapse problem, the equations of the shell elements, which are the main focus in our study, are

parabolic (Belytschko 2000). However, explicit methods are preferred here because of the noise introduced by contact-impact problems. Although explicit methods are guaranteed to converge, they are only conditionally stable which means that they are time-step dependent. (Hughes 2000). The stable time step in a parabolic system decreases by a factor of four each time the size of the smallest element is reduced by 50% (Belytschko 2000). Therefore, the element refinement in an explicit method makes the analysis very expensive. The time step size for shell element in LS-DYNA is calculated using equation (2.13) (Halquist 2006)

$$\Delta t = \frac{L_s}{c} \tag{2.13}$$

where L_s is the characteristic length, and c is the speed of sound given by

$$c = \sqrt{\frac{E}{\rho\,(1-\upsilon^2)}} \tag{2.14}$$

where *E, ρ,* and *ν* represent the elastic modulus, material density and Poisson's ratio, respectively.

In the default mode, the characteristic length L_s is given by

$$L_s = \frac{(1+\beta)\,A_s}{max(L_1,L_2,L_3,(1-\beta)\,L_4)} \tag{2.15}$$

where $\beta = 0$ is for quadrilateral and $\beta = 1$ for triangular shell elements, A_s is the element area, and L_i is the length of the sides defining the shell elements with i varying from 1 to 4.

2.3 Contact algorithm-constraint implementation

Besides the system nonlinearity due to deformation, strain and material behavior, contact is another source of nonlinearity that can be observed in a boundary value

problem. In the axial collapse process, there are two main forms of contact, one between the striker (impactor) and the tube and another between one portion of the tube and another (self contact) due to extensive deformation. Contact interface basically is a motion constraint equation. There are four conventional methods for treating a constraint such as penalty function method, Lagrange multiplier, augmented Lagrangian, and perturbed Lagrangian methods, all of which originate from optimization theory. Most of the finite element codes including LS-DYNA use the penalty function method as their default contact formulation due to the simpler implementation. In penalty function method, a penalty term is added to the energy equation (Wriggers 2002). The energy equation for a simple mass-spring system in figure 2.1 is defined as below:

$$\Pi(u) = \frac{1}{2}Ku^2 - mgu + \frac{1}{2}\epsilon\,(\mathbf{c}(u))^2 \tag{2.16}$$

where K, m, u, g, ε and **c**(u) are the actual spring stiffness matrix, mass, translational deformation of the system, gravitational acceleration, penalty stiffness parameter and constraint equation, respectively. This additional energy term treats contact as an active constraint and has been defined as the strain energy of fictitious springs between two contact boundaries. This penalty parameter is defined as the stiffness of the rigid wall in LS-DYNA (Halquist 2006).

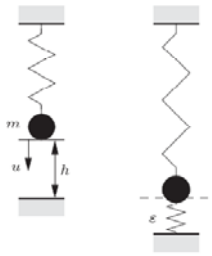

Figure 2.1

Point mass supported by a spring and a penalty spring due to the penalty term (Wriggers 2002).

The key condition in contact calculation, which is the condition of impenetrability, cannot be expressed by simple equations. In explicit solvers, this condition is expressed in the rate form (Belytschko 2000). In the case of contact between a rigid surface and a flexible one, the contact force represents an important response for energy absorption analysis. In the penalty function method, the contact force for the spring-mass system shown in figure 2.1 is calculated as

$$R_N = \epsilon \left(c(u)\right) = \frac{\epsilon}{\epsilon+K}(Kh - mg) \tag{2.17}$$

where h is the initial distance between two contacting boundaries (figure (2.1)).

Because the stiffness of rigid wall is assumed to be higher compare to spring stiffness, the penalty stiffness parameter reaches one of the extreme conditions $\epsilon \rightarrow \infty$ and contact force is not depend on the penalty stiffness parameter. Therefore, the contact force calculation is considered to be a proper measure for energy absorption characterization.

Other important feature of contact algorithm is the condition of impenetrability between different folds in the tube that is called self contact. This feature can be implemented using single surface definition in LS-DYNA (Halquist 2006).

2.4 Quasi-static simulation of square tubes

In the quasi-static loading simulation, a tube is held fixed at its base and a linear incremental displacement is applied at the other end as shown in figure 2.2. The contact friction coefficient between the rigid wall and tube is set at 0.3 to prevent slippage between two surfaces. A preliminary analysis showed that the friction coefficient between wall and tube does not influence the energy absorption behavior.

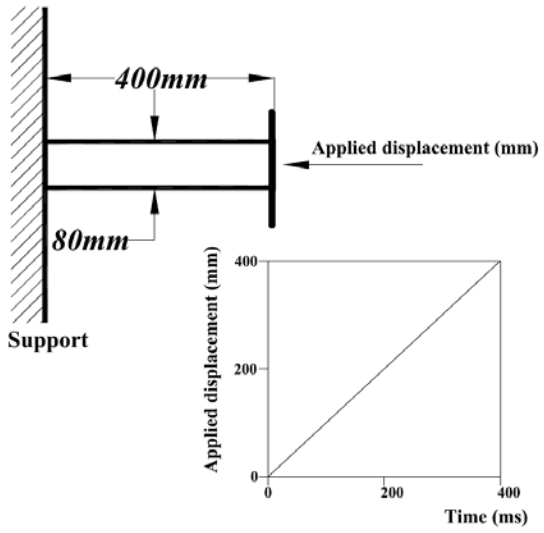

Figure 2.2

Quasi-static model setup

To prevent element-element penetration due to excessive deformation, a frictionless self-contact condition is used all for the element surfaces. The crush tube material is selected to be aluminum with the physical properties of (E = 70 GPa, υ= 0.3, and ρ = 2.7e-6 kg/mm3). The material behavior is expressed in terms of true stress-true strain curve, which is extracted from tension test up to ultimate stress. Since there is no failure and damage defined in this model, the material is assumed to be perfectly plastic after

ultimate stress. J_2 plasticity linear/multi-linear isotropic hardening material model is used such that the stress-strain curve is divided into a number of linear isotropic hardening models.

Element density study is performed to obtain an optimum mesh density for the models investigated. Because of the high distortion in elements, zero energy deformation or hourglass energy [Belytschko 2000] is calculated for element performance check. Results show a very small non-physical hourglass energy which is less than 2% of the total internal energy.

The FE models used here are developed using the ANSYS-preprocessor with FEA simulations performed using transient dynamic nonlinear explicit FE code LS-DYNA. All simulations are conducted on 16 nodes of RAPTOR, a 2048 processor cluster composed of 512 Sun Microsystems SunFire X2200 M2 servers, each with two dual-core AMD Opteron 2218 processors (2.6GHz) and 8 GB of memory (for a total of 4TB) at Mississippi State University. The post-processor LSPREPOST is used for visualization and data acquisition. To filter out noise in the simulation results, the SAE type filtering with the frequency of 60 Hz has been used. The termination time has been specified at 400 ms for all the cases considered for quasi-static analysis which resulted in the 1mm/ms constant velocity axial loading on the tube.

Prior to establishing a baseline model for investigating the crush characteristics of multi-cell tubes, the effect of element type on collapse response of a simple square tube model needs to be investigated first. Based on these results an appropriate element formulation will be selected for all the subsequent simulations.

2.4.1 Effect of shell element formulation

The square tube's cross-sectional dimension is 80 mm with wall thickness of 2 mm and length of 400 mm. The rate sensitivity effect is totally ignored in this analysis as the material considered here (i.e. aluminum alloy) is almost rate insensitive. True stress-true strain curve for AA6060-T6 (de Kanter 2006) used in this analysis is shown in figure 2.3. The number of integration points through the thickness is set to three for all the shell element formulations. In order to obtain a stable crush pattern, a trigger mechanism, in the form of two small symmetric indentations is placed at 15mm from the free edge (impacted end) of the tube. The effect of trigger mechanism will be discussed later in this chapter.

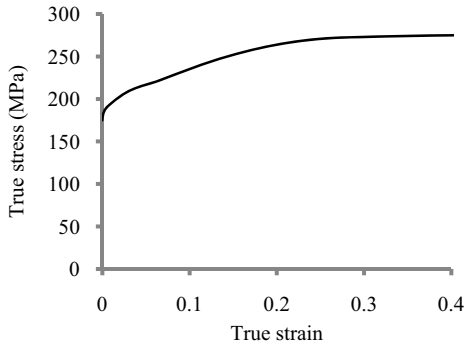

Figure 2.3

True stress-true strain curve for AA 6060-T6 (de Kanter 2006)

The available shell elements in LS-DYNA as identified in table 2.1 are examined. However, only the plots of in this section, the result of those elements that produced converged throughout the simulations has been reported. Figure 2.4 shows crush force versus crush distance using different element formulations. The termination times for

these analyses are also reported in each plot. The crush behaviors of the EF1, EF2, and EF16 are fairly similar and follow the same pattern as that observed in experiments (Abramowicz 1984, Otubushin 1998, DiPaolo 2004, Dipaolo 2006). Other element formulations including EF7, EF8, EF10, and EF11 show the different patterns of crush behavior, which are not acceptable. Further analysis has shown that despite the accuracy of fully integrated element (EF16), it is computationally expensive and unstable in all the loading conditions considered here. Hence, for the purpose of quasi-static simulation, EF1 and EF2 have acceptable performance.

Table 2.1

List of shell elements investigated in this study.

LS-DYNA Element Formulation	Name	Properties
EF1	*Hughes-Liu*	Degeneration of 8-node brick, incrementally objective, uniformly reduced integration, nonplanar geometry, one point quadrature
EF2	*Belytschko-Tsay (Lin)*	Computationally efficient, 5 through-the-thickness integration points, co-rotational coordinates and rate of deformation formulation, hourglass viscosity, nonplanar geometry, Hughes-Liu mass matrix
EF6	S/R Hughes-Liu	Selectively reduced integration near boundary and point loads to prevent hourglass, nonplanar geometry
EF7	*S/R co-rotational Hughes-Liu*	Similar to EF6 using co-rotational coordinate system from Belytschko-Tsay
EF8	*Belytschko-Leviathan*	Modified Belytschko-Tsay for passing the patch test, physical hourglass control
EF10	*Belytschko-Wong-Chiang*	Perfectly planar geometry
EF11	*LS-DYNA*	Fast co-rotational Hughes-Liu (EF1)
EF16	*LS-DYNA*	Fully integrated shell

The Hughes-Lu shell element formulation (EF1) has four in-plane integration points. It uses the selectively reduced integration technique and has hourglass control for the mode of zero energy (Halquist 1998). Because of the severe bending in the model, the stress and strain variations through the thickness are important factors for energy absorption calculation. As a result of this investigation, EF1 is used for the subsequent simulations.

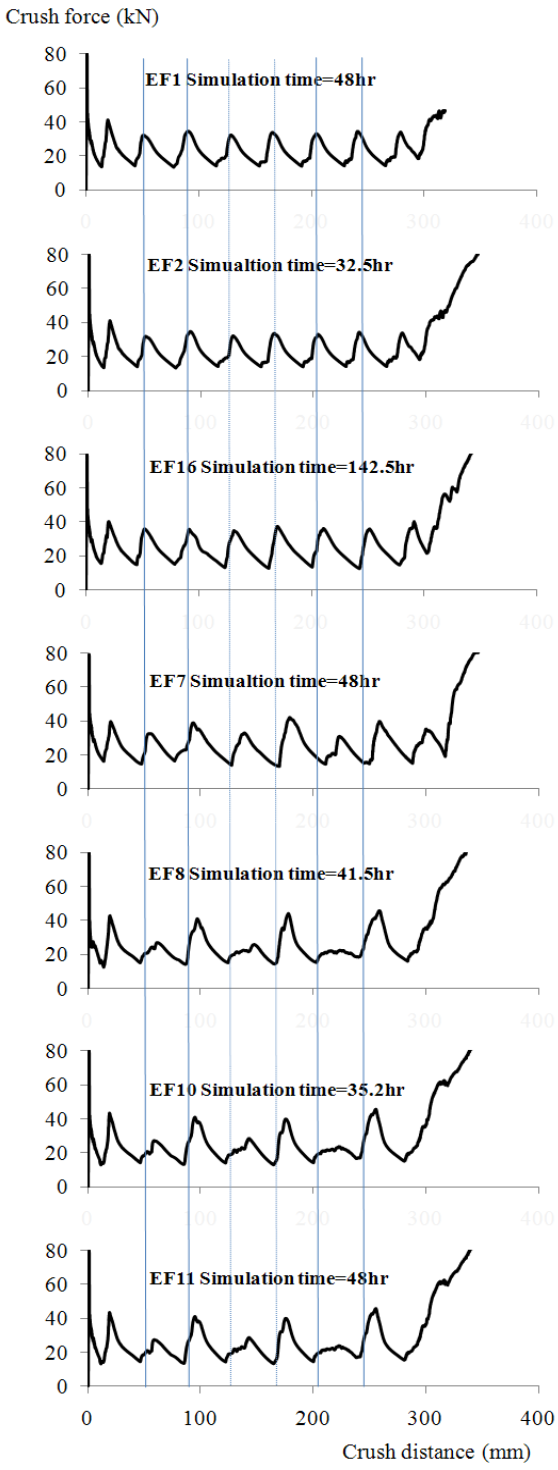

Figure 2.4

Crush force-crush distance variation for different shell element formulations in LS-DYNA

In shell-element models, responses are calculated at the defined integration points located at different locations through the shell thickness. Generally, the more integration points the more accurate the stress and strain predictions. In this study, four different integration point (NIP) cases have been studied to find the optimum number of integration points through the thickness. The plots of crush force versus crush distance for different NIP values are shown in figure 2.5. As far as the crush response is concerned, there is no noticeable improvement in accuracy as a result of increasing NIP. However, there is a nonlinear increase in the computational time. Hence, three integration points are used for subsequent simulations. However, in some case in order to reduce the computational time, two integration points are used for some of the simulations.

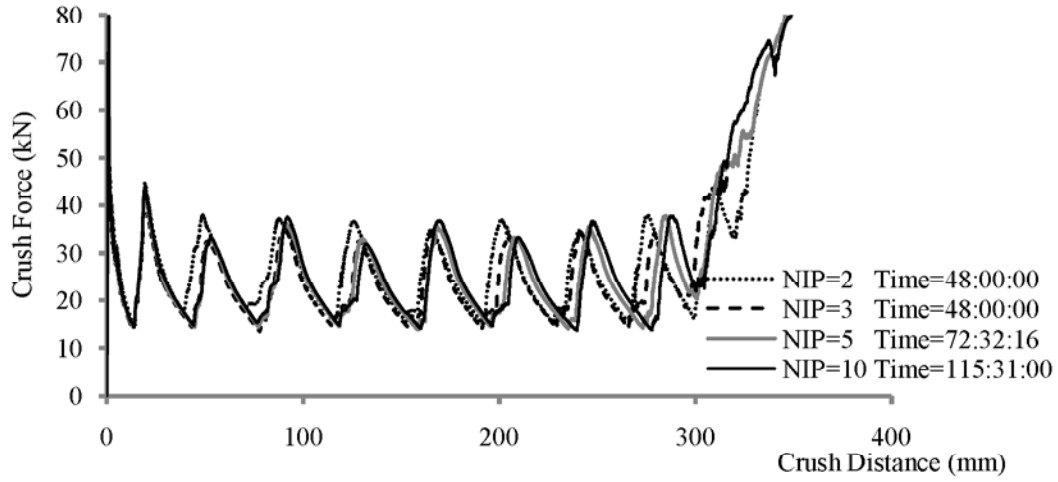

Figure 2.5

Effect of the number of integration points (NIP) in Hughes-Liu element (EF1) on the crush response

2.4.2 Effect of trigger mechanism

Trigger mechanism is used to lower the initial peak crush force, induce a stable progressive failure, and avoid the global bending of the tube as it is crushed. In this study, a simple trigger mechanism in the form of small indentation on two opposite walls is used. This is referred to as an asymmetric trigger mechanism because it induces the asymmetric mode shape as will be discussed in chapter 4.

Two integration points through the shell element thickness is used in this analysis. The stress-strain curve used here is illustrated in figure 2.6. The location of the indentation trigger relative to the impacted end of the tube is varied from 5 mm to 30 mm with the effect on the crush force dissipation shown in figure. 2.7. It is clear that the addition of indentation trigger reduces the initial peak force while stabilizing the deformation as indicated by the shapes of the curves and asymmetric mode shape. The trigger location offsets the load-displacement curve according to its position, but it does not change the mean crush force and the crush force fluctuation frequency considerably. However, it is important to note that the crush distance can be affected slightly when the trigger distance is reduced. For the trigger distances of 15mm and 30mm, the effective crush distance stays the same. Since the folding distance of 30mm is higher than the length of a crushed corner element (figure 1.3) of the tube, the number of peak loads through the crush process reduces. For the future simulations, the trigger distance of 15mm will be used. It is worth noting that in order to obtain a steady crush behavior, the location of trigger should be close to the stationary point of the buckling wave of the wall. In this case, the trigger distance of 15 mm is closer to the actual horizontal hinge lines appeared in the structure.

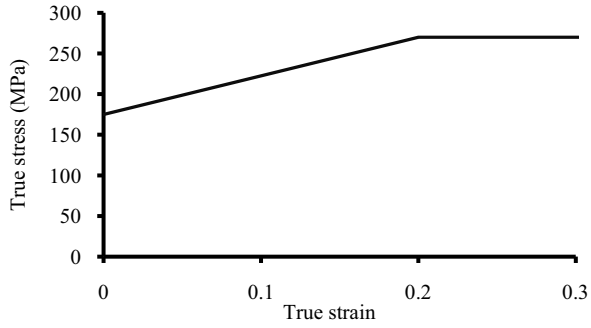

Figure 2.6

Stress-strain curve for the study of trigger mechanism

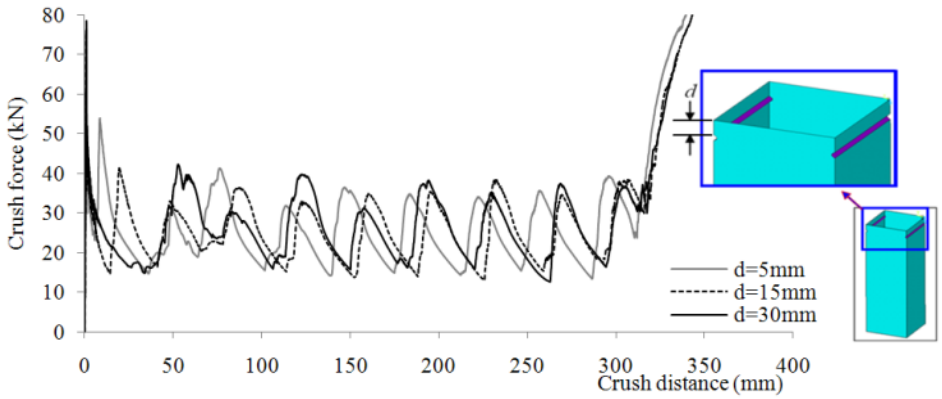

Figure 2.7

Effect of trigger distance on crush response

2.4.3 Effect of tangent modulus

The inelastic behavior of the material is represented by a rate-independent linear hardening law (figure 2.8). In order to keep the same toughness for different hardening slopes, a failure strain, ε_f has been defined in the model (figure 2.8). Two integration points are used through the shell thickness for this analysis. Figure 2.9 shows the effect of

hardening on the crush response of the tube. Crush force increases by increasing material hardening. Increasing the hardening by 50% causes a 15% improvement in the mean crush force.

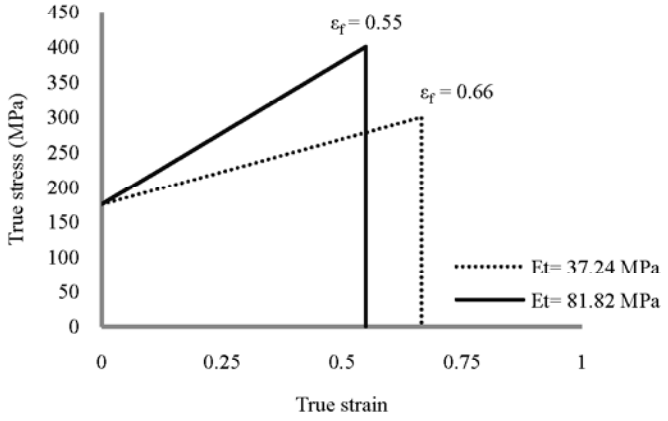

Figure 2.8

Stress-strain curve used for the study of tangent modulus

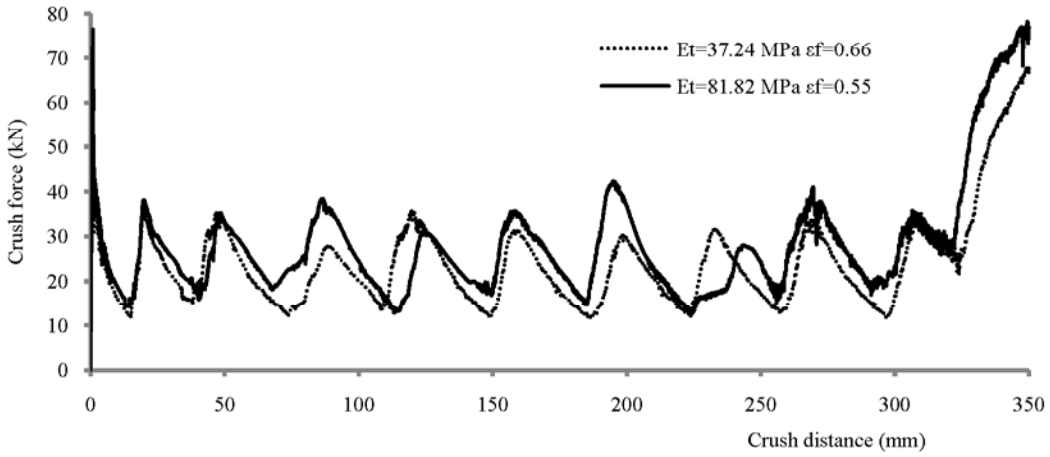

Figure 2.9

Effect of tangent modulus on crush response

2.4.4 Effect of toughness

The Hughes-Lu shell element formulation (EF1) has four in-plane integration points. It uses the selectively reduced integration technique and has hourglass control for the mode of zero energy (Halquist 1998). Because of the severe bending in the model, the stress and strain variations through the thickness are important factors for energy absorption calculation. As a result of this investigation, EF1 is used for the subsequent simulations.

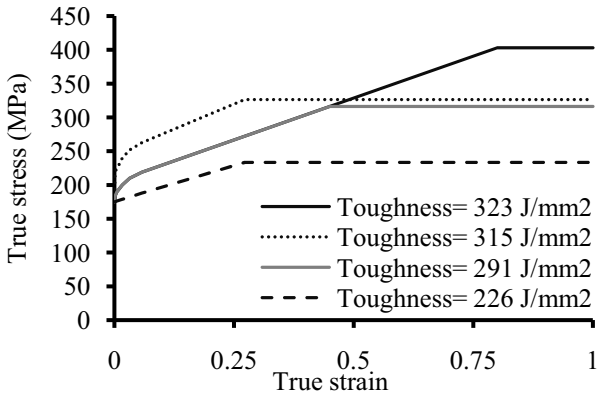

Figure 2.10

Stress-strain curves used for toughness study

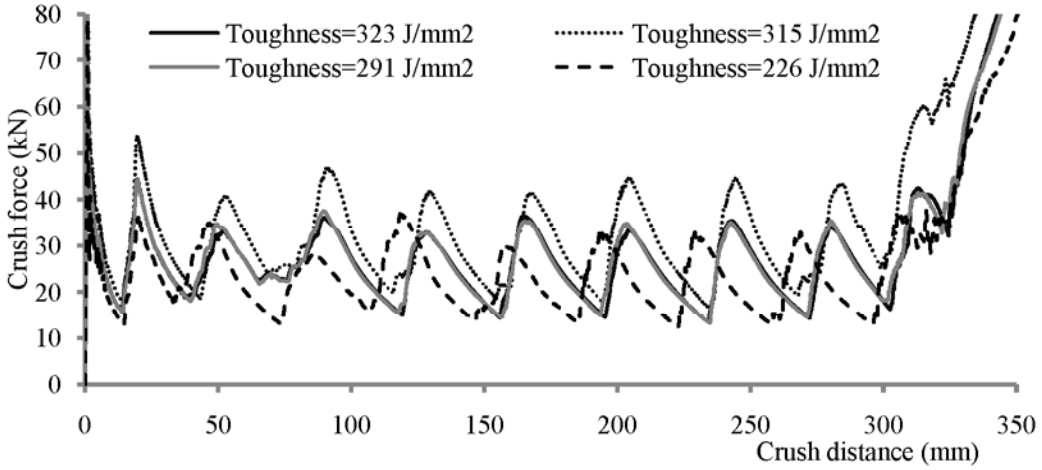

Figure 2.11

Effect of material toughness on crush response

2.4.5 Effect of strain to failure

Since the plastic strain in the collapse of thin-walled prismatic tubes is high, the stress-strain behavior of the material has a considerably more effect on energy absorption.

In order to decompose different stress-strain behavior parameters such as hardening slope and toughness, the maximum allowable amount of strain that can occur in the structure should be controlled by using a strain-to-failure criterion. Maximum strain at each integration point through the shell thickness will be monitored, and when it reaches the failure value, that element was removed from the analysis. The number of integration points in this analysis is chosen to be ten, although this makes the simulation very expensive. The energy absorption behavior of the tube is illustrated in figure 2.12. Failure strains in the range of 0.2 to 2.0 were used. It is seen that the failure strains of 0.2 and 0.3 cause failure in the tube. Though, as shown in figure 2.12, the energy absorbed in this case is due to the plastic bending of each disconnected walls individually (figure 2.13).

Since the element with high strain values can be highly distorted, the simulation can halt prior to the assigned termination time for the solver. To remove this deficiency, the highly distorted shell elements are removed from the model. Because of this criterion and neglecting the fracture energy of the splitting process, the resulting of shell splitting does not accurately capture the energy absorption characteristics. However, this form of failure has been observed in some similar cases in literature experimentally (Lu 2003). In order to have a more accurate energy absorption study in this case, the failure should rigorously be taken into account. The result of the effect of failure strain as one parameter for failure also shows that with the failure strain of 30% and higher, the failure strain does not have any considerable effect on the energy absorption characteristics of the model.

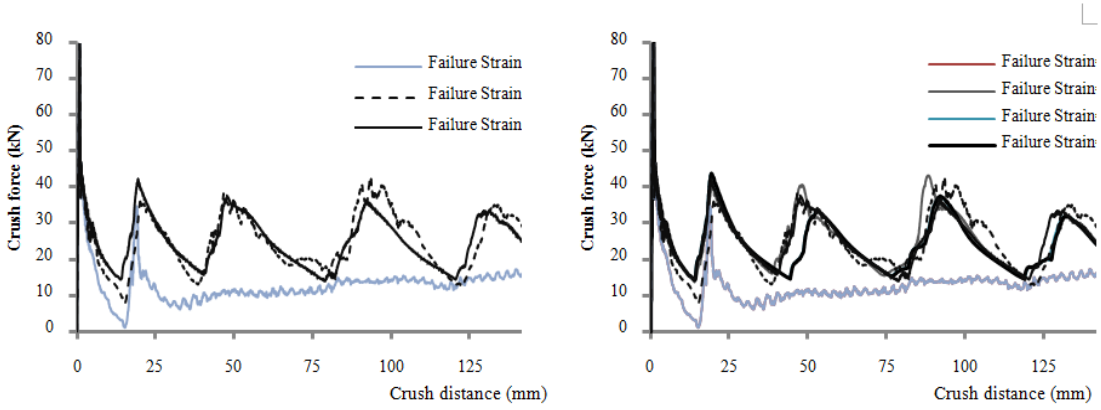

Figure 2.12

Effect of failure strain value on the energy absorption behavior

One advantage of asymmetric mode shape is that in the case of failure and splitting the crush tube will be deformed in a way that can preserve its energy absorption properties. However, in some design cases, this failure is not desirable and should be avoided. Figure 2.13 shows the deformation shape of the failed tube under compression. It can be seen

that two opposite walls deform inward toward the center line of the tube while the other two walls deform outward.

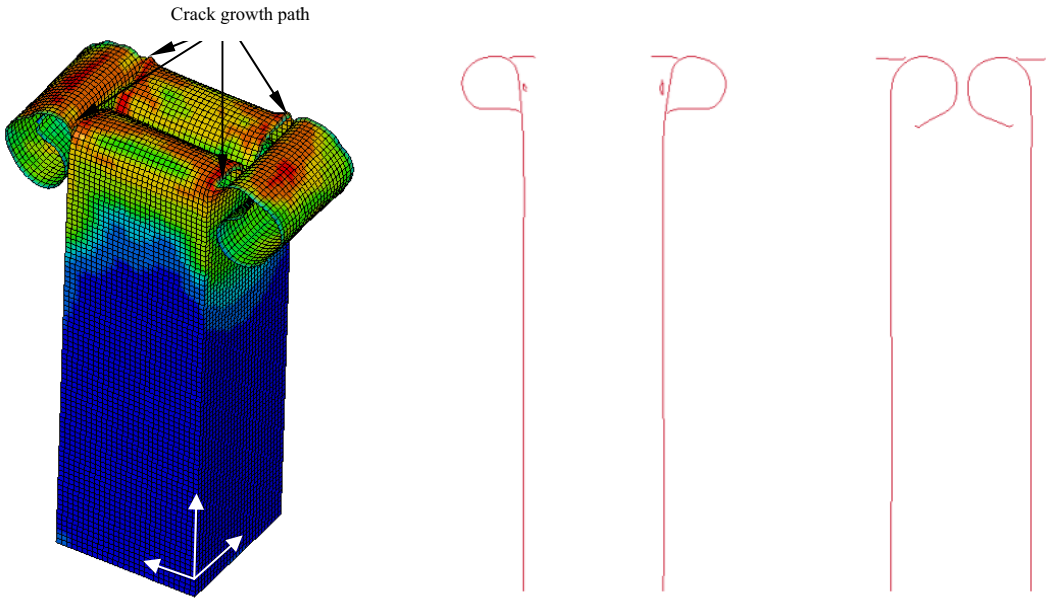

Figure 2.13

Splitting of the tube walls due to the removal of elements

2.4.6 Effect of self contact

The cut view in figure 2.14 illustrates an asymmetric crush process of a square tube. The folds start to appear in succession as the applied displacement is continued. Each fold maintains its configuration as the next fold starts to develop. The load reaches its maximum value at the beginning of the formation of horizontal hinge lines. As will be explained later, double bending controls the force while folds continue to accumulate with the surface of adjacent folds contacting each other as shown in figure 2.14F. This phenomenon has been captured in FEA by defining the self contact in such a way that no nodes of the tube can penetrate to the elements. The presence of self contact preserves

each crushed fold such that the force required to increase deformation is greater than that for forming a new fold. At this point, the folded region behaves as a bulk rigid structure such that any further deformation will be impossible provided that there is enough room for new folds to develop. When there is no capacity for folding formation, the crush force rapidly increases. This phenomenon is defined as locking. The accumulated crush distance this point represents, the effective crush distance (see figure 1.1), which plays an important role in mean crush force calculation. The internal dissipated energy is calculated from crush force versus crush distance curve up to this point, and the crush force is found by dividing this calculated energy by the effective crush distance.

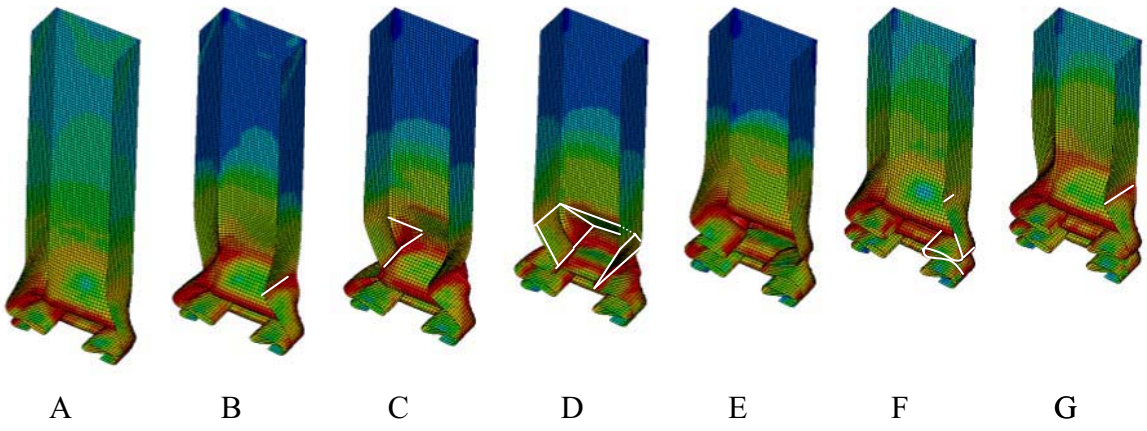

Figure 2.14

Folding progression in single-cell tubes under quasi-static axial compression

Another important factor in this self-contact process is the amount of friction that is present between two contacting folds with the coefficient of friction of 0.3. As depicted

in figure 2.15, friction decreases the overall crush force as well as the mean crush force of the tube very slightly. This means that any surface imperfection such as surface corrosion can affect the mean crush force and reduce the energy absorption capacity. Although based on the simulation results these effects do not change the energy absorption capacity tremendously, they should be considered in design. To identify the importance of self-contact, a crush tube model without self contact was analyised, with the result of crush force versus crush distance depicted in figure 2.15. For the sake of comparison, the effect of friction corresponding to two different friction coefficients is captured in figure 2.15. Looking at the result of the model without any self-contact, we note a fairly uniform crush pattern. The absence of self contact makes the crush process sequential such that the deformation in the tube will not be observed until the fold reaches the rigid wall. This can explain the steep increasing of load after each drop. As deformation reaches the end of the tube, there is no locking observed in this curve, which is analogous to assuming that the folds do not have any curvature and it is a complete fold. As mentioned above, the friction should be reduced in the surface, which can reduce the energy capacity of the tube.

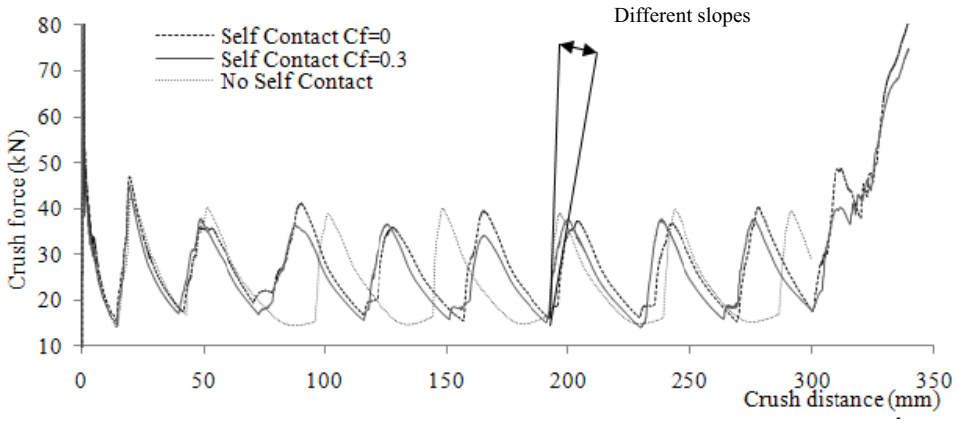

Figure 2.15

Effect of contact and surface friction on energy absorption

2.4.7 Thickness study

Figure 2.16 shows the crush force versus crush distance for two different wall thickness values. In single-cell tubes, increasing the wall thickness leads to larger amplitudes in load oscillation while increasing the mean crush force.

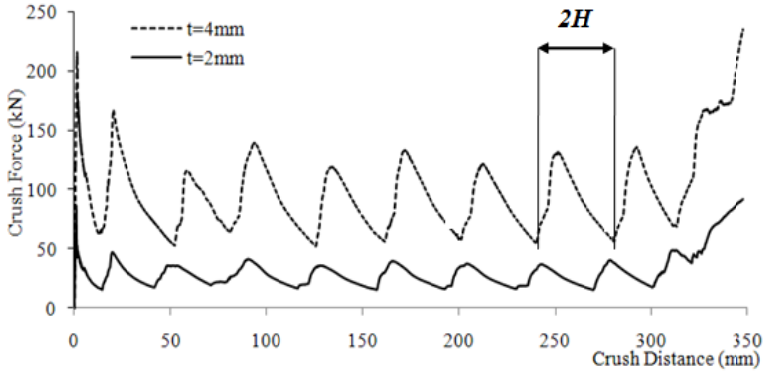

Figure 2.16

Effect of thickness on the crush behavior

The increase in crush force can be attributed to the increase in the second moment of area of the cross-section, and since the thickness is increased from 2 mm to 4mm, the load is 4 times higher due to this relation

$$\frac{\Delta P_{t1}}{\Delta P_{t1}} = \frac{I_{t1}}{I_{t2}} = \frac{t_1^2}{t_2^2} \tag{2.18}$$

Figure 2.17 illustrates the crush mode of the square tube with two different thicknesses. It turns out that the crush effective fold distance between two ends of the fold, x_{eff} shown in figure 2.17 can be identified in load-displacement curve (Figure 2.16). The actual fold size is *2*b. A relation between H and b can be derived. The effective folding height x_{eff} is also shown in figure 2.17. The effective crush distance is calculated using this relation

$$\delta_{\text{eff}} = (2\text{b} - \text{x}_{\text{eff}})\text{N}_{\text{fold}} \tag{2.19}$$

where $\text{N}_{\text{fold}}$is the number of folds. If there is no contact, x_{eff}=0 and the effective crush distance becomes $2\text{b}\ \text{N}_{\text{fold}}$.

The radius of curvature of the inward lobe is approximately two times greater than the outward lobe in the single-cell tubes. This relation can be justified by investigating the crush mode in figure 2.17. This figure also shows that by increasing the tube thickness, the folding pattern becomes more stable and periodically repeats throughout the crush process. For the tube with thickness value t=4mm, the primary bending radius is of the order of the shell thickness where as in the thinner tube this relation does not hold. It is worth mentioning that the ratio of outward lobe radius to the inward lobe radius stays constant as the thickness increases.

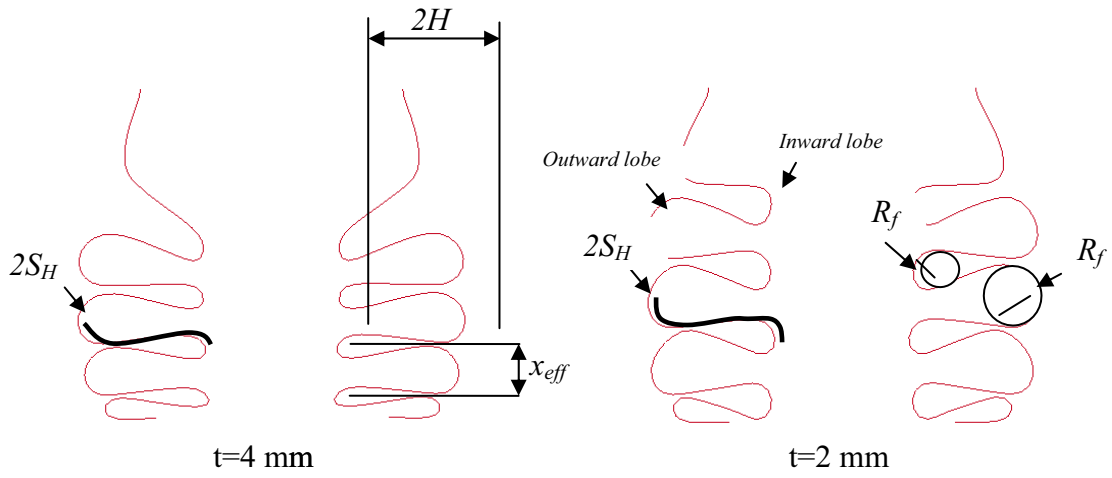

Figure 2.17

Crush mode cut view showing the folding pattern in the wall.

The scale of deformation in figure 2.18 is increased by 80% to reveal the double bending configuration. A paper model of the double-bending process is also shown in figure 2.18 for comparison. The same folding patterns can be seen in both the crush of thin walled tube and the double-folded paper. The bending will be formed in the primary bending regions by inward lobes and the inclined hinge lines. This is then followed by the second bending process. The primary bending area that participates in the secondary bending process is the inclined hinge lines as shown in figure 2.18.

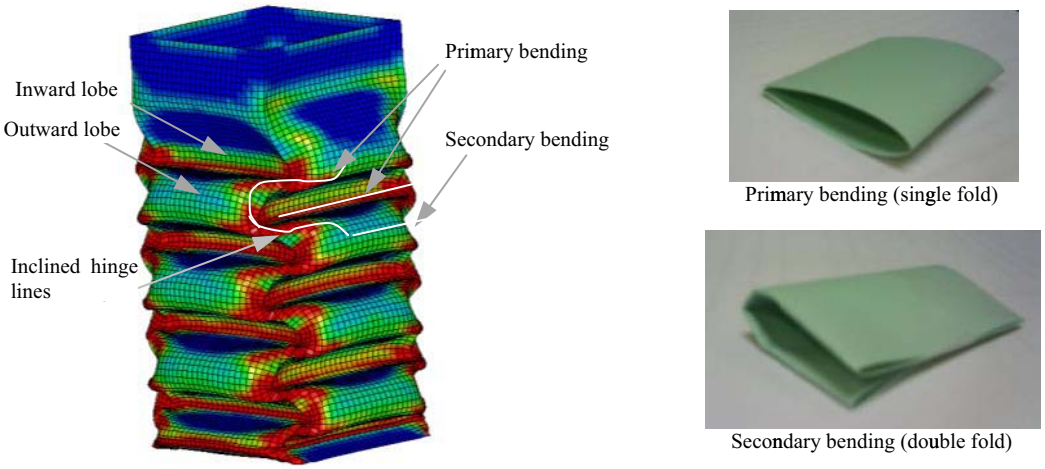

Figure 2.18

Formation of primary and secondary bending folds

The collapsing thin-walled tube undergoes very complicated strain-stress behavior. Material can go into tension, compression and shear during the crush process. The compression load starts to develop at the early stages of deformation up to a point that tube reaches its buckling load. The amounts of stress and strain due to pure axial compression depend on the configuration of imperfection or trigger mechanism and the effect of dynamic load in terms of stress wave propagation. These effects are negligible when a trigger mechanism is used in conjunction with quasi-static loading. In the horizontal hinge lines, the main mechanism of deformation is bending where the material experiences both tension and compression through the wall thickness. In this study, it is assumed that the tension and compression stress-strain behaviors of the material are identical and can be taken from the uniaxial tension test. Inclined hinge lines are also under bending while neglecting the effect of the corner, which is also bent and results in a much more complicated deformation pattern. Figure 2.14 shows the process of formation

of inclined hinge lines for a single cell tube with 4 mm thickness. As it is shown, the inclined hinge lines are not stationary in the crush process. The moving hinge line puts the material under bending, and while it proceeds further, material unbends to its flat state. This causes both loading and unloading of the material indicating that the tension, compression, shear and unloading properties of the material can have a strong effect on the energy absorption of the structure.

2.4.8 Stress-Strain response of elements in localized plastic region

Figure 2.19 shows the stress-strain response of a representative element in a horizontal hinge-line region. The normal stress in YY direction is plotted versus normal strain in element coordinate system. Both stress and strain are calculated in the upper surface of the shell element containing three integration points through the shell thickness. As expected, the largest stress occurs in YY direction that is perpendicular to the horizontal bending axis. Since the values are calculated in the upper surface, the stress is mainly tensile. Similar compressive behavior can be captured by calculating the stress and strain on the lower surface.

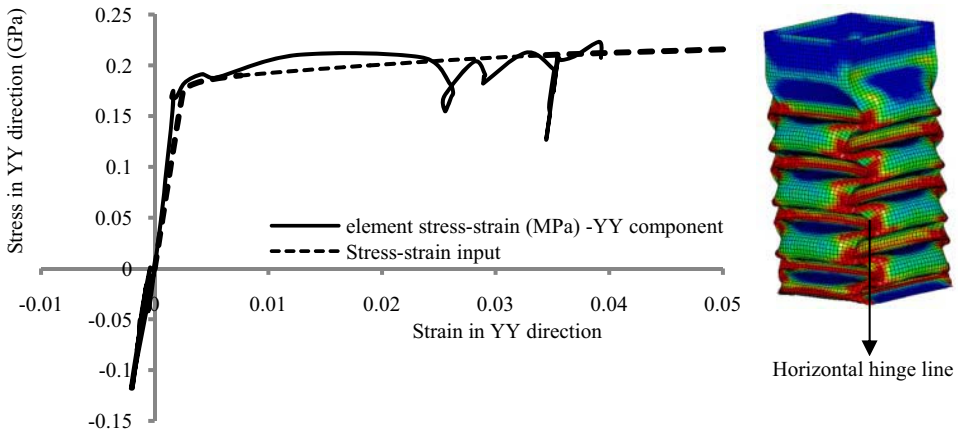

Figure 2.19

Stress-strain response of an element of the horizontal hinge line

Figure 2.20 shows the stress on the lower surface of the toroidal surface. The stress in this region is compressive.

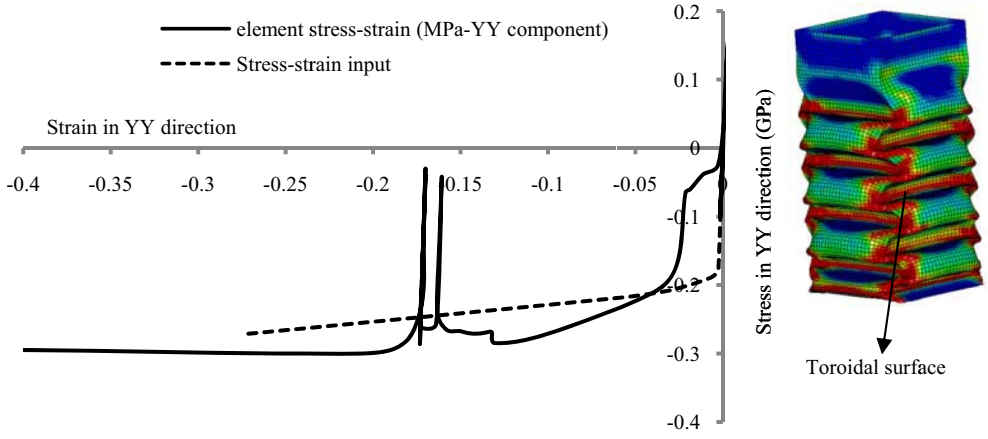

Figure 2.20

Stress-strain response of an element of the toroidal surface

Figure 2.21 shows the stress and strain response of an element which is located in the "moving" inclined hinge line. As discussed earlier in this chapter, the material experiences both loading and unloading in different regions. Because of this property, the material with the Baushinger (Wierzbicki 1999) effect should be modeled using a model that has kinematic hardening or anisotropic texture behavior.

The stress-strain response affected by the material behavior has a huge effect on the energy absorption prediction of the tube. One of the major issues in this respect is the effect of anisotropic texture which shows that the behavior of an isotropic material can be anisotropic and vary in different directions. This property can be expected from thin-walled structures manufactured by any kind of forming or extrusion process. Having this property and also damage properties in the model can improve and extend the computational capability to explore the energy absorbing capacity of different tube designs. It is worth mentioning that capturing all of these features in large-scale problems is very expensive as it would require the use of a large number of elements.

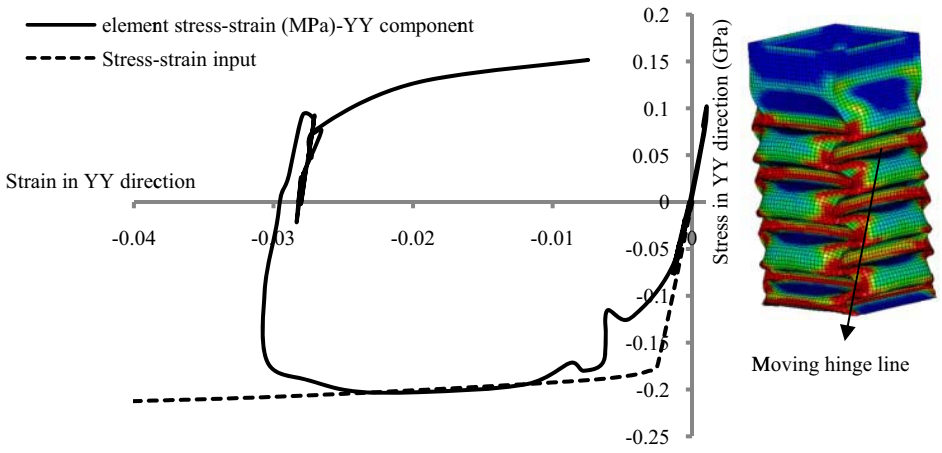

Figure 2.21

Stress-strain response of an element of the moving hinge line

2.5 Dynamic simulation of square tubes

In the previous section, the crush behavior of thin-walled square tubes under quasi-static loading was discussed. The quasi-static analysis enabled us to capture the relationship between energy absorption and the mean crush force without considering any dynamic effects. However, in many cases, energy absorbing components are designed for structures that are exposed to impact loads. The main feature of impact is that the loading occurs within a short time duration. Because of time dependency of the process, the deformation process is not static but dynamic. Experimental studies have shown major differences in the energy absorption characteristics of energy absorbing components (Calladine 1984). Some of these differences are due to loading, boundary conditions, folding mode shape, and material properties (Karagiozova 2008). There are two major factors in dynamic collapse that do not appear in the quasi-static collapse. The first is the rate sensitivity property of material such that the yield point and flow stress of material

depend on the value of strain rate. For instance, in mild steel, representing a rate-sensitive material, the value of yield stress in dynamic case is almost 2 times higher than the quasi-static case. The second factor is due to the inertia developed in the structure due to the rapid acceleration. This can be explained in terms of the effect of stress wave propagation as well. In this section, the strain rate effect is captured through Cowper-Symond phenomenological model. Two cases of dynamic loading are considered, one is a constant velocity loading and the other is an impact loading with an initial velocity.

2.5.1 Model description

The two dynamic loading cases considered are shown in figure 2.22, and identified as Case I and Case II. In Case I, dynamic loading simulation, a tube is held fixed at its base while it is struck at the other end by a 300-kg rigid block (hammer) traveling at an initial speed of V_0 m/s as shown in figure 2.22. In Case II, the constant velocity is applied as a fast enforced displacement similar to the quasi-static analysis but using a higher velocity (figure 2.22).

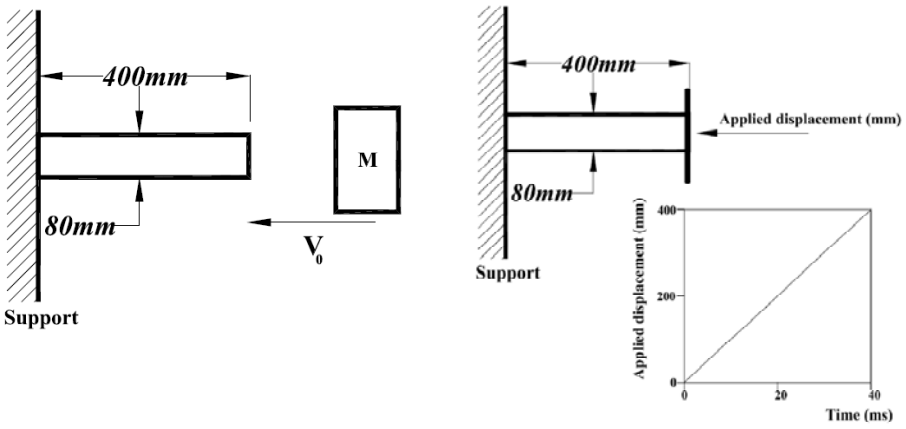

Case I Case II

Figure 2.22

Description of the dynamic loading cases

The contact friction coefficient between the rigid wall and tube is set at 0.3. To prevent element-element penetration due to excessive deformation, a frictionless self-contact condition has been specified for the element surfaces. The material used in this simulation is aluminum alloy AA6060-T6 (E = 70 GPa, ν = 0.3, and ρ = 2.7e-6 kg/mm^3) with tensile true stress-true strain curve shown in figure. 2.3.

2.5.2 Effect of shell element formulation

An element study, similar to that in quasi-static case, is performed using the dynamic loading condition and without introducing any trigger mechanism (Najafi 2008). The collapse responses are shown in figure 2.23 with the top end representing the impact side of the tube. Figure 2.23 shows that the predicted collapse mode shapes are different. Based on quasi-static and dynamic simulations, the element formulation EF1 (Hughes-Lu shell element) has been chosen for the simulations in this study.

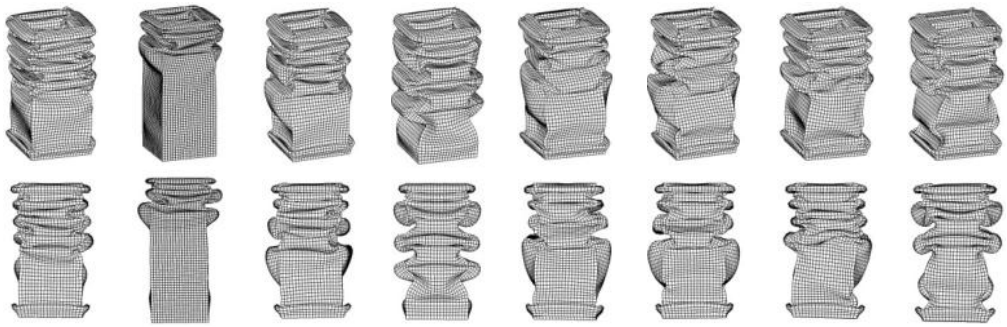

Figure 2.23

Crush responses under dynamic load for different shell element formulations in LS-DYNA (Najafi 2008)

2.5.3 Effect of initial velocity

One important feature of the tubes without a trigger mechanism under dynamic load is the effect of velocity on the symmetric folding formation at the bottom (supported) end of tubes, which is called bottom-out deformation (Jones 1998) (Karagiozova 2004). This effect is investigated in figures 2.24 and 2.25 for the tubes with no rate sensitivity and wall thickness t=2 mm. Although the main deformation pattern is easier to develop at the contact point, the elastic/plastic wave propagation causes the tube to bottom out. This forces the structure to experience an instability, which may result into global bending of the tube, not desirable for axial crush. The amplitude of this deformation varies with the impact velocity. Figure 2.24 also shows that the deformation near the fixed end is changing with velocity. The deformation reaches the maximum at $V_0=15$ *m/s* while disappears for the initial velocity of $V_0=40$ *m/s*.

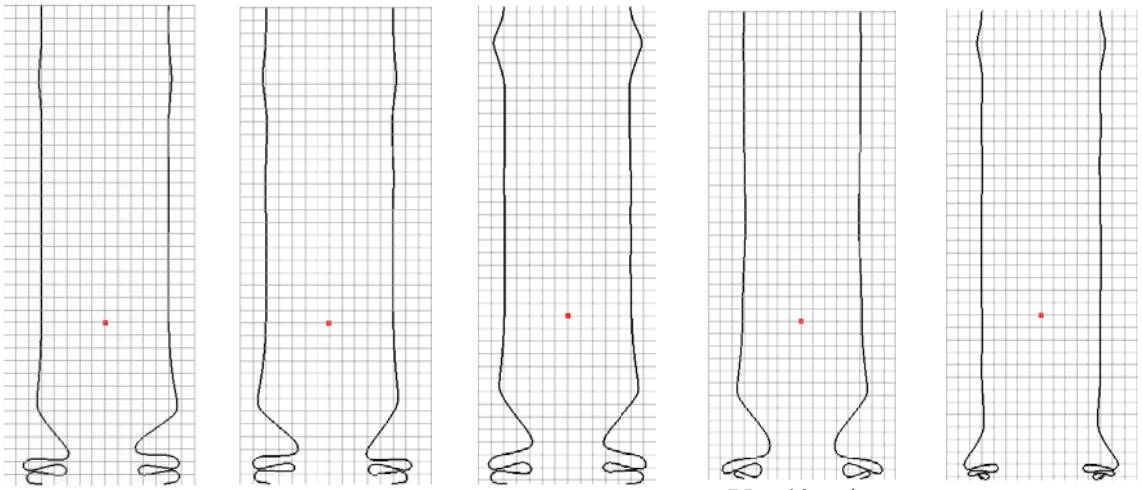

V_0=5 m/s V_0=10 m/s V_0=15 m/s V_0=40 m/s V_0=100 m/s

Figure 2.24

Effect of initial velocity (case I) on the crush mode of a square tube without trigger mechanism

The crush behavior in terms of crush force versus crush distance is presented in figure 2.25. The bottom plot shows the initial crush behavior of the tube. The maximum initial peak increases as the initial velocity goes higher. For the velocity range of 5 to 15 m/s, there is no considerable difference between their observed initial peaks. In this range, the overall behavior stays approximately the same for the whole crush process. As shown here, the initial velocity changes the deformation pattern in tubes without trigger mechanism.

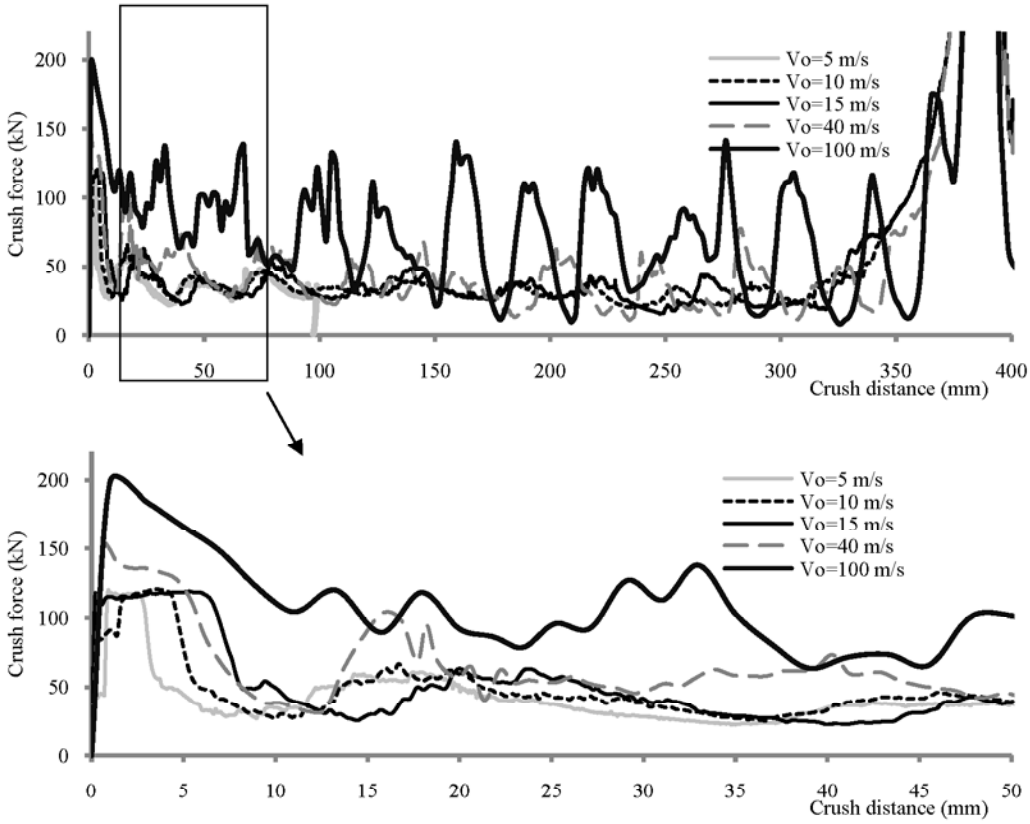

Figure 2.25

Effect of initial velocity on the crush behavior of a square single-cell tube without trigger mechanism

2.5.4 Effect of thickness

As shown in figure 2.26, the crush mode in tubes without trigger is symmetric whereas in tubes with trigger it is asymmetric. Symmetric crush mode has higher mean crush force because of having higher energy dissipation through plastic deformation (Abramowicz 1984), (Langseth 1996). The crush mode in t=2mm evolves from symmetric mode to asymmetric mode shape due to the fact that the energy in asymmetric mode is lower than the symmetric mode. By increasing the wall thickness, this instability

can be eliminated as shown in figure 2.26. For thickness t=4mm, the whole deformation process appears as a pure symmetric mode shape. The main consequence of increasing the wall thickness is the weight penalty. Using sandwich walls can improve the energy absorption and keep the weight as low as possible. The quasi-static response of tubes with sandwich walls was also considered by (Mohr 2003, 2004, Santosa 1999) through experimental and numerical investigations. They observed the symmetric and mixed deformation modes in their studies.

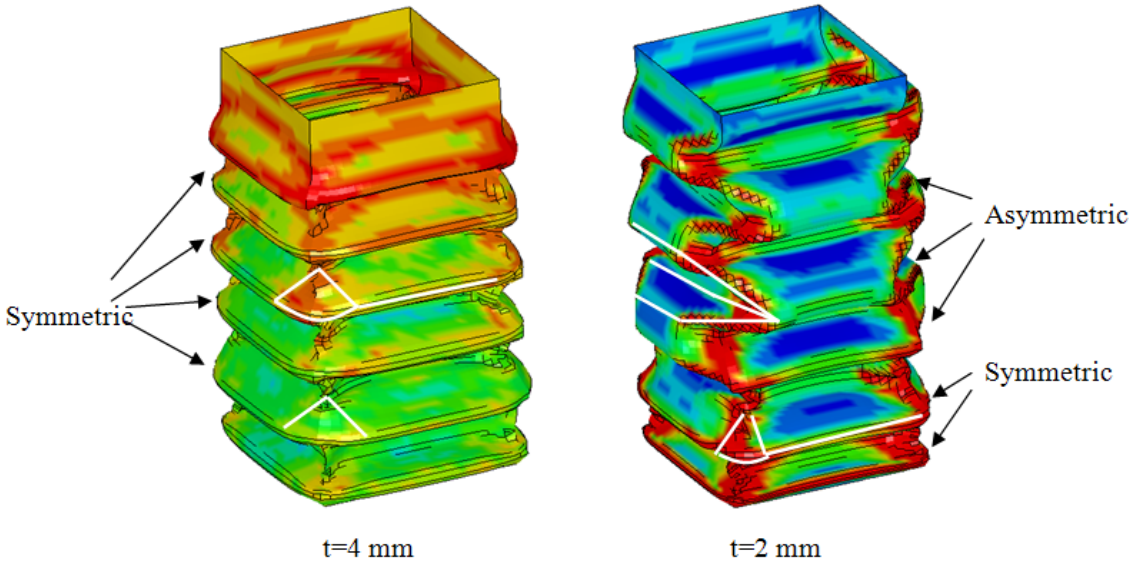

Figure 2.26

Effect of thickness on the folding pattern of a square single-cell tube without trigger mechanism

2.5.5 Effect of trigger mechanism

The effect of trigger mechanism on the crush mode under dynamic loading Case I is shown in figure 2.27. The deformed shape is magnified by the factor of 0.8 to reveal the folding pattern more clearly. Figure 2.27 (a) depicts a tube without trigger where the out-of-plane deformation pattern started from both ends of the tube with symmetric

deformation mode shape. The response of tubes with trigger located at 5mm, 15mm, and 30mm are shown in figure 2.27(b),(c), and (d), respectively. As shown in figure 2.28, the trigger mechanism affects the initial crush force very dominantly. Crush force in the tube with trigger stays higher than the cases without trigger mechanism due to the difference between initial folding patterns up to a point which the crush mode changes from symmetric to asymmetric mode. Tubes without trigger need much higher load to deform the sidewalls in order to initiate the folding process. Although the crush load is higher in this case, it is very sensitive to any possible flaw or imperfection in the tube. The effect of trigger distance on the crush behavior is also shown in figure 2.28. As pointed out in quasi-static analysis, the major contribution of trigger mechanism is to stabilize the folding pattern. Due to the axial load, the tube is very susceptible to any non-symmetric perturbation, which may result global bending as opposed to axial collapse. Axial collapse can be achieved by trigger mechanism due to the indentation load offsets that causes a bending moment in the structure. The location of this indentation (trigger distance) forms the first folding pattern because of increasing the imposed bending moment.

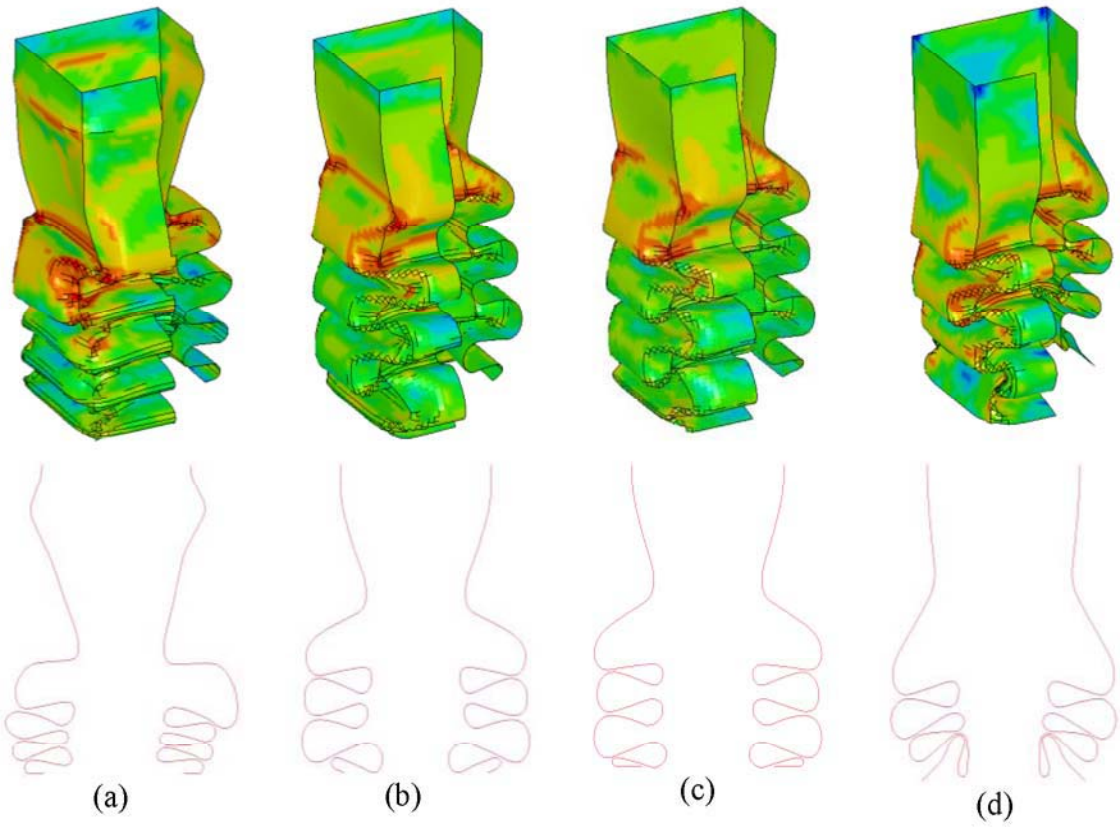

Figure 2.27

Effect of trigger mechanism in the crush mode deformation (a) no trigger, (b) d=5, (c), d=15, and (d) d=30 mm

Once a trigger distance is larger than the folding height, x_{eff}, the second peak of the crush load decreases due to the increase in the moment arm as seen in d=30mm, whereas by moving the trigger closer to the impacted end, the amount of second peak load increases. With d=15mm, the second peak is in the order of the other peaks. This location will be used for all the subsequent simulations. The proposed trigger mechanism does not affect the mean crush force considerably. However, it changes the crush force at the initial folds that can reduce the initial impact load resistance.

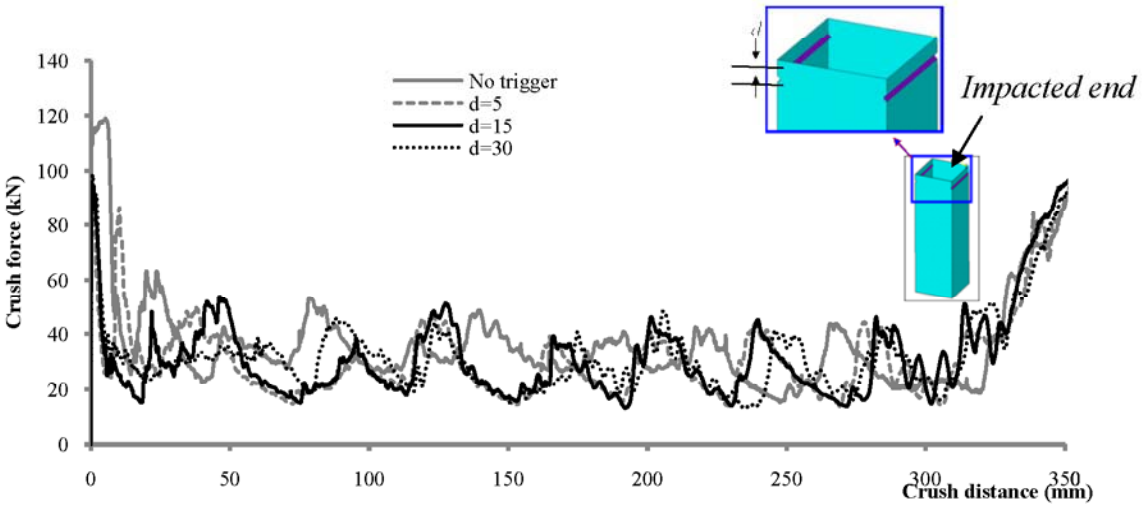

Figure 2.28

Effect of trigger mechanism on the crush behavior

2.5.6 Effect of velocity in tubes with trigger mechanism

The magnitude of initial velocity also affects the tubes with trigger mechanism. The effect of velocity on the folding pattern in both dynamic load cases is presented in figure 2.29. The crush deformations for three initial velocities are compared with the quasi-static analysis by neglecting the rate sensitivity parameters. The crush modes at higher velocities have a more compressed shape than the quasi-static results such that the radii of the internal and external lobes become closer; in the quasi-static case, they are different by the factor of 2. As a result of this dynamic effect, the plastic strain increases with initial velocity whereas the folding height decreases.

The effect of initial velocity on the crush behavior under the dynamic load Case I is compared with the quasi-static case in figure 2.30. The crush force changes by increasing

the initial velocity. The reason for this change is that the strain response in the folded lobes is greater for higher initial velocity values.

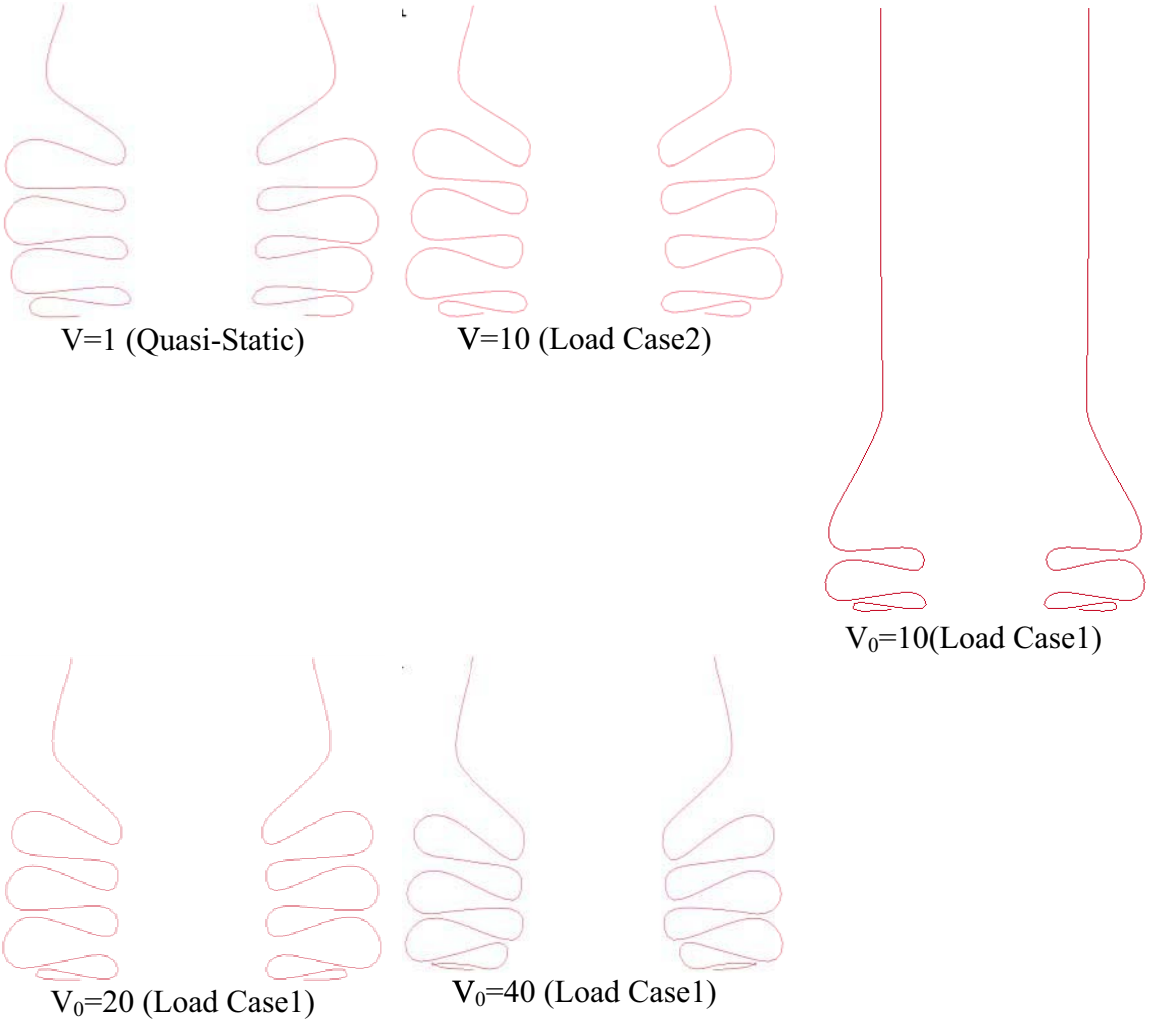

Figure 2.29

Effect of impact velocity on the deformation shape of tubes with trigger mechanism

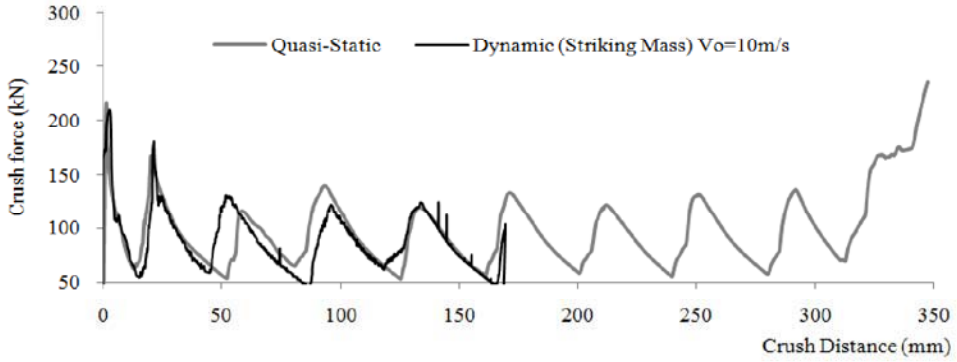

(a)

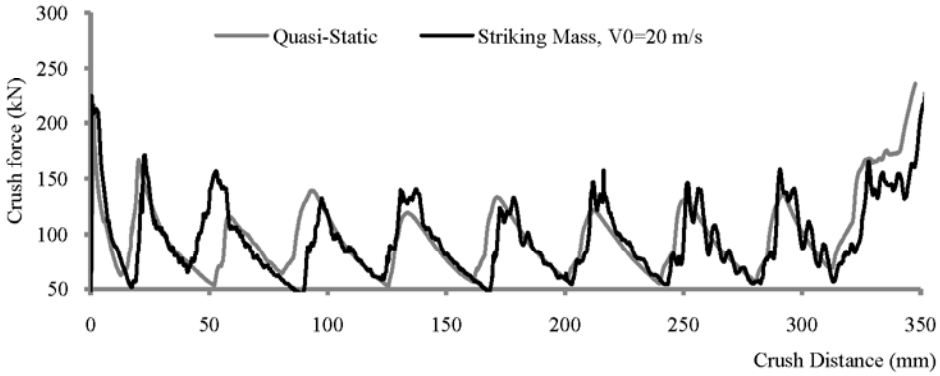

(b)

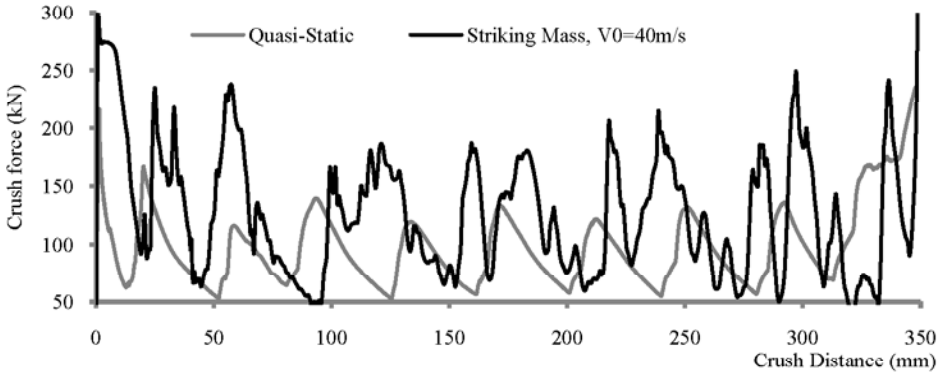

(c)

Figure 2.30

Crush behavior of tube under dynamic load Case I with initial velocities at (a) 10m/s, (b) 20m/s, and (c) 40m/s

2.5.7 Effect of striking mass

Two different values for impactor mass are considered to study the effect of striking mass on the energy absorption characteristics of the tube with trigger distance of 15mm. Figure 2.31 shows the crush behavior plot for two different mass values. It was shown that the energy absorption behavior of crush tubes is not influenced by the mass of striker. This finding is consistent with the results found by Krogiozova (Karagiozova 2004a).

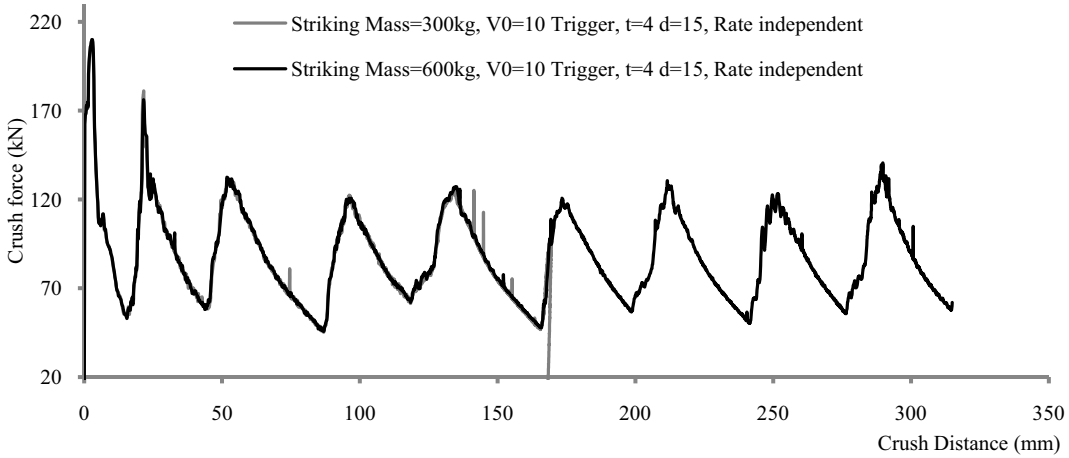

Figure 2.31

Crush behavior of tube for striking mass of M=300kg and 600 kg

2.5.8 Effect of rate sensitivity

Rate sensitivity effect is represented by Cowper-Symonds phenomenological relation in L-DYNA. This model has two parameters in equation 2.11. These constants are calculated for aluminum and magnesium alloys (D=1288000 s^{-1},p=4) (de Kanter 2006) and (D=570 s^{-1}, p=3), respectively. The dynamic response of tubes with different strain

rate sensitivity parameters is illustrated in figure 2.32. It was seen that the strain rate sensitivity can have a considerable impact on the crush behavior.

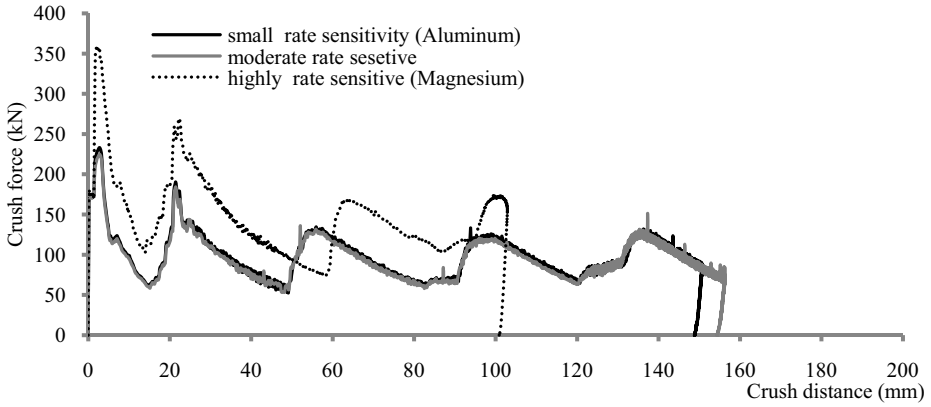

Figure 2.32

Influence of rate sensitivity on the crush behavior

2.6 Summary

The explicit nonlinear finite element analysis is found to be suitable solution of non-smooth problems involving highly nonlinear characteristics. The main drawback of this solver is that it is conditionally stable and the stability of the solution depends upon the time step size. The different shell element formulations available in LS-DYNA were considered and their performance in crush analysis of thin-walled tubes was investigated. It was found that Hughes-Liu (EF1) and Belytschko-Tsay (EF2) are appropriate shell elements for crush simulation. The number of integration points through shell thickness is also investigated, and it was shown to affect the crush behavior of tubes due to large amount of bending present in localized plastic regions. Quasi-static simulation was performed using slow enforced displacement with constant rate (constant velocity). The

computational model tube was evaluated by studying the effect of trigger mechanism, tangent modulus, material toughness, strain-to-failure and thickness. Trigger mechanism stabilizes the crush mode in quasi-static cases. The trigger mechanism used in this study imposes the asymmetric crush mode on the structure, which is a stable crush mode because it has the lowest energy that a thin-walled tube can dissipate under axial crush force. The trigger distance did not affect the overall mean crush force of the tube while it affected the second peak crush force due to the difference in moment arm that is directly resulted from the trigger distance. Tangent modulus also affects the mean crush force. It was shown that toughness affects the mean crush force considerably provided that the toughness is increased in terms of yield stress and tangent modulus as opposed to the total area under the stress-strain curve. Failure strain is a crucial parameter, where it can change the crush mode to a splitting mode. It was shown that the self contact definition provides a proper definition of actual problem. Although friction did not change the crush behavior considerably, it was shown that a high surface roughness is not desirable for crush. It was illustrated that the fold formation is a result of double bending formation and the effective crush distance is defined based on double-bending of the walls. Looking at the stress-strain response within different elements in the model revealed that the material will undergo complicated stress-strain changes including unloading. This reveals the importance of Baushinger effect and the kinematic hardening and anisotropic yield surface parameters. Dynamic load simulations were performed based on two loading strategies: load Case I by applying initial velocity and load Case II by applying a constant velocity throughout the crush process. Dynamic load can be distinguished from quasi-static through two major factors including elastic-plastic wave propagation or inertia

property and material strain rate sensitivity. In the tubes without trigger mechanism, the stress wave propagation under dynamic load can result in formation of a partial fold at the bottom end of the tube whereas in the cases with trigger mechanism this effect vanishes due to the confined deformation in the triggered area. Strain rate effect appeared in models with and without trigger. Striking mass does not seem to have any effect on the crush behavior of tubes.

CHAPTER III

QUASI-STATIC AND DYNAMIC SIMULATION OF MULTI-CELL MULTI-CORNER TUBES

3.1 Model Description

Previous studies on crush characteristics of various multi-cell tubes have shown that such tubes can have fairly high capacity for energy absorption (Chen 2001, Zhang 2006, Kim 2002). In this chapter, the result of an investigation on the effect of cross-sectional configuration on energy absorption of multi-cell, multi-corner tubes are presented. This investigation was focused mainly on the evaluation of multi-cell tubes possessing acute and obtuse corner geometries with models in figure 3.1 as four possible examples. The selected models generally show a square inner tube connected to a square outer tube twice its size. The distinguishing feature is the way the inner and outer tubes are connected together to form the multi-cell geometry. The connecting webs create *corner-to-corner (C2C)*, *corner-to-web (C2W)*, *web-to-corner (W2C)*, and *web-to-web (W2W)* attachments in these models. Although the shape and wall thickness of the inner and outer tubes are identical in all four models, there is a slight weight difference due to minor variation in width dimensions of the connecting webs. Since energy absorption and the stability of progressive folding are heavily dependent on the corner elements (Kim

2002), the four configurations can produce different crush characteristics. The wall thickness is kept constant at 2mm with the outer and inner tubes having a side dimension of 80mm and 40mm, respectively. The length of the tube is 400mm. All FE models are based on Hughes-Liu (EF1) shell elements (Halquist 1998).

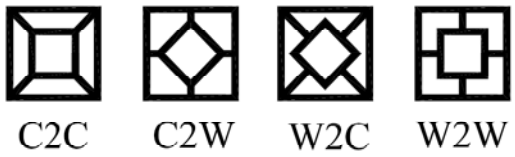

Figure 3.1

Cross-section of multi-cell multi-corner tubes

3.2 Quasi-static response of multi-cell tubes

The quasi-static loading condition and associated parameters are the same as those discussed in the previous chapter. Three integration points are used through the shell thickness. An indentation trigger mechanism similar to that figure 2.7 is used on two opposite walls of the outer tube. There is no trigger mechanism in the inner tube.

3.2.1 Crush mode

A cut view of the folded tubes is shown in figure 3.2. The crush mode shapes reveal a more complex folding pattern than that observed previously in single-cell tubes. The outside and inside lobes are no longer symmetric (figure 3.2, 3.3). This can be attributed to the presence of internal folds such that in one side of the deformed shape a simple curvature occurs due to bending, whereas in the outer fold double curvature is responsible for folding radius. The first fold radius is usually in the same order as the tube thickness.

As shown in figure 2.14, the terminal stage of deformation is a result of two subsequent bending of initially flat sheet metal. At the center of the tube, this deformation can easily be identified at the center of the tube sides. Radius of the cylindrical bending is governed by folding of side plates rather than by corner lines. This may not be the case for multi-cell tubes that have a wall with smaller value of C/t where C and t represent the flange size and wall thickness, respectively.

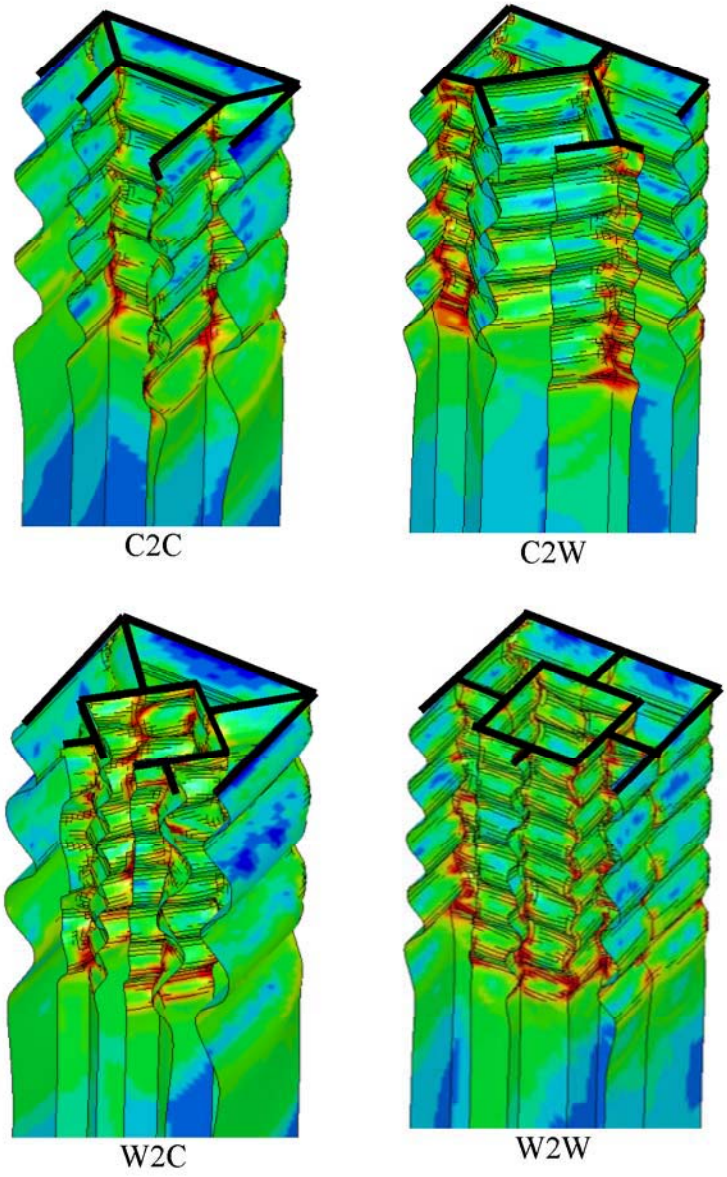

Figure 3.2

Crush mode in different multi-cell tubes

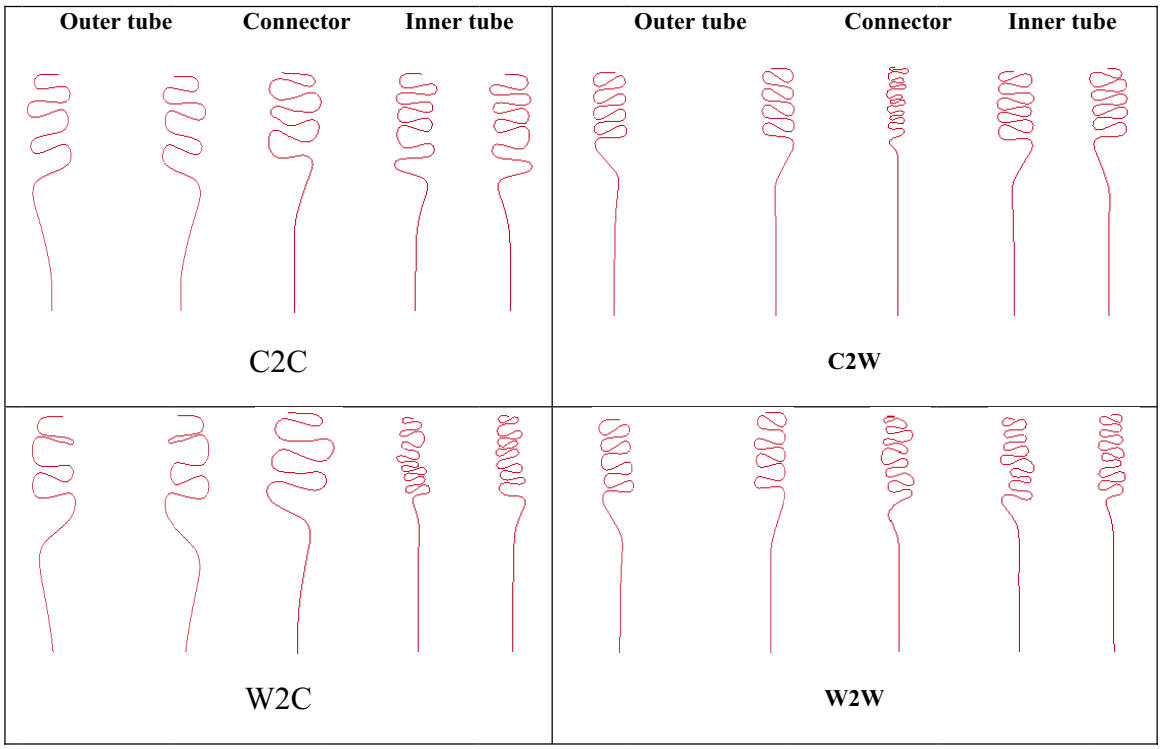

Figure 3.3

Cut view of the crush mode in multi-cell tubes

Table 3.1 shows the folding geometry based on parameters defined earlier in figure 2.17. As mentioned above the number of folds and the equivalent projected fold length vary in each wall. As the flange size decreases, the number of folds increases. This data shows that the folding irregularity in this region becomes very dominant, and it is difficult to identify a uniform folding pattern in such multi-cell tubes.

Table 3.1

Geometry of the deformed shape in each wall of the investigated multi-cells

Configuration	element	# of external folds	Actual fold length $2S_H$ (mm)	Equivalent Projected fold length 2H (mm)	effective folding height x_{eff} (mm)
C2C	Outer tube	7	30.5	25.5	7.5
	Connector	7	27	21	10
	Inner tube	9	22	17	6.5
C2W	Outer tube	9	22	17	10
	Connector	17	10	6	3.5
	Inner tube	9	20	15	8
W2C	Outer tube	6	33	24	10
	Connector	6	33	24	8
	Inner tube	12	15	10	4.5
W2W	Outer tube	8	25	17	6
	Connector	~12	20	14	3
	Inner tube	~12	22	16	5

3.2.2 Energy absorption behavior

Figure 3.4 shows the crush behavior of the multi-cell tubes in figures 3.2. Each is compared with a square tube, having a 4-mm thickness, as a baseline model. The thickness of the single-cell tube is selected such that the mean crush force is close to that of the multi-cell tubes. The difference in the load fluctuation is the main noticeable difference between multi-cell tubes and the baseline model. The crush force fluctuation in the crush process for multi-cell tubes is smaller than the baseline as the slope of the load-displacement curve is sharper in the baseline model. The crush force fluctuations of the multi-cell tubes are less than single-cell tubes. The load-displacement behavior shows that the folding pattern is more complicated and the number of folds cannot easily be identified from load-displacement curve. This means that a larger area in the structure is participating in load resistance. Thus, the multi-cell tubes have more rigidity than single-

cell tubes. Another characteristic of the multi-cell tubes is that the effective crush distance is lower than the baseline (table 3.1). The decreasing crush distance is due to the fact that the self-contact in the tube is increased and the accumulated folds are more rigid than the baseline.

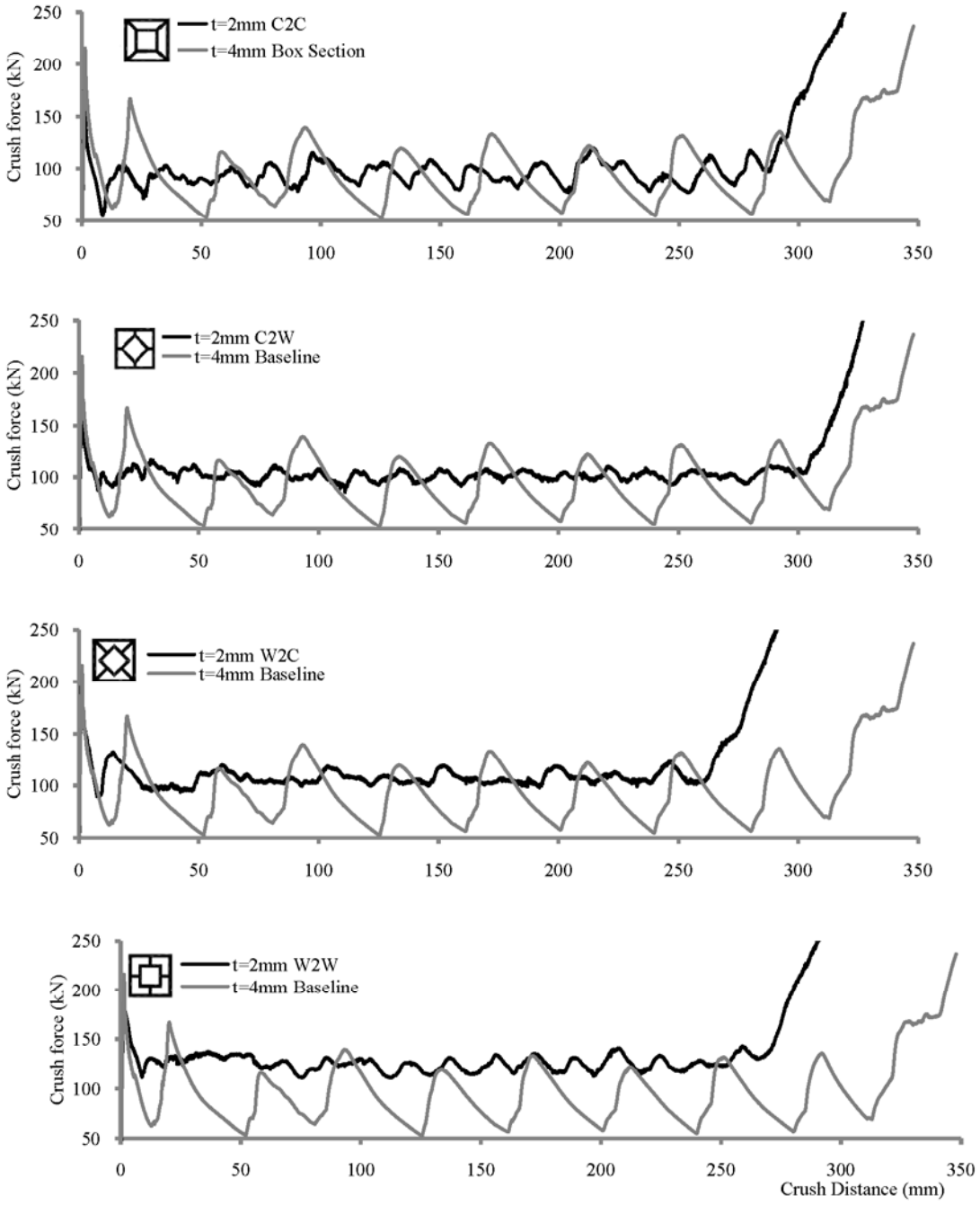

Figure 3.4

Crush behavior of multi-cell tubes and the baseline model

3.2.3 Effect of thickness

In this section, the effect of wall thickness in multi-cell tubes is examined (figure 3.5). The material used is similar to the previous analyses (AA6061-T6) with very low strain-rate sensitivity and three integration points through the shell thickness. As it was shown in the single-cell tubes, the load fluctuation increases with increasing the wall thickness. The effective crush distance remains constant in all cases.

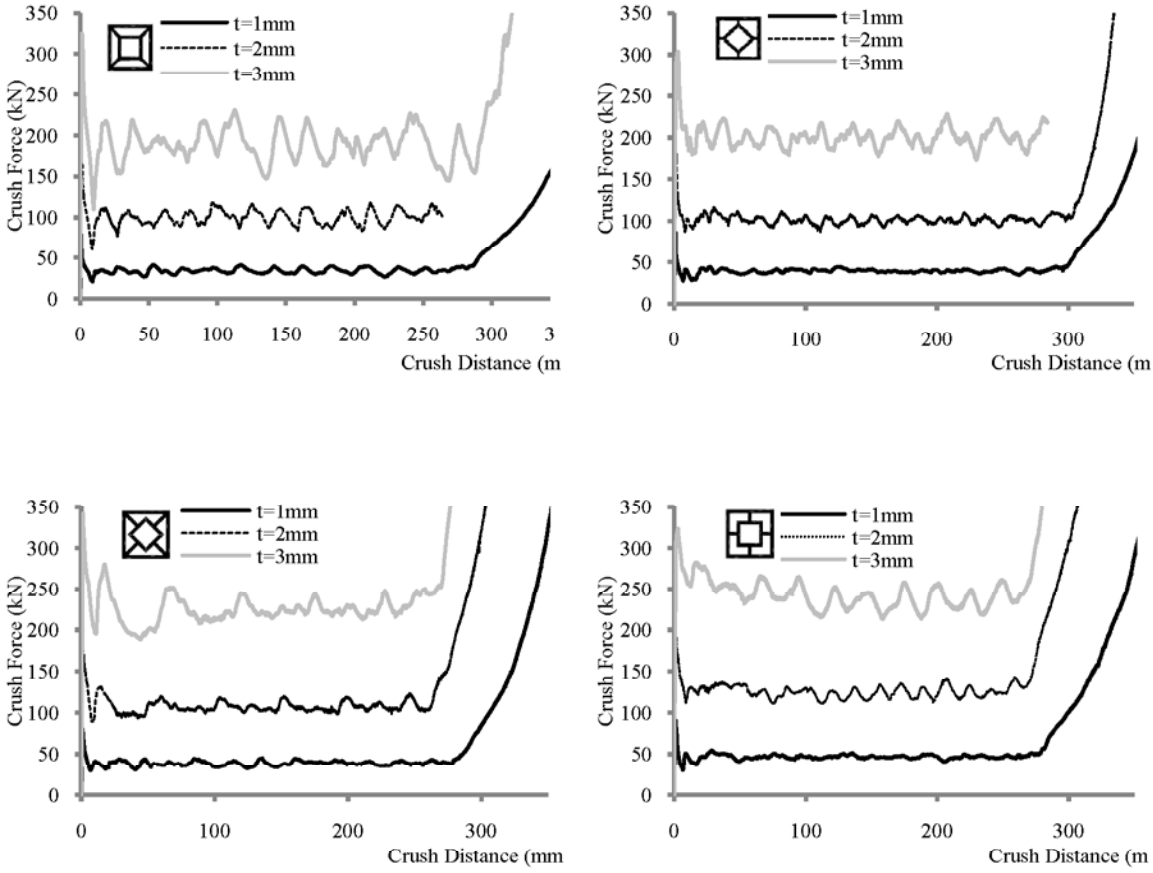

Figure 3.5

Effect of wall thickness on crush behavior of multi-cell tubes

3.3 Comparison with other cross-sectional shapes

The effect of cross-sectional geometry of the proposed multi-cell tubes and other multi-cells examined in the literature (Chen 2001, Zhang 2006) is captured in the plots shown in figure 3.6. The crush behavior pattern in the multi-cell to be with square cell geometry has a periodic crush pattern similar to single-cell tubes. For the multi-cell tubes with nonequal cells, the crush behavior is more complicated, which is directly because of the dissimilar folding pattern of nonequal flanges. The effective crush distance for the 2by2 and 3by3 configurations is higher than the proposed multi-cells.

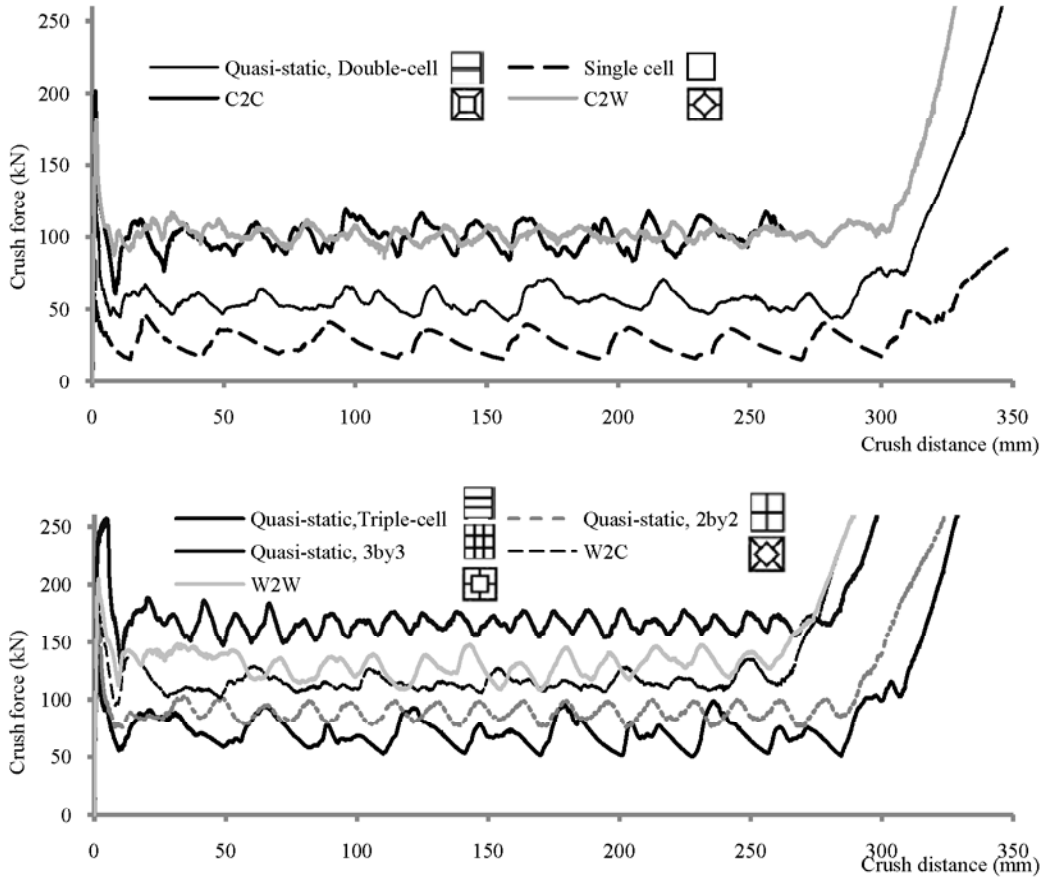

Figure 3.6

Crush behavior of multi-cell tubes proposed in other studies (Chen 2001, Zhang 2007)

3.4 Dynamic response of multi-corner multi-cell tubes

The effect of increase in constant velocity in dynamic loading Case II is shown in different multi-cell tubes in figure 3.7. Although this simulation may not be feasible experimentally, in many studies (Otubushin 1998, Zhang 2006, Meguid 2007, Faruque 2008) this simulation is considered as a quasi-static simulation. Neglecting any rate sensitivity effect, a slight increase in the crush force is observed in all cases except C2C that remains almost constant. This result shows that although the quasi-static simulation may take a longer time, the response may vary due to the dynamics of the problem.

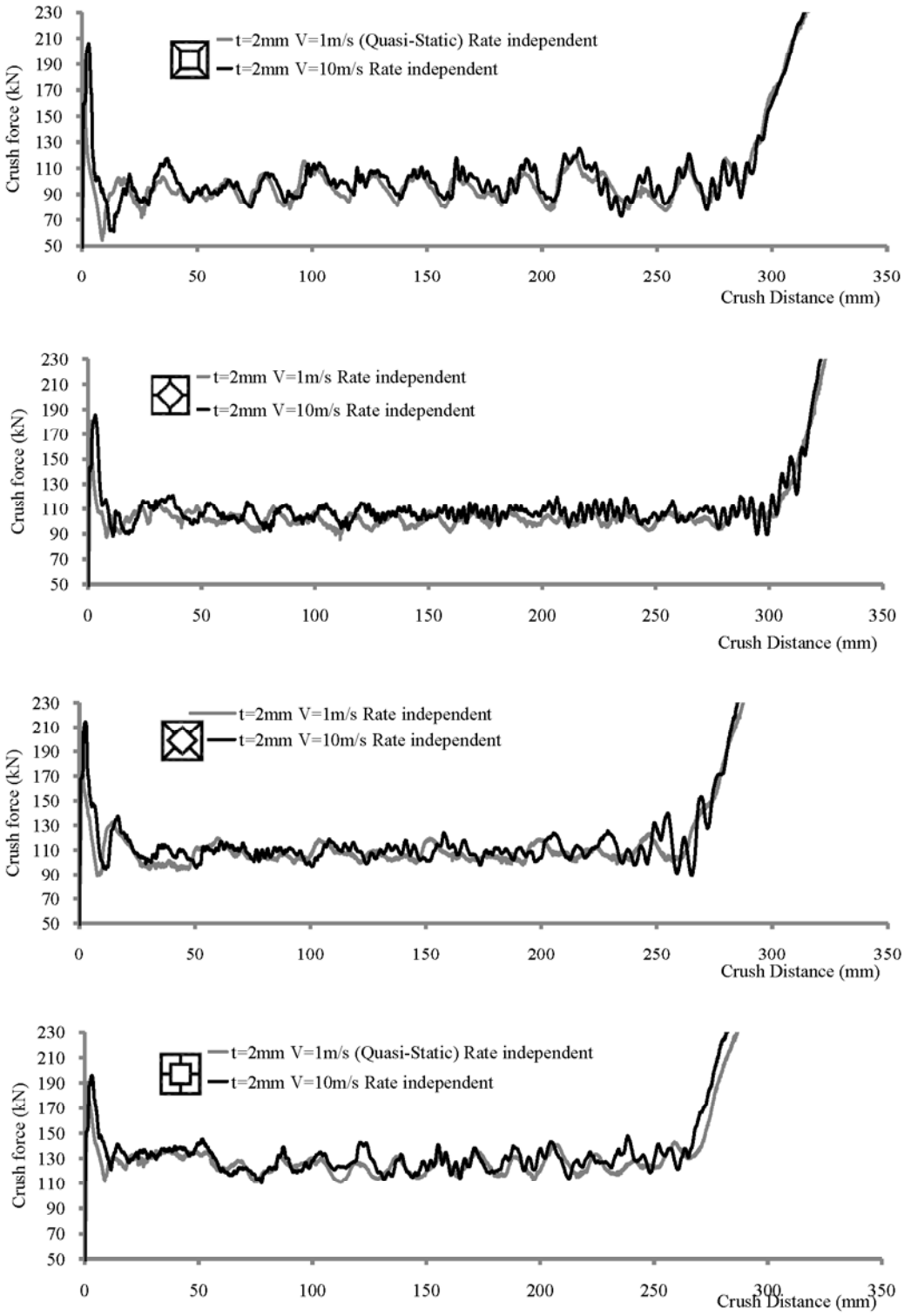

Figure 3.7

Dynamic crush simulation with constant velocity for multi-cell tubes

As a rough estimate of the limit on applied constant velocity, this velocity should be low enough such that the plastic wave is not created at the instance of initial load application. This limit can be calculated from the plastic wave propagation problem proposed by Von Karman (VonKarman 1950) with this relation

$$V_{limit} = \frac{\sigma_y}{\rho\, c_0} \tag{3.1}$$

where σ_y , ρ and c_0 are yield stress, material density and elastic wave speed, respectively. This value for aluminum with the yield stress $\sigma_y = 175\ \mathrm{MPa}$ is $V_{limit} \approx 12\ \mathrm{m/s}$. By adding very small rate sensitivity as seen in AA6061-T6, the rate effect emerges to be a very crucial factor in the energy absorption behavior in dynamic loading.

The effect of rate sensitivity on the crush behavior of multi-cell tubes in load Case II is plotted in figure 3.9. It is seen that the very low rate sensitivity present in AA6060-T6 can affect the results. This change can be significant in rate sensitive materials such as magnesium alloys.

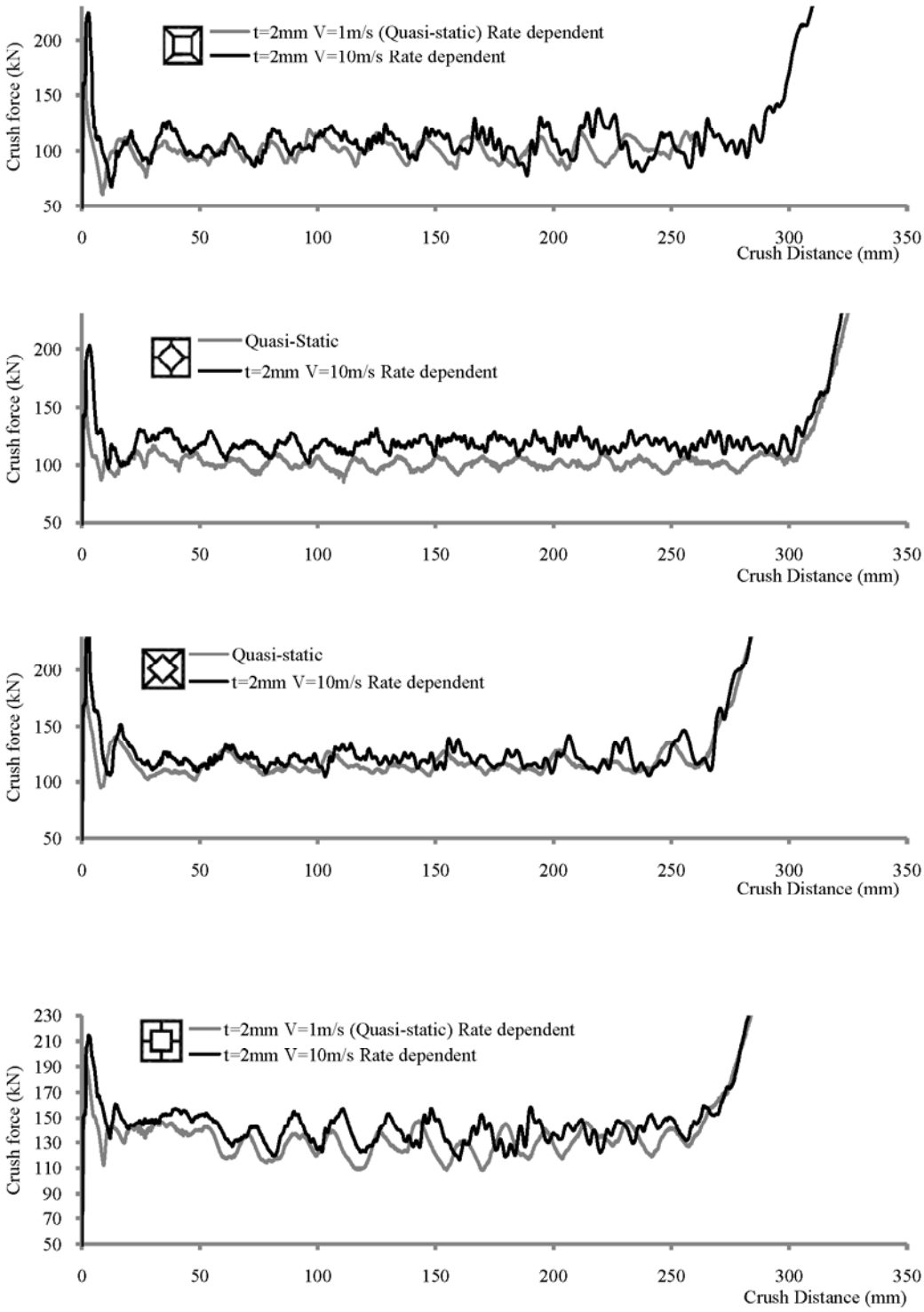

Figure 3.8

Effect of rate dependency in load case II for multi-cell tubes

In the impact dynamic load case, two initial velocities are considered and compared with the quasi-static results. Despite the very small rate sensitivity of aluminum alloy, the crush force increases with velocity. Since the potential plastic dissipation energy of tube is higher than the kinetic energy of initial velocity of 10m/s, the dynamic effects of crush disappears as the velocity of impactor approaches zero, whereas in the initial velocity of 15m/s tubes crush throughout the entire length (Figure 3.8).

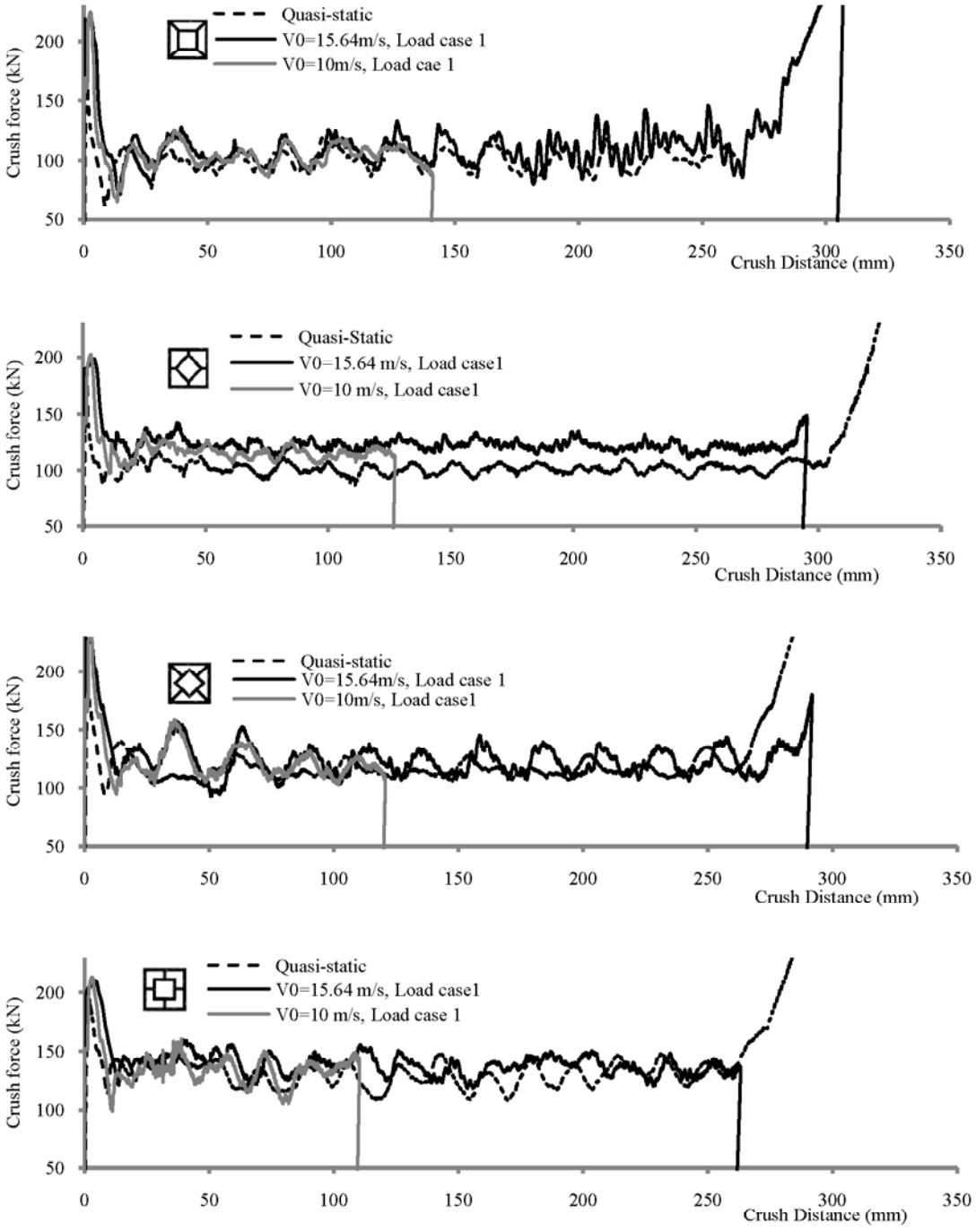

Figure 3.9

Effect of initial velocity on crush behavior of multi-cell tubes

Looking at some other multi-cell designs presented in the literature (Chen 2001, Zhang 2007), it appears that by increasing the number of cells increases the sensitivity of crush behavior to dynamic load. Figure 3.10 compares these multi-cell tubes in quasi-static and dynamic loading cases. One major reason for the difference between quasi-static and dynamic cases in rate insensitive material is because of the compatibility zone imposed on the structure due to the difference between folding heights, which appears in multi-cell tubes. These compatibility zones are the result of the difference between web sizes along with the presence of acute and/or obtuse angles.

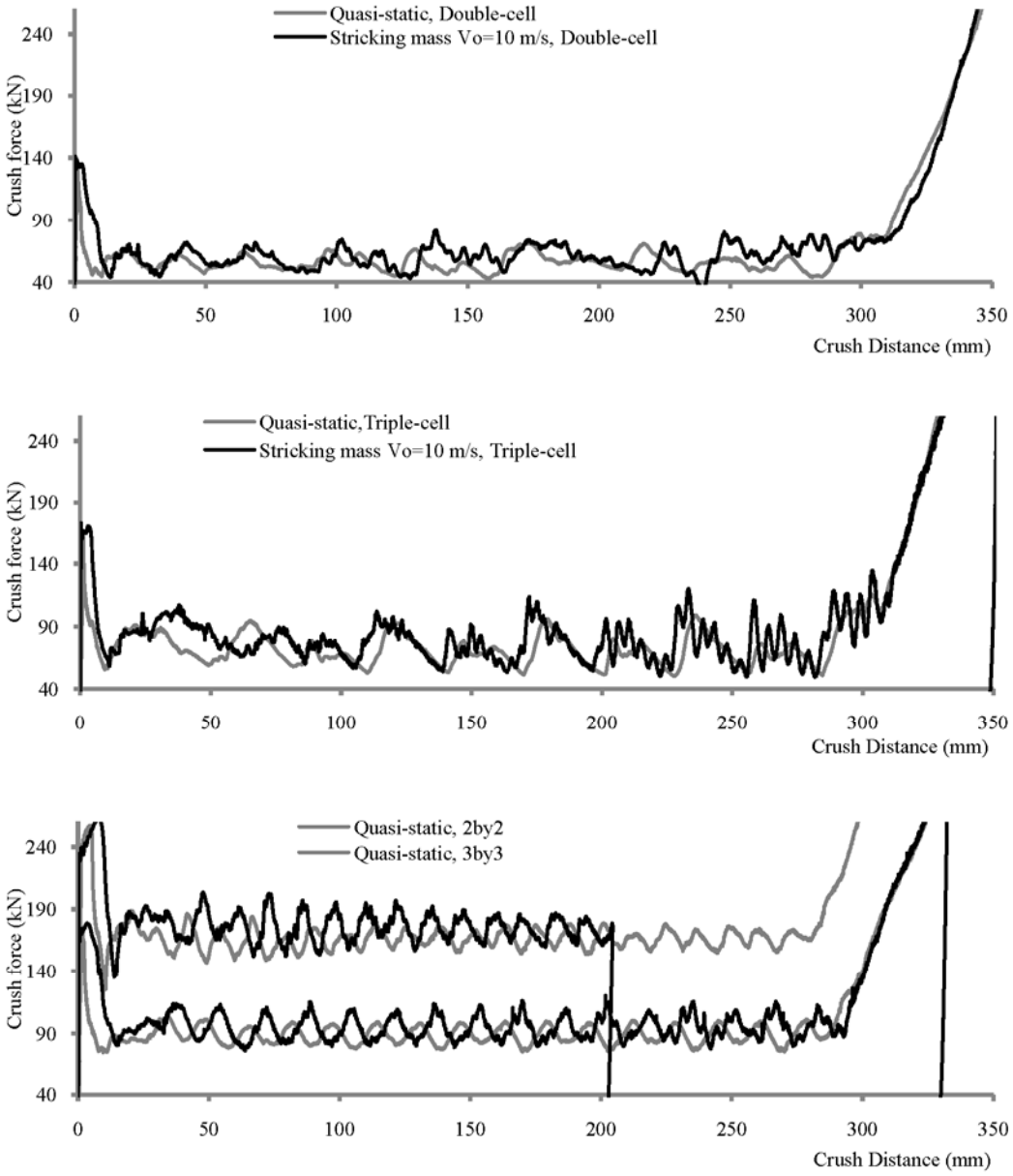

Figure 3.10

Crush behavior in multi-cell tubes

3.5 Summary

In this chapter, the effect of cross-sectional geometry on the energy absorption behavior of multi-cell multi-corner tubes was examined. Four basic multi-cell tubes were

introduced based on different methods of connection between the outer and the inner tubes that are aligned in the same longitudinal axis. This method of connection creates cells that with different angles between two webs, non-equal webs, and corners with three webs. Trigger mechanism is introduced on two opposite walls of the outer tube. Study of the crush mode shape showed that the folds have a complicated pattern depending on the angle between webs and web dimension. Nonuniform folding pattern leads to forming compatibility zones that are responsible for maintaining the structural continuity. Results show that the number of folds is highly dependent on the web size that can increase the effective folding height and reduce the crush distance. Comparing the results of multi-cell tubes with single-cell tubes shows that the peak-to-peak amplitude of the crush force decreases with multi-cell configuration. This essentially means that multi-cell tubes have less sensitivity to dynamic loading compared to quasi-static. Our study showed that increasing thickness can raise the load fluctuation while reducing the maximum crush distance. It was observed that the very small rate sensitivity parameter in aluminum alloys can affect the crush behavior. Crush behavior of load Case 1 was close to quasi-static result for all cases except for C2W (Corner to Web) case where the dynamic and quasi-static results were much different.

CHAPTER IV

ANALYTICAL PREDICTION OF ENERGY ABSORPTION IN MULTI-CELL MULTI-CORNER TUBES

Finite element analysis (FEA) provides a general framework for solving many boundary and initial value problems in structural mechanics. However, in the context of design optimization, the direct application of FEA for high fidelity simulation can be cost prohibitive, especially for nonlinear problems. Developing a closed form analytical formulation for analysis of the structural model can significantly reduce the cost of rapid evaluation of design optimization. Moreover, it can serve as a useful tool to study the key features that can help improve the design.

In this chapter, first the the general formulation of plastic collapse or limit theorem for solving the limit loads of elastic-plastic problems is introduced. Then, as a special case, the super folding element theory (Abramowicz 1989) will be introduced. This methodology considers important phenomena in the plastic collapse of thin shells such as the folding behavior, and provides an efficient method for rapid evaluation of crush tubes.

4.1 Theory of plastic collapse

In plasticity analysis, often the two most interesting results are: (a) the critical load where the solid starts to yield, and (b) the critical load where it collapses (Bower 2008). In order to solve a plasticity problem for finding the yield point, the elastic field is sufficient for the analysis. In many design problems, plastic flow must be avoided, but there are situations where some plasticity can be tolerated or even desirable such as designing crumple zones in cars. The crush tubes that are used in this study are to absorb energy during plastic deformation. In this situation, we usually would like to know the collapse load for the solid. Having this collapse load gives us some measure for energy absorption. This is the motivation for plastic limit analysis. The limit theorems of plasticity provide a quick way to estimate collapse loads, without resorting the expensive nonlinear FEA.

The early development of the theory of plastic collapse is attributed to Coulomb who in 1776 attempted to evaluate the maximum load in concrete structures and soil foundations (Ottosen 2005). The strict proof of lower and upper bound theory was given by Gvozdev (1938) and Drucker et. al. (1952) (Ottosen 2005), (Lubliner 2008). For the proof, derivation and historical remarks, interested readers are referred to Lubliner (Lubliner 2008), Calladine (Calladine 2000), and (Bower 2008). This theory states that the load cannot increase indefinitely and that the structure has a limited load capacity. The plastic collapse theorem takes two separate forms as lower bound and upper bound theorem. The lower-bound theorem can be used to perform limit load analysis by using equilibrium equation and finding the corresponding stress in the material up to yield resulting in calculation of the safety factor without considering the mode of deformation.

The upper-bound theorem is used to estimate the collapse load under which the structure is plastically deformed or slip occurs. At this critical load, the plastic region becomes large enough to allow unconstrained plastic flow in the solid provided that no kinematic and/or kinetic constraint is present. The load cannot be increased beyond this point. Therefore, the limit load will be bounded by the two values coming from lower bound and upper bound theorem. For instance, the load points A and C in figure 4.1 represent the lower bound and upper bound limits for the simple elastic-plastic beam problem shown in the figure 4.2. The lower-bound theorem can predict the load required to yield the material whereas the upper-bound theorem can predict the state of material that is completely under plastic deformation. Figure 4.2 illustrates the normal stress distributions through beam thickness corresponding to points A, B and C. It is shown that at point A, material does not experience any plasticity whereas at point C, material has become perfectly plastic, and unconstraint slip can develop without increasing the load.

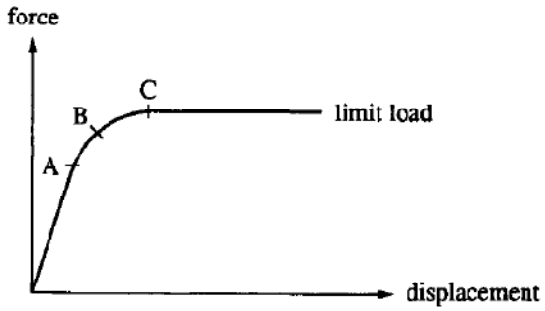

Figure 4.1

Illustration of limit load for a structure consisting of an elastic-perfectly plastic material (Ottosen and Ristinmaa 2005)

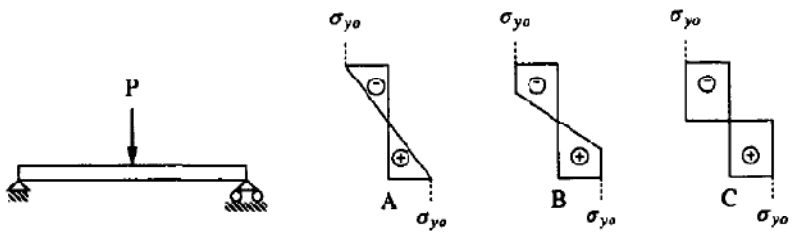

Figure 4.2

Elastic-perfectly plastic beam and the normal stress distribution at the midsection for the loading stages shown in figure 4.1 (Ottosen and Ristinmaa 2005)

The upper-bound theorem starts by identification of the deformation pattern or kinematics of deformation, and then uses energy balance between the external energy due to applied force and the internal energy generated in structure within the previously assumed kinematics. It is worth noting that the proof of the upper-bound theorem requires both normality and convexity of the yield surface known as associative flow (Lubliner 2008). Elastic-perfectly plastic model is the simplest model that can provide an analytical solution for elastic-plastic problems. This also can be extended to rigid-plastic material in cases where material experience significantly large plastic strains (Lubliner 2008). As mentioned above, the methodology is based on identification and assuming a compatible kinematically admissible deformation. This deformation can be observed through physical experiments by considering the significant modes of deformation. The assumed kinematically admissible deformation for associative flow rule, the weak form of the rate of equilibrium equitation or principle of virtual velocity can be written as the balance between external power and internal dissipated energy given by

$$\int_V \dot{\varepsilon}_{ij}\, \sigma_{ij}\, dV = \int_{S_t} \dot{u}_i\, t_i\, dS + \int_V \dot{u}_i\, b_i\, dV \tag{4.1}$$

where $\dot{\varepsilon}_{ij}$ and σ_{ij} are strain rate and stress tensors, respectively, $\dot{u}_i$, t_i and b_i are the displacement, surface, and body force vectors, respectively. S_t represents the element surface area and V represents the element volume. The kinematic parameters are derived by minimizing the above function.

Since progressive axial crush of tubes is characterized by the presence of highly localized zones of plastic flow, a similar approach as the upper-bound theorem is established for energy absorption behavior of thin walled prismatic tubes with associative materials. A displacement/velocity field is called kinematically admissible if it is continuous in the structure, satisfies the velocity/displacement boundary condition and the external force does positive work on this displacement/velocity field (Lu 2003). The limit load theorem can only be used to determine the incipient collapse mechanism, the initial load or its bounds. However, in the structures that are designed for energy absorption due to plastic deformation, they are usually expected to experience large plastic deformation under external loads. Hence, the effect of large deformation should be taken into account while using the theory of limit analysis where mainly has been captured through averaging the flow stress or energy equivalent flow stress as will be discussed later in this chapter. In the rigid-plastic model, it is necessary to have only one parameter identified as flow stress. However, based on its definition, flow stress is not constant and can vary with the amount of tangent modulus. As a simplified approach for our analytical model, energy-equivalent flow stress in extensional deformation is introduced based on the average value of the unidirectional stress-strain curve up to the final strain experienced by the structure (Wierzbicki 1999).

$$\sigma_0^N(\bar{\varepsilon}) = \frac{1}{\varepsilon_f}\int_0^{\varepsilon_f} \sigma \, d\varepsilon \tag{4.2}$$

where σ_0^N is equivalent-energy flow stress for extentional deformation, ε_f , and σ are final strain and instantaneous stress respectively.

Based on equation 4.2, the energy-equivalent flow stress depends on the final strain in the structure that may have different values in different regions of the material.

As a summary, the general assumption made here is that the material is rigid-perfectly plastic, isotropic, time-independent, isothermal, and associative as defined by the energy-equivalent flow stress.

4.2 Mechanics of progressive plastic collapse in axially compressed tubes

The mechanics of plastic collapse in axially compressed prismatic tubes is motivated by the upper-bound theorem. As mentioned earlier, the main element of this analysis include (1) energy balance equation, (2) kinematically admissible deformation, (3) proper constitutive assumption and, (4) extermum condition.

4.2.1 Energy balance equation

In this study, the thin-walled shell structure primarily undergoes plastic deformation. Ignoring the elastic part, the global balance of the rate of energy can be expressed based on equation 4.1 via

$$\dot{W}_{ext}(\dot{u}) = \dot{E}_{int}(\dot{\varepsilon}) \tag{4.3}$$

where $\dot{W}_{ext}(\dot{u})$ is the external work and $\dot{E}_{int}(\dot{\varepsilon}) = \int_V \sigma\dot{\varepsilon}\, dV$ is the instantaneous rate of energy dissipation in the plastically deformed regions. This is analogous to the balance of internal energy and the work done on a structure. The reason for choosing the term "internal dissipated energy" is that in contrast to the theory of elasticity that the energy

store in material, this process is irreversible and the amount of external work is dissipated through plastic deformation.

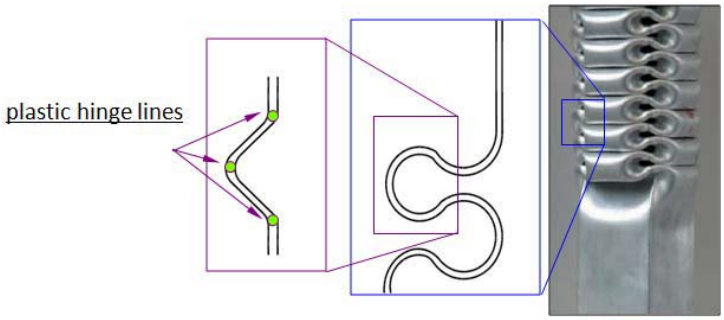

Figure 4.3

Localized plastic regions and rigid-body rotation formed during axial collapse dominated by asymmetric mode

The problem of deep plastic collapse and large shape distortion of shells include two basic deformations: rigid-body translation/rotation and localized plastic regions as shown in figure 4.3. The amount of rigid-body translation/rotation will be controlled by the plastic deformation in the localized area. The rate of external work applied on the collapsible component can be observed as the product of the effect of generalized external load and the rigid-body translation/rotation. Considering a thin-walled tube, the rate of external work can be expressed in terms of three major loads including force, moments and internal/external pressure such that

$$\dot{W}_{ext}(\dot{u}) = P\dot{u} + M\,\dot{\theta} + p\,\dot{\omega} \tag{4.4}$$

where *F, M* and *p* are the vector of applied force, moment and pressure, respectively, and $\dot{u}$, $\dot{\theta}$, and $\dot{\omega}$ are their corresponding vectors rigid-body deformations, respectively. In equation 4.4, both applied force and boundary condition can be considered. In the case of

axial crush analysis of the tube, the rate of external work is calculated based on applied axial force $P = \{P, 0,0\}$ and the axial crush velocity of $\dot{u} = \{\dot{\delta}, 0,0\}$. Hence, the expression for the rate of external work will be

$$\dot{W}_{ext}(\dot{u}) = P\,\dot{\delta} \tag{4.5}$$

For shells made of rigid-perfectly plastic isotropic materials, the rate of internal energy dissipation is divided into continuous and discontinuous velocity fields (W. Abramowicz 1989)

$$\dot{E}_{int} = \int_S \left(M_{\alpha\beta}\,\dot{\kappa}_{\alpha\beta} + N_{\alpha\beta}\,\dot{\varepsilon}_{\alpha\beta}\right) dS + \sum_{i=1}^{m} M_0^i\,\dot{\theta}^i d\iota^i \tag{4.6}$$

where *S* defines the extent of continuous plastic deformation, ι^i is the length of the i^{th} hinge line, m is the total number of stationary or moving hinge lines. In the continuously deforming zones, bending moments $M_{\alpha\beta}$ and membrane forces $N_{\alpha\beta}$ are the conjugate generalized stresses for the components of the rotation rate tensor $\dot{\kappa}_{\alpha\beta}$ and extension rate tensor $\dot{\varepsilon}_{\alpha\beta}$, M_0^i is the fully plastic bending moment per unit length (Abramowicz 1989).

4.2.2 Kinematically admissible deformation

Crush deformation of thin-walled multi-corner tubes under quasi-static and dynamic axial loads is principally governed by the collapse mechanism of the corner sections. Following a careful examination of the folding mechanisms present in a collapsing corner section of various tubes made of ductile materials, Wierzbicki and Abramowicz (Abramowicz 1989) developed a super folding element (SFE) model (figure 4.4). They concluded that the collapse is a progressive phenomenon that can be represented in terms of angle α and described by quasi-inextensional (asymmetric) and extensional (symmetric) folding modes as depicted in figure. 4.5 (a) and (b). Each fold is defined in

terms of the half-length H, the toroidal surface curvature b, the corner angle $2\pi - \psi_0$, and wall thickness t. In their generalized folding model shown in figure. 4.4, they identify the formation of 15 shell elements that are combined into five separate groups based on their response characteristics. Groups 1 and 2 consist of cylindrical and conical surfaces that have moving boundaries and undergo inextensional deformation group 3 is a toroidal surface with moving boundaries and quasi-inextensional deformation group 4 consists of conic surfaces that undergo extensional deformation and group 5 represents multiple trapezoidal elements that undergo rigid-body translation and rotation due to propagating hinge lines. What is clear in this model is that despite the drastic geometric changes, the crush process is characterized principally by localization of plastic deformation in a relatively small area of the structure (i.e. groups 3 and 4).

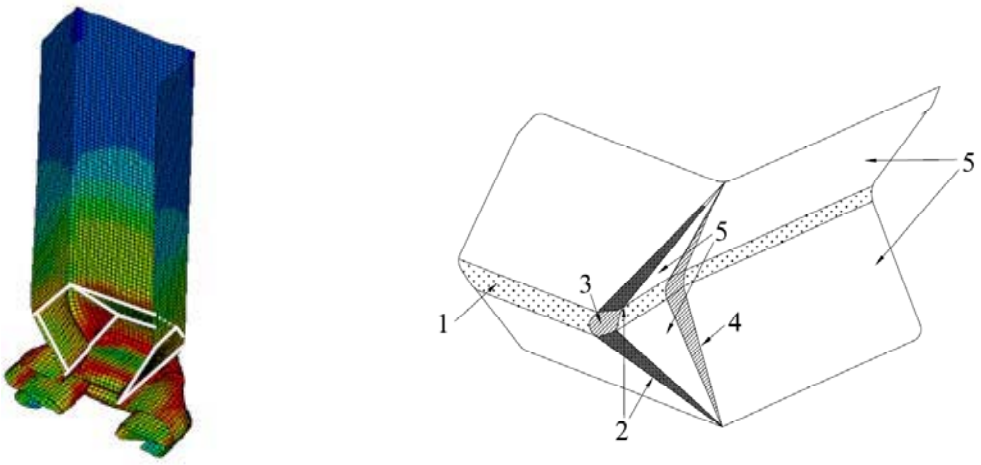

Figure 4.4

Generalized super folding element (Abramowicz 1989)

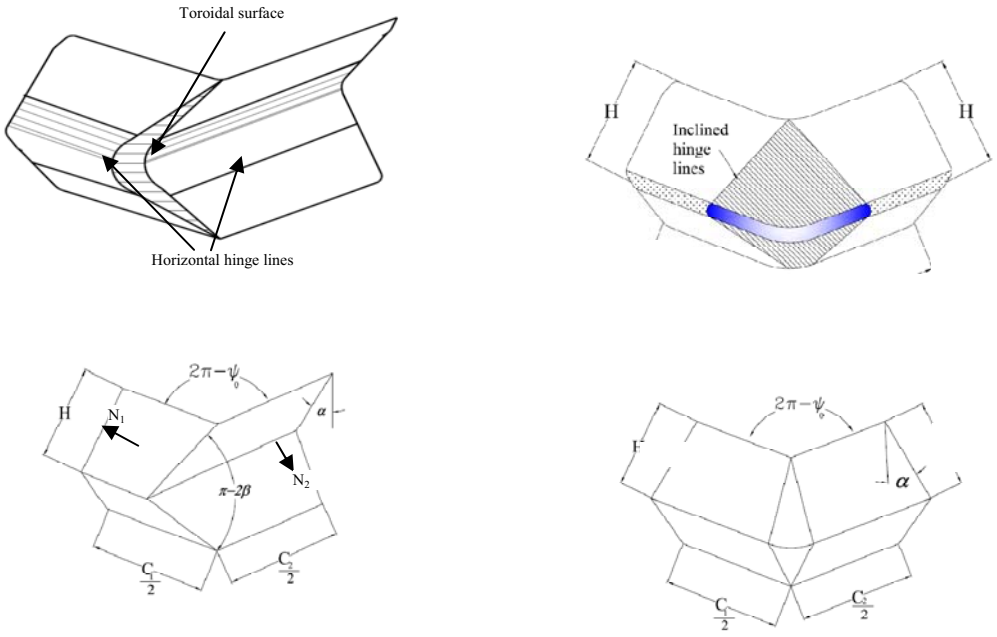

(a) Asymmetric mode $\overline{\alpha} = \alpha_f$

(b) Symmetric mode $\overline{\alpha} = 0$

Figure 4.5

Actual and simplified configuration of (a) Quasi-inextensional deformation, and (b) extensional deformation

The basic geometry of the four fold lines in asymmetric deformation is presented in figure 4.6. The initial geometry of this asymmetric mode shape is defined with the element height *2H*, total width *C*, and the corner angle $2\pi - \psi_0$. The geometry in the current configuration can be expressed via either δ which is the crush distance or the angle of rotation of side panel α (Abramowicz 1989). The geometric relations between these parameters are given as

$$\delta = 2H(1 - \cos\alpha) \tag{4.7}$$

$$S = H\sin\alpha \tag{4.8}$$

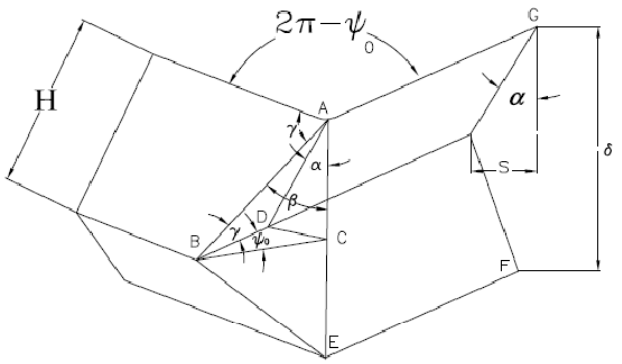

Figure 4.6

Simplified basic geometry of asymmetric element

The angles γ(in ABD plane) and β(in ABC plane) are related to ψ_0 and α through

$$\tan\gamma = \frac{\tan\psi_0}{\sin\alpha} \tag{4.9}$$

$$\tan\beta = \frac{\tan\alpha}{\sin\psi_0} \tag{4.10}$$

By taking the time derivative of equation 4.7, the relative vertical velocity between the upper and lower hinge lines (AG and EF) is found to be

$$\dot{\delta} = 2H\sin\alpha\ \dot{\alpha} \tag{4.11}$$

Similarly, the relative horizontal velocity of the middle hinge line characterized by the movement of point C toward its location after collapse (i.e. point D) is given as

$$V = \dot{S} = H\cos\alpha\ \dot{\alpha} \tag{4.12}$$

The local motion of the shell through the toroidal surface identified in figure 4.7(a) is due to the radial flow of the material described by the tangent velocity shown in figure 4.7(b) which is expressed as

$$V_t = \dot{\omega}b = \frac{V}{\tan\psi_0} \tag{4.13}$$

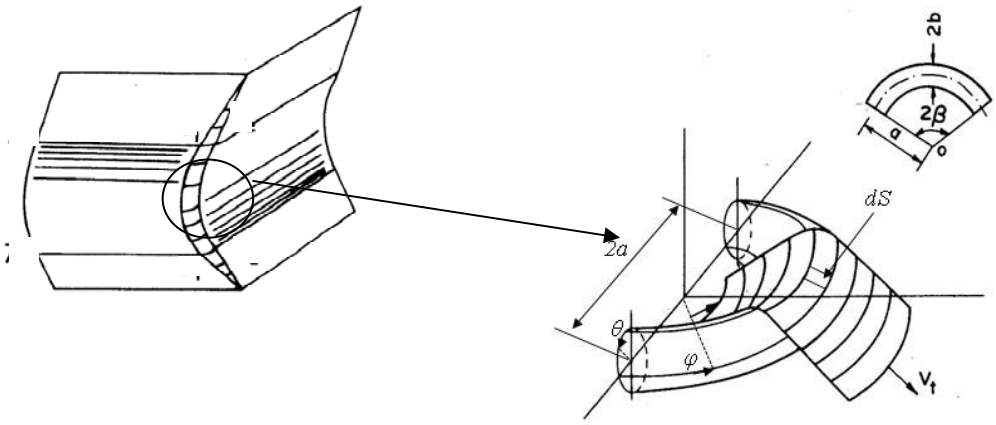

Figure 4.7

(a) toroidal surface formation in asymmetric mode (b) plastic flow of metal sheet through toroidal surface (Wierzbicki 1983)

where ώdenotes the angular velocity of the flow and b is the radius of the toroidal surface. By defining a toroidal coordinate system as $\{\theta, \phi, x\}$ where θ and ϕ denote the meridional and circumferential coordinates of the toroidal surface. The shell is assumed to be inextensible in the meridional direction that means there is no stretch rate in this direction $\lambda_\theta = 1$, the velocity vector in the toroidal coordinate system becomes

$$V = \{\dot{\omega} b, 0, 0\} \tag{4.14}$$

The kinematics of the plastic flow in toroidal surface is illustrated in figure 4.7. The integrand in equation 4.6 has six components including the energy of all the stretches and rotations. Because of the rotational symmetry and assumption of radial plastic flow all of the nondiagonal components of strain rate tensor in toroidal coordinate (figure 4.8) $(\dot{\kappa}_{\alpha\beta}, \dot{\varepsilon}_{\alpha\beta})$ are zero. Also the stretching rate in the merdional direction $\dot{\lambda}_{\phi\phi} = \dot{\varepsilon}_{\alpha\beta}$ is also assumed to be inextensible and equal to zero. The rate of stretch and curvature can be derived from (Wierzbicki 1983)

$$\dot{\lambda}_{\phi\phi} = -\frac{\dot{\omega} b \sin\theta}{r} \tag{4.15}$$

$$\dot{\kappa}_{\phi\phi} = \frac{\dot{\omega} a \sin\theta}{r^2} \tag{4.16}$$

The curvature rate for the hinge lines can be expressed as

$$[\dot{\kappa}_{\theta\theta}] = \dot{\theta} = \frac{V_t}{b} \tag{4.17}$$

Where *a* and *b* are larger and smaller radius of the toroidal surface (figure 4.7) and r is the current position of the point with θ coordinatewith repect to the axis of symmetry$r = b\cos\theta + a$.

4.2.3 Energy contributions of localized regions

The angle parameter $\bar{\alpha}$ ($0 \leq \bar{\alpha} \leq \alpha_f$), which should not be confused with α, defines the contribution of extensional deformation to the total energy dissipation. When $\bar{\alpha} = 0$, the folding mode is completely symmetric whereas for $\bar{\alpha} = \alpha_f$, the folding is purely asymmetric. In SFE, the folding process starts as an asymmetric mode that continues up to a point where the inclined hinge line is locked and the symmetric deformation begins. The actual value of $\bar{\alpha}$ depends on geometric parameters, wall thickness, and the corner angle. The geometry of all of the contributing elements can be fully described by three parameters $\{H, b, \bar{\alpha}\}$ where b is the radius of toroidal surface. These parameters are calculated from the energy balance considering the contribution of each cross-sectional element. The number of degrees of freedom in the super-folding elements is two orders of magnitude lower than that of finite element method. In other words, by describing the current state of deformation in terms of two or three free parameters, we can describe the shape function of highly distorted thin shells.

The total internal energy dissipation is obtained by integrating Eq. (4.6) in the interval range of $(0 \leq \bar{\alpha} \leq \alpha_f)$. Since deformation is based on two different folding modes that are assumed to develop in series (asymmetric followed by symmetric), the expression for the internal energy is divided into two parts and calculated as

$$E_{int} = \int_0^{\bar{\alpha}} \dot{E}_{int}^{(1)} \, d\alpha + \int_{\bar{\alpha}}^{\alpha_f} \dot{E}_{int}^{(2)} \, d\alpha \tag{4.18}$$

The two integrals in Eq. (4.18) can be decomposed as $\int_0^{\bar{\alpha}} \dot{E}_{int}^{(1)} \, d\alpha = E_1 + E_2 + E_3$ and $\int_0^{\bar{\alpha}} \dot{E}_{int}^{(2)} \, d\alpha = E_4 + E_5 + E_6$ where E_i defines the contribution of each folding mechanism to the energy dissipation, and is calculated here by considering the separate portions of the cross section based on the kinematics of the deformation expressed in figure 4.4 and 4.5. E_1 is the contribution of the toroidal surface, E_4 is the contribution of extensional deformation of conical surface, E_2 and E_5 are the energy contributions of horizontal hinge lines in symmetric and asymmetric modes, and E_3 and E_6 are the contribution of inclined hinge lines for symmetric and asymmetric modes respectively.

Based on the internal energy dissipation equation 4.18, the differential surface element *dS* shown in figure 4.7 is expressed as

$$dS = b d\theta \, r d\phi \tag{4.19}$$

4.1

where the limits for the toroidal surface are

$$\frac{\pi}{2} - \psi \leq \theta \leq \frac{\pi}{2} + \psi \tag{4.20}$$

$$-\beta < \phi < \beta \tag{4.21}$$

where 2β is the central angle of the toroidal section as shown in figure 4.7. The angle ψ is linearly increasing with ϕ from ψ_0 to $\pi/2$ according to

$$\psi = \psi_0 + \frac{\pi - 2\psi_0}{\pi}\phi \tag{4.22}$$

The yield function in the case of two nonvanishing components of the generalized strain rate tensor is

$$\left|\frac{M_{\phi\phi}}{M_0}\right| + \left(\frac{N_{\phi\phi}}{N_0}\right)^2 = 1 \tag{4.23}$$

Where $M_0 = 1/4\ \sigma_0\, h^2$ and $N_0 = \sigma_0\, h$ and h represents the current thickness of the shell. With this and assuming associated flow rule, the continuous rate of energy dissipation can be uniquely determined.

Since the effect of thickness variation is small except for problems in which the ratio of $\eta = \frac{b}{h}$ is relatively large (for instance outside-in tube inversion problems (Wierzbicki 1983)), in this study, two other η is assumed to be small thickness is kept constant. As shown previously in finite element analysis, these two assumptions have good agreement with the computational results. As mentioned previously, the major energy dissipation occurs during the early deformation (when α is small) with no considerable thinning in the shell. During the formation and development of the toroidal surface, general internal energy dissipation can be expressed with the first integral of the equation 4.6. Therefore, the first term in internal energy contributions (equation 4.18) in toroidal coordinate system for the toroidal surface is a double-integral equation expressed as

$$\dot{E}_1 = \int_{-\beta}^{\beta} b \left\{ \int_{\pi/2-\psi}^{\pi/2+\psi} \left[M_0 \frac{\dot{\omega} a \sin\theta}{r^2} + N_0 \frac{\dot{\omega} b \sin\theta}{r} \right] r\, d\theta \right\} d\square \tag{4.24}$$

Doing the first integration

$$\dot{E}_1 = \int_{-\beta}^{\beta} \left\{ 2\,\dot{\omega}\, b^2 N_0 \sin\psi + \dot{\omega} b\, M_0\, 1/\eta \ln\left(\frac{1+\eta\sin\psi}{1-\eta\sin\psi}\right) \right\} d\square \tag{4.25}$$

For the small values of η, the second term can be approximated by selecting the first (linear) term of power series, which yields

$$\dot{E}_1 = \int_{-\beta}^{\beta} \{2\, \dot{\omega}\, b \sin\psi\, [N_0 b + M_0]\}\, d\square \tag{4.26}$$

The dependence of the solution on the larger radius is neglected for the small value of *a*. The first integrant term shows the contribution of circumferential extension where as the second term represents the contribution of continuous bending. In the two-flange corners, since wall thickness is usually four times greater than the radius (Abramowicz 1983), continuous bending can be neglected in equation 4.26. It is been founded that the small η is reduced to a single point on the yield condition ($M_0 = 0$) (Abramowicz 1983). Considering only the first integrant of equation 4.6 together with equations 4.26 results in:

$$\dot{E}_1 = \frac{4\, N_0 b H \pi}{(\pi - 2\psi_0)\tan\psi_0} \cos\alpha \left\{ \sin\psi_0 \sin\left(\frac{\pi - 2\psi_0}{\pi}\right) \beta + \cos\psi_0 \left[1 - \cos\frac{\pi - 2\psi_0}{\pi}\beta\right]\right\} \dot{\alpha} \tag{4.27}$$

Integrating the above equation over the whole collapse process gives

$$E_1(\psi_0, \bar{\alpha}) = \int_0^{\bar{\alpha}} \dot{E}_1 d\alpha = 16\, M_0\, I_1(\psi_0, \bar{\alpha})\, \frac{Hb}{t} \tag{4.28}$$

where

$$I_1(\psi_0, \bar{\alpha}) = \frac{\pi}{(\pi - 2\psi_0)} \int_0^{\bar{\alpha}} \cos\alpha \left\{ \sin\psi_0 \sin\left(\frac{\pi - 2\psi_0}{\pi}\beta\right) + \cos\psi_0 \left[1 - \cos\left(\frac{\pi - 2\psi_0}{\pi}\beta\right)\right]\right\} d\alpha \tag{4.29}$$

The contribution of the horizontal hinge lines are expressed in $\dot{E}_2$. As it is shown in figure 4.5, there are two horizontal hinge lines in each side of the basic folding element.

The energy dissipation of horizontal hinge lines are resulted from the discontinuous velocity fields, where the second term in equation 4.6 is given as

$$\dot{E_2} = M_0 C_1 \dot{\alpha} + M_0 C_2 \dot{\alpha} \tag{4.30}$$

where C_1 and C_2 are SFE flange sizes defined in figure 4.5 then, the energy term in the horizontal hinge line in basic folding element is

$$E_2 = \int_0^{\bar{\alpha}} \dot{E_2}\, d\alpha \tag{4.31}$$

and for the equal flange size it can be written as

$$E_2(\bar{\alpha}, C) = 2\, M_0 C\, \bar{\alpha} \tag{4.32}$$

It is worth noting that for energy dissipation calculation, the horizontal hinge line is assumed to be simply supported. This energy dissipation will be changed due to the horizontal boundary condition of folding mechanism.

The energy dissipation contribution of the inclined hinge lines are included in E_3. The length of the inclined hinge lines (line ABE in figure 4.6) changes during the crush process with the kinematic relation

$$L = 2H / \sin\gamma \tag{4.33}$$

Where L is the length of inclined hinge line. For more accurate calculations, the larger radius of toroidal surface "b" should be used in this calculation (Wierzbicki 1983). The inclined hinge line consists of two segments of assumed straight lines and an arc of the circle defined by the radius r_0 and central angle of 2β (figure 4.5).

The rate of rotation is constant along L and equal to

$$\dot{\theta} = V_t / b \tag{4.34}$$

Having two inclined hinge lines in nontapered tube, the energy equation based on the second term of equation 4.6 can be written as

$$\dot{E}_3 = M_0 L\dot{\theta} + M_0 L\dot{\theta} = 2M_0 L\dot{\theta} \tag{4.35}$$

Substituting equation 4.34 and 4.33 into equation 4.35 yields:

$$\dot{E}_3 = 4M_0 \frac{H^2}{b} \frac{1}{\tan\psi_0} \frac{\cos\alpha}{\sin\gamma} \tag{4.36}$$

After integrating over α, we find

$$\dot{E}_3(\psi_0) = 4M_0 I_3(\psi_0) \frac{H^2}{b} \tag{4.37}$$

where

$$I_3(\psi_0) = \frac{1}{\tan\psi_0} \int_0^{\bar{\alpha}} \frac{\cos\alpha}{\sin\gamma} d\alpha \tag{4.38}$$

The phase two of deformation which is the symmetric mode, the second integral in equation 4.18 . This mode consist of the formation of conical zone along with the formation/continuation of the horizontal and vertical hinge lines. The material in the conical zone stretches in the meridional direction, θ. Owing to continuous deformation, the first term in equation 4.6 is sufficient to express the rate of energy dissipation in this region. Assuming inextensional deformation in ϕ direction, and neglecting the shear and rotation components, E_4 can be expressed as

$$\dot{E}_4 = \int_S N_0 \dot{\lambda}_{\theta\theta} \, dS \tag{4.39}$$

where *S* is the current area of the conical surface (figure 4.5b). The final expression for the energy dissipation contribution of conical surface can be expressed as:

$$\dot{E}_4 = \int_S N_0 \dot{\lambda}_{\theta\theta} \, dS = 2 M_0 V_t \frac{H}{t} \tag{4.40}$$

where V_t or the tangential velocity for the conical surface based on the rate of stretching is

$$V_t = \frac{H}{\sin^2\gamma}\dot{\gamma} \tag{4.41}$$

The final expression for the energy contribution considering two identical conical zones is

$$E_4 = 2\,M_0\,\frac{H^2}{t}\int_{\psi_0}^{\alpha_f}\frac{d\gamma}{\sin^2\gamma} \tag{4.42}$$

The rate of energy dissipation for the horizontal hinge lines in the second phase is derived similar to equation 4.30 as

$$E_5 = \int_{\bar{\alpha}}^{\alpha_f}\dot{E_5}\,d\alpha \tag{4.43}$$

That means for equal flange size, *E_5* becomes

$$E_5(\bar{\alpha}, \alpha_f, C) = 2\,M_0\,C\,(\alpha_f - \bar{\alpha}) \tag{4.44}$$

During the second phase of deformation (second term in equation 4.6), the inclined hinge line AB is fixed (figure 4.6) A the same time, the angle between the planes that intersect AB varies

$$\sin\theta_1 = \frac{\tan\psi_0}{\sqrt{\tan^2\psi_0 + \cos^2\phi}} \tag{4.45}$$

This relation resulted from the angle between two surface normals in figure 4.6 as:

$$N_1 = \{0, \cos\alpha, \sin\alpha\} \tag{4.46}$$

$$N_2 = \{\cos\alpha\sin 2\psi_0, \cos\alpha\cos 2\psi_0, -\sin\alpha\} \tag{4.47}$$

The angle between two planes can be described by the angle between its two normals as

$$\cos 2\theta_1 = 2\cos^2\alpha\,\cos^2 2\psi_0 - 1 \tag{4.48}$$

So the energy dissipation of the two hinge lines can be calculated as

$$\dot{E}_6 = M_0 L 2\dot{\theta} = 2M_0 H \frac{\sin\alpha\,(\sin^2\alpha+\tan^2\psi_0)}{\tan\psi_0(\sin^2\alpha+\tan\psi_0\sin^2\alpha)} \tag{4.49}$$

Integrating $\dot{E}_6$ within the range of $(\bar{\alpha}, \alpha_f)$ results in

$$\dot{E}_6(\psi_0, \bar{\alpha}) = M_0\, H\, I_6(\psi_0, \bar{\alpha}) \tag{4.50}$$

with

$$I_6(\psi_0, \bar{\alpha}) = \frac{2}{\tan\psi_0}\int_{\bar{\alpha}}^{\alpha_f} \frac{\sin\bar{\alpha}\,(\sin^2\bar{\alpha}+\tan^2\psi_0)}{\sin^2\bar{\alpha}+\tan^2\psi_0\sin\alpha}\, d\alpha \tag{4.51}$$

Where the angles α, β and ψ_0 are defined in figure. 4.6 while flange dimension C is defined in figure. 4.5

4.2.4 Constitutive assumption and energy equivalent flow stress

Material behavior in this analysis is assumed to be rigid-perfectly plastic. This is proven to be very useful in deriving the approximate solution for plane plasticity problems including slip line theory (Bower 2008, Lubliner 2008) and structural problems including limit load analysis discussed earlier. These theories consider the incipient plastic flow. Therefore, the material can be characterized by a single parameter called flow stress. This is basically valid when the elastic strain is negligible compared to plastic strain. The plastic strain rate and total strain are equal in the original proof of Saint-Venant-Levy-Mises flow rule (Lubliner 2008, Hill 1998). This treatment is equivalent to treating the nonvanishing elastic modulus as infinite. Any solution obtained based on this theory is valid for the rigid-perfectly plastic material or Mises theory. The upper-bound theorem is valid for this assumption owing to associative material in which convexity and normality of the yield surface are satisfied.

In contrast to small strain plasticity, a proper formulation of energy absorption problems requires the consideration of a number of new effects including: inhomogeneous strain fields, complex strain histories under monotonic loading, kinematic vs. isotropic hardening rule, fracture initiation and propagation (Wierzbicki 1999). In the literature most of the researchers (Abramowicz 1984, 1989, Hanssen 2000, Langseth 1996) calculated the average flow stress based on simple averaging assumption shown in equation 4.2, but this should be used with caution. This assumption is valid provided the strain value in the entire localized region is uniform. The Baushinger effect is ignored and no failure and damage is considered. The calculation of energy equivalent flow stress is one of the major sources of discrepancies between the mean crush force calculated from analytical equation and that of experiment (Wierzbicki 1999). The nonuniform strain in the hinge lines can be modified by calculating the actual strain from the kinematics of deformation such that the final strain ε_f in equation 4.2 appropriately calculated (Abramowicz 1989). To calculate the equivalent flow stress, power law is widely used due to it good performance and simplicity. As shown in chapter 2, the strain history in some regions includes both loading and unloading. Baushinger effect can also be taken into account where the effects of both kinematic and isotropic hardening are considered. Hence the general equation for the energy-equivalent flow stress is given as (Wierzbicki 1999).

$$\sigma_0 = \frac{\sigma_u}{n+1}\left\{\frac{1}{2}\left(\frac{\varepsilon_f}{\varepsilon_u}\right)^n + \left(2^n - \frac{1}{2}\right)\beta\left(\frac{\varepsilon_f}{\varepsilon_u}\right)^n + \frac{1}{2}(1-\beta)\frac{n+1}{m+1}\left(\frac{\varepsilon_f}{\varepsilon_u}\right)^m\right\} \qquad (4.52)$$

where σ_u, $\varepsilon_u$and ε_f are ultimate stress, strain corresponding to ultimate stress and maximum attained strain at which strain reversal begins respectively, and n, m and β are the exponent of monotonic power law curve, exponent of reverse strain power law, and

parameter describing relative magnitude of isotropic and kinematic hardenings, respectively. For the pure isotropic hardening case $\beta=1$, $m=n$, $\varepsilon_f=\varepsilon_u$., and the energy-equivalent flow stress is simplified to

$$\sigma_0 = \frac{\sigma_u}{n+1} 2^n \tag{4.53}$$

Kinematic hardening is obtained by setting $\beta=0$, $m=n$, $\varepsilon_f=\varepsilon_u$., which gives

$$\sigma_0 = \frac{\sigma_u}{n+1} \tag{4.54}$$

As mentioned earlier in the general form of equation 4.2, the energy equivalent flow stress is defined based on the value of maximum attained strain or final strain. Each region in super folding element has its own strain value. Measuring the strain in each region provides a better prediction of the mean crush force. Wierzbicki (Wierzbicki 1989, 1999) showed that the strain in three localized regions including horizontal hinge line ε_1, inclined hinge lines ε_2 and inextensional deformation in an asymmetric element ε_3 (figure 4.6) are

$$\varepsilon_1 = 1.3 \left(\frac{t}{b}\right)^{2/3} \tag{4.55}$$

$$\varepsilon_2 = 0.65 \left(\frac{t}{b}\right)^{1/3} \tag{4.56}$$

$$\varepsilon_3 = 0.64 \left(\frac{t}{b}\right)^{1/3} \tag{4.57}$$

These values should be used in calculation of energy equivalent flow stress (equation4.2). It has been shown shown (Wierzbicki 1999) that the values of strain in different regions are approximately equal for a wide range of C/t varies between 10%-20%.

4.2.5 Extermum condition

The existence of this optimum path is shown by Hill (Hill 1998) for the theory of plastic collapse, and was recently proven for axial crush (Abramowicz 1996). To preserve energy balance, the total internal energy defined by the sum of individual contributions has to be equal to the external work done by the axial crush force (equation 4.5), which can be rewritten as

$$\dot{W}_{ext}(\dot{u}) = P_m \dot{\delta}_{eff} \tag{4.58}$$

where P_m is the mean crush force and δ_{eff} the associated effective crush distance. This assumption helps us to include the real crush distance, which will be discussed later. The criterion for calculating the mean crush force is derived by minimization of mean crush force as a postulate (Wierzbicki 1983), (Wierzbicki 1983) for a minimum condition (Zhang 2007). Wierzbicki and Abramowicz (Abramowicz 1989) mentioned that the validity of this assumption was vague and needed a rigorous proof. This problem was resolved later (Abramowicz 1996). Following the framework of (Abramowicz 2003), the minimum condition for the mean crush force for the defined kinematic parameters is provided below in a simple form for the case of axial crush.

Here, we have three kinematic parameters that should be identified to calculate the mean crush force. Due to the limitation that has already been imposed onto the set of kinematically admissible deformation, the boundary condition, initial condition and loading are automatically satisfied. Also the deformation gradient is also satisfied due to selecting the kinematically admissible deformation field in a simply connected domain. Consequently, the compatibility conditions are automatically satisfied.

The principle of virtual velocity can be expressed as the functional J defined as

$$J = \dot{E}_{ext} - \dot{E}_{int} \tag{4.59}$$

In order to solve this functional, we need to define a set of trial admissible deformation parameters defined by $\beta^* = \{H^*, b^*, \overline{\alpha}^*\}$. With this, a set of trial functionals J^*can be defined as:

$$J^* = \dot{E}^*_{ext} - \dot{E}^*_{int} \tag{4.60}$$

Each trial functional J^* corresponds to a trial admissible deformation $x^* = \chi^*(X, \beta^*, t)$

Since deformations are finite in reality, $x = \chi(X, \beta, t)$and trial $x^* = \chi^*(X, \beta^*, t)$may occupy different regions that is the limits in the actual functional and trial one can be different except in the initial condition. Hence, as the general approach, the equilibrium of the body can be expressed by requiring the vanishing of the residual value that should be vanished at each time instant

$$\Re = J^* - J \tag{4.61}$$

Since we have assumed that crush is a quasi-static process under kinematic loading, the trial external power (energy rate) and actual external power are the same.

$$\dot{E}^*_{ext} = \dot{E}_{ext} \tag{4.62}$$

Therefore, residual equation 4.62 can be written as

$$\Re(\beta, t) = \dot{E}^*_{int} - \dot{E}_{int} : t \in [\tau_0, \tau_f] \tag{4.63}$$

where time *t* is defined in the range of initial state (τ_0) to final state (τ_f)

Thus, to achieve equilibrium, the residual value should be minimized to zero

Based on equation 4.63 and the upper bound theorem of the theory of plasticity, the internal energy should be minimized for $b, \overline{\alpha}$ That is

$$\frac{\partial \dot{E}_{int}}{\partial b} = 0, \frac{\partial \dot{E}_{int}}{\partial \bar{\alpha}} = 0 \tag{4.64}$$

From equation 4.59, the functional is minimized with respect to H

$$\frac{\partial J}{\partial H} = \frac{\partial (\dot{E}_{ext} - \dot{E}_{int})}{\partial H} = \frac{\partial \dot{E}_{ext}}{\partial H} - \frac{\partial \dot{E}_{int}}{\partial H} = 0 \tag{4.65}$$

And from equation 4.58

$$P_m \delta_{eff} = E_{int} \tag{4.66}$$

Assuming $\delta_{eff} = \varrho\, 2H$ and based on equation of J minimization

$$\frac{\partial E_{ext}}{\partial H} = \frac{\partial E_{int}}{\partial H} \tag{4.67}$$

That the right hand side of equation 4.67 is

$$2\varrho\, P_m = \frac{\partial \dot{E}_{int}}{\partial H} \tag{4.68}$$

From 4.66 and 4.68 we have

$$\frac{\partial E_{int}}{\partial H} = \frac{E_{int}}{H} \tag{4.69}$$

It can be shown that the above equation is equivalent to

$$\frac{\partial P_m}{\partial H} = \frac{\partial}{\partial H}\left(\frac{E_{int}}{\varrho H}\right) = 0 \tag{4.70}$$

It can be easily concluded that the extermal value of the kinematically admissible parameters $\{H, b, \bar{\alpha}\}$ derived from the minimization of the mean crush force:

$$\frac{\partial P_m}{\partial H} = 0, \frac{\partial P_m}{\partial b} = 0, \frac{\partial P_m}{\partial \bar{\alpha}} = 0 \tag{4.71}$$

As presented in the previous chapter, the use of trigger mechanism led to the collapse of tubes in asymmetric mode shape. This means that the $\frac{\partial P_m}{\partial \bar{\alpha}} = 0$ term is not necessary to be satisfied , the angle parameter will be $\bar{\alpha} = \frac{\pi}{2}$ in this case. In the case of symmetric mode shape, the angle parameter turns into the other extreme i.e. $\bar{\alpha} = 0$. Although in the

presence of trigger mechanism the second term in equation 4.18 becomes zero, the general deformation discussed in this chapter will be used for formulating the problem of multi-cell tubes.

4.2.6 Effective crush distance and contact effect

The effective crush distance is used to calculate the external energy from equation 4.58. This relation should balance the internal dissipated energy and external work to find the mean crush force. Therefore, there is an inverse relation between mean crush force and the effective crush distance. Experimental and numerical observation show that the folds are not in a plane surface and there is a curvature associated with this distance. As shown in chapter 2, the double bending process of the walls creates a folding pattern as shown in figure 2.17. The effective crush distance is defined as $\delta_{\text{eff}} = \varrho\ 2\text{H}$. In the case of complete contact, where both faces of non-deformed components (region 5 in figure4.4) are collapsed completely on each other, $\varrho = 1$. In practical cases this condition never happens and may result in under-predicting the mean crush force. Abramowicz (Abramowicz 1983) showed that the factor ϱ varies within a range of 0.60-0.75 percent for linear strain hardening materials in single cell square tubes. This factor also depends on the corner angle and the cross sectional shape.

Two simplified mode shapes considered in this study as depicted in figure 4.9. These modes are distinct from each other by the radius of the inward and outward lobes. In one case, the radius are equal (figure 4.9a) and in the other case the radius of the inward lobe is half of the radius of the outward lobe (figure 4.9b). The ratio of the effective crush distance and projected fold length (2H) can be calculated for figure 4.9a as

$$\frac{\delta_{eff}}{2H} = 1 - \frac{x_{eff}}{2H} = 1 - \frac{R_f}{(\sqrt{3}+2)R_f} = \sqrt{3} - 1 = 0.73 \quad (4.72)$$

And for figure 4.9b case:

$$\frac{\delta_{eff}}{2H} = 1 - \frac{x_{eff}}{2H} = 1 - \frac{R_f}{(\frac{\sqrt{5}}{2}+\frac{3}{2})R_f} = \frac{1}{2}\left(\sqrt{5} - 1\right) = 0.62 \quad (4.73)$$

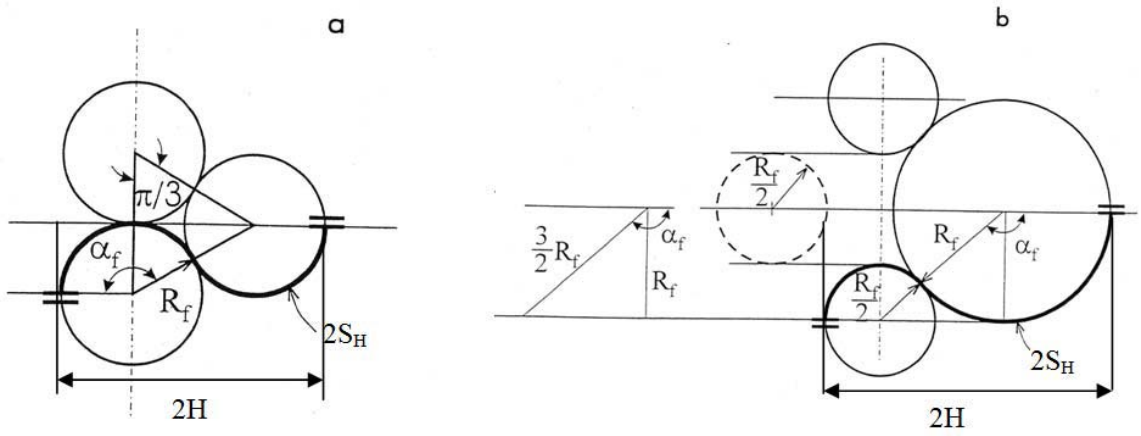

Figure 4.8

Formation of folds for crush distance calculation for (a) equal-size lobes, and (b) different size lobes (Wierzbicki 1999)

Hence, the constant ϱ can take values within 62% to 73% based on the tube crush mode, wall thickness and cross sectional geometry.

With this, we have a consistent framework for characterizing the energy absorption properties of structures. However, this solution needs to consider the effective crush distance to have a proper value for external energy applied to the structure. Other effects such as mode instability due to imperfection and thickness effect, buckling mode, material behavior, failure behavior, and more importantly dynamic behavior are ignored. In the next section, some features regarding the dynamic behavior will be addressed.

4.3 Effect of dynamic loading

Experimental studies showed that in perfectly prismatic square tubes the energy absorption behavior under dynamic impact changes due to inertia effects (Reid 1996, Langseth 1996, Karagiozova 2008). Inertia effects are sensitive to the initial straightness of the specimens. In quasi-static case, the deformation occurs predominately by rotation of plastic hinges. Unlike the quasi-static theory of progressive plastic collapse, which assumes inextensional deformation in the hinge lines, in dynamic loading, a straight structure goes into axial compression due to the initial velocity. This will affect the initial peak load that was discussed in chapter 2. This effect can be described in terms of the elastic-plastic wave propagation. Stress wave propagation or inertia effect mainly influences the mode of deformation as described in chapter 2. Karagiozova showed that the initial out-of-plane deformation in structures under impact changes by the initial velocity that caused adjustment of the crush mode shape (Karagiozova 2004b). They showed that the speed of plastic stress wave depends on the stress state and the direction of wave propagation. This phenomenon initiates the buckling pattern and remains unchanged while large displacements develop. They have shown that two plastic stress waves travel with two velocities called slow and fast plastic stress. Material hardening has a stronger effect on the slow plastic wave speed while state of stress affects both fast and slow plastic wave speeds. Embedding the effect of stress wave propagation on the analytical equation developed in the previous section is not possible. The theory described above requires an identified crush mode, which is subject to change in the presence of dependency of the initial buckling mode formation on parameters such as hardening and initial velocity. We also showed that the trigger mechanism in the form of

indentation can eliminate this effect. This effect will not be captured through the analytical method described here.

4.3.1 Strain rate sensitivity

Abramowicz and Jones (Abramowicz 1984)used the empirical Cowper-Symonds uniaxial constitutive equation (equation 4.74) to modify the energy equivalent flow stress used to derive the mean crush force such that

$$\frac{\sigma_{0d}}{\sigma_0} = 1 + \left(\frac{\dot{\varepsilon}}{D}\right)^p \tag{4.74}$$

where the values for AA 6060-T6 and AZ31 are ($D=1288000s^{-1}$, $p=4$) (de Kanter 2006) and ($D=570s^{-1}$, $p=3$). The average strain rate due to a dynamic load applied by a striking mass with an initial velocity of V_0 can be found as

$$\dot{\varepsilon} = \frac{h\,V_0}{2\,b\,\delta_{eff}} = \frac{h\,V_0}{4\,b\varrho H} \tag{4.75}$$

Substituting equation 4.74 in to 4.75 gives the modified energy equivalent flow stress with the strain rate effect included

$$\sigma_{0d} = \sigma_0\left(1 + \left(\frac{h\,V_0}{4\,b\varrho HD}\right)^{1/p}\right) \tag{4.76}$$

σ_{0d} value should replace the flow stress in the mean crush force calculation.

4.3.2 Reduction in effective crush distance due to high velocity impact

Figure 2.29 and 2.24 showed that the lobe shape changes by increasing the initial velocity. The schematic shape is shown in figure 4.9, such that the lobe pattern changes from quasi-static configuration (4.9a) to figure 4.9b. Based on quasi-static mode shape (figure 4.9a), the actual fold length can be derived from

$$2S_H = 2.4\left(\frac{R_{fl}}{2} + R_{fl}\right) \tag{4.77}$$

The actual fold length based on figure 4.9a configuration is

$$2S_H = \frac{5\pi}{6}(2R_{f2}) \tag{4.78}$$

Assuming that the actual fold length stays constant during the course of deformation, the effective crush distance should be modified according to

$$\frac{\delta_{Deff}}{\delta_{eff}} = \frac{R_{f2}}{R_{f1}} = 0.69 \tag{4.79}$$

4.4 General approach for multi-cell prismatic tubes

The quasi-static mean crush force of multi-cell prismatic tubes is considered based on the deformation mechanism described in the previous section. Figure 4.10 Illustrates four different multi-cell configurations. When divided into its distinct corner sections, each cross-section is characterized by two- and three-flange elements. The two-flange elements are described by the width dimensions C_1 and C_2 whereas the three-flange elements include an additional flange with width C_{sh}. All members have the same thickness t. Table 1 shows the distribution of decomposed elements in multi-cell models C2C, C2W, W2C, and W2W.

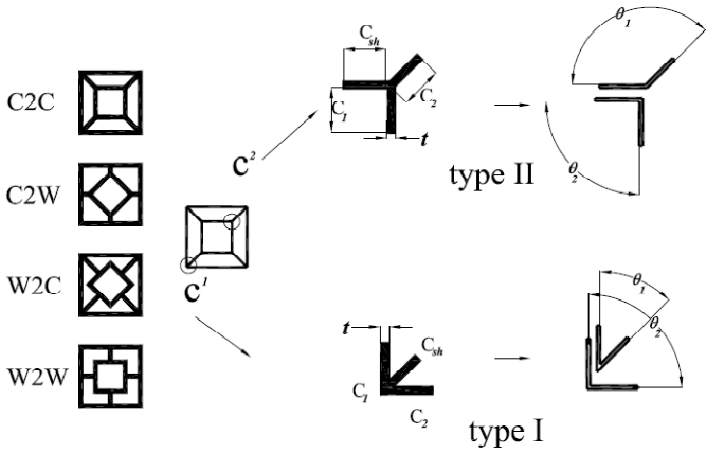

Figure 4.9

Alternative cross-sectional models for multi-cell tubes (Najafi 2008)

Three types of three-flange elements identified as types I and II and T in figure. 4.10, are considered. Type I element has two obtuse angles while type II has two acute angles. Simple T elements present in models C2W, W2C and W2W are treated as a combination of two right angle corners.

Table 4.1

Distribution of corner elements in multi-cell tubes.

Model	2-flange elements	3-flange elements (type I)	3-flange elements (type II)	3-flange Elements T-Shape
C2C	0	4	4	0
C2W	4	0	4	4
W2C	4	4	0	4
W2W	8	0	0	8

Based on the super folding element theory described in previous sections, the deformation mode in multi-cell tubes is decomposed into the basic deformation described

in figure 4.5. Figure 4.11 shows the deformation mode of a three-flange corner with obtuse angle. Based on the finite element simulation, the deformation region can be described in terms of basic deformation pattern shown in figure 4.11.

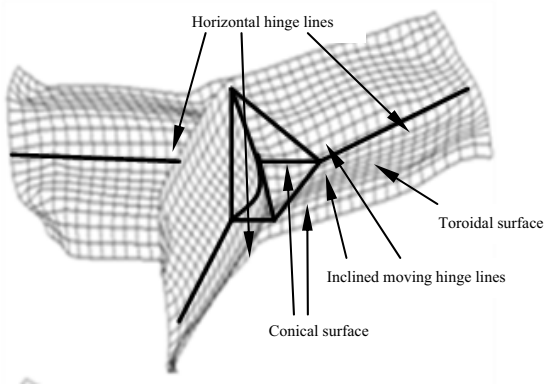

Figure 4.10

Plastic deformation pattern in type II corner section

Toroidal surface will be formed mainly between obtuse angles, so the energy dissipation contribution due to toroidal surface is derived from equation 4.28 between obtuse angles. In general, the numbers of horizontal hinge lines are based on the number of flanges in the model. Hence, for three flange elements there are three horizontal hinge lines related to each flange C_1, C_2, C_{sh} with clamped boundary condition such that

$$E_2 = 2M_0(C_1 + C_2 + C_{sh})\alpha \tag{4.80}$$

where in our analysis$\alpha = \frac{\pi}{2}$ and $M_0 = \frac{\sigma_0 t^2}{4}$ since the thickness is constant in all the walls. Two inclined moving hinge lines are observed. Using the inclined moving hinge lines present in the asymmetric mode of deformation can be derived from equation 4.37. Two

conical surfaces are identified resulting from the symmetric mode shape of the super folding element. Thus, the corresponding internal energy is found as

$$E_4 = M_0 V_t \frac{H^2}{t} \int_{\psi_0}^{\alpha_f} \frac{d\gamma}{\sin^2\gamma} \tag{4.81}$$

Comparing equations 4.81 and 4.42, it appears that the conical surface in the actual two-flange element is 2 times higher than that of used in the three flange assembly because of the fact that this deformation assumed to be confined to one flange only.

Figure 4.12 summarizes the calculation of the plastic deformation in each three-flange element based on the basic deformation in supper folding element. As it is shown type I and T shape corners can be decomposed in to a complete pure asymmetric element and half of pure symmetric element, whereas, the type II corners are decomposed into a combination of one and half pure asymmetric super folding elements.

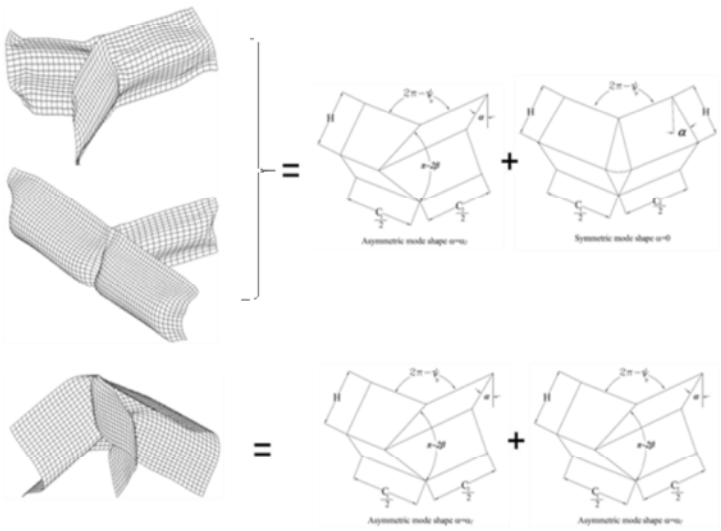

Figure 4.11

Decomposition of three-flange corners to basic elements

With this assumption, the basic folding elements for obtuse angle type I and T-shape are expressed in terms of one asymmetric right angle and one symmetric super folding elements described in the previous section. The basic folding element of the acute angle, which has been introduced as type II, is described as a combination of two asymmetric super folding elements. The resulting energy equations for each type can be expressed

Type I and T-shape:

$$\underbrace{\qquad\qquad}_{\text{Asymmetric mode}}\ \underbrace{\qquad}_{\text{Symmetric mode}} \tag{4.82}$$

Type II:

$$\underbrace{\qquad\qquad}_{\text{Asymmetric mode}}\ \underbrace{\qquad\qquad}_{\text{Asymmetric mode}} \tag{4.83}$$

It is important to note that each angle θ in figure 4.10 represents the angle ψ_0 in energy contribution equation of corner section. The total energy dissipation for multi-cell

models C2C through W2W can be obtained by adding the contribution of individual corner elements, which together with Eq. (14) provides a closed form formula for the mean crush force

$$P_m = \frac{1}{2\square H}\sum_{j=1}^{n_e} N_j E_{int}^j \tag{4.84}$$

where N_j represents the number of each distinct corner elements from table 4.1 with separate contributions to the total energy absorption of the tube, and n_e represents the number of element types present in the cross-section. Since Eq. (4.84) is based on a single value for equivalent projected fold length, H, some error will be introduced in the estimated value of P_m for crush cases with non-uniform fold geometries.

Following the minimization equation 4.71 for H and b in previous section, the equivalent H and b for multi-cell elements can be obtained from equation 4.85 and 4.86 below where all the constants have been specified in the Table 4.2.

$$b_{eq} = -\frac{t\beta}{4\lambda} - \frac{\xi}{4\sqrt{3}} + \frac{1}{2}\varsigma \tag{4.85}$$

$$H_{eq} = \frac{1}{t\eta}\left(\frac{t^2\beta^2\gamma}{4\lambda^2} + \frac{\sqrt{3}t^3\beta^3\gamma}{8\lambda^3\xi} + \frac{1}{8\sqrt{3}\lambda}t\beta\gamma\xi - \frac{1}{4\lambda}t\beta\gamma\varsigma - \frac{1}{4\sqrt{3}}\gamma\xi\varsigma\right) \tag{4.86}$$

$$\xi(t, C, n, \kappa) = \sqrt{\left(\frac{3t^2\beta^2}{\lambda^2} - \frac{162^{1/3}3^{2/3}Ct^3\eta^2(\mu_1+n\mu_2)}{\kappa} + \frac{22^{2/3}3^{1/3}\kappa}{\gamma^2\lambda}\right)} \tag{4.87}$$

$$\kappa(t, C, n) = \left(-9C\,t^5\beta^2\gamma^4\eta^2(\mu_1 + n\mu_2 2) + \sqrt{3}\sqrt{C^2t^9\gamma^6\eta^4(\mu_1 + n\mu_2 2)^2(27t\beta^4\gamma^2 + 256C\eta^2\lambda^3(\mu_1 + n\mu_2))}\right)^{\frac{1}{3}} \tag{4.88}$$

$$\varsigma(t, C, n, \xi) = \sqrt{\left(\frac{t^2\beta^2}{2\lambda^2} + \frac{4\left(\frac{2}{3}\right)^{1/3}C\,t^3\eta^2(\mu_1+n\mu_2)}{\kappa} - \frac{\kappa}{2^{1/3}3^{2/3}\gamma^2\lambda} + (\sqrt{3}t^3\beta^3)/(2\lambda^3\xi)\right)} \tag{4.89}$$

Substituting the term in equations 4.85 to 489 into 4.84 using the relations defined earlier gives the general analytical equation for mean crush force of multi-corner multi-cell tubes as

$$P_m = \frac{\sigma_0 t}{\square b_{eq} H_{eq}} \left(A\, b_{eq}^{\,2} H_{eq} + B\, H_{eq}^{\,2} t + K\, b_{eq} H_{eq}^{\,2} + F\, b_{eq} C t + G\, b_{eq} n C t \right) \quad (4.90)$$

where C is the internal tube flange length, n is the ratio of external tube flange by internal tube flange length and $\varrho = 0.73$ based on equation 4.72. Other constants for each configuration are listed in table 4.2

Table 4.2

Constants in equations 4.85 to 4.90

	C2C	*C2W*	*W2C*	*W2W*
μ_1	*1.8403*	*-0.7623*	*-189.7430*	*10.6814*
μ_2	*10.7261*	*20.1508*	*604.0790*	*63.4602*
λ	*0.8284*	*4.0000*	*113.1370*	*38.6274*
β	*34.2118*	*86.7882*	*1101.8800*	*367.2940*
γ	*9.2457*	*17.9513*	*12.5951*	*20.1101*
η	*8.5529*	*10.8485*	*3.4434*	*5.7390*
A	*9.2457*	*17.9513*	*25.1902*	*40.2201*
B	*8.5529*	*10.8485*	*6.8868*	*11.4779*
K	*0.2071*	*0.5000*	*0.7071*	*1.2071*
F	*0.4601*	*-0.0953*	*-1.1859*	*0.3338*
G	*2.6815*	*2.5189*	*3.7755*	*1.9831*

It is worth mentioning that the equivalent energy flow stress is calculated from equation 4.53, which assumes that the material behaves as isotropic hardening material. This assumption also indicates that the strain values in the localized plastic regions are assumed to be uniform and identical.

4.4.1 Comparison of P_m and H with FEA results

Figure 4.13 illustrates the variation of mean crush force of the four multi-cell tube models from both the analytical equations and FEA simulation for different thicknesses. Very close agreement is seen between the results in these cases. As discussed earlier, the analytical equation is valid as long as the mode shape of deformation does not alter. Crush mode is mainly dependent on the initial imperfection or trigger mechanism and wall thickness compared to the flange size or C/t. This puts a limitation on the analytical equation and in the case of altering crush modes, the analytical equation needs to be revised. The average value for the equivalent projected fold length H from table 2.1 is compared with to H_{eq} from analytical equation in table 4.3. The results differ within 1% to 17%.

Table 4.3

Comparison of equivalent projected fold length (*H*) derived from analytical approach and FE analysis

Heq (mm)	
Equation 4.86	*FEA*
10.7	*10.6*
7.1	*6.3*
8.6	*9.7*
4.8	*5.8*

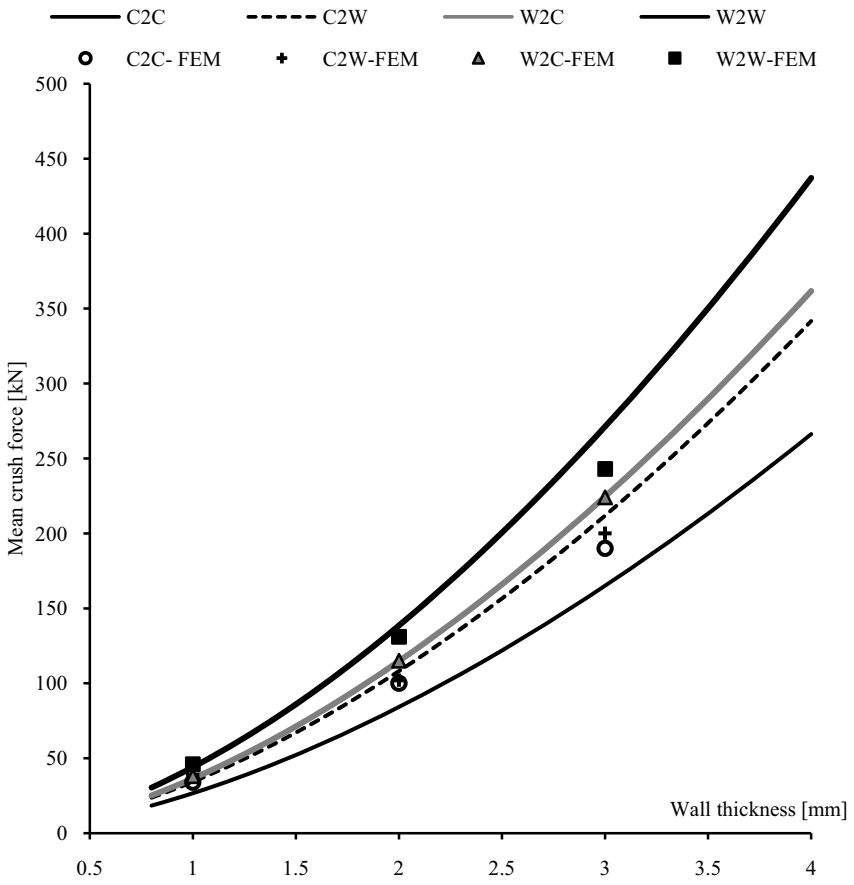

Figure 4.12

Comparison between the mean crush force from analytical and FEA simulation for different thicknesses

4.4.2 Sensitivity of P_m with parameters

As noted previously, the value of mean crush force in analytical equation is highly dependent upon choosing the proper value for the effective crush distance and energy equivalent flow stress. The effect of ϱ parameter for C2C configuration within the range of 0.6 to 0.75 is plotted in figure 4.14. This behavior has been observed for all configurations. As the thickness increases, the effect of ϱ selection becomes more significant.

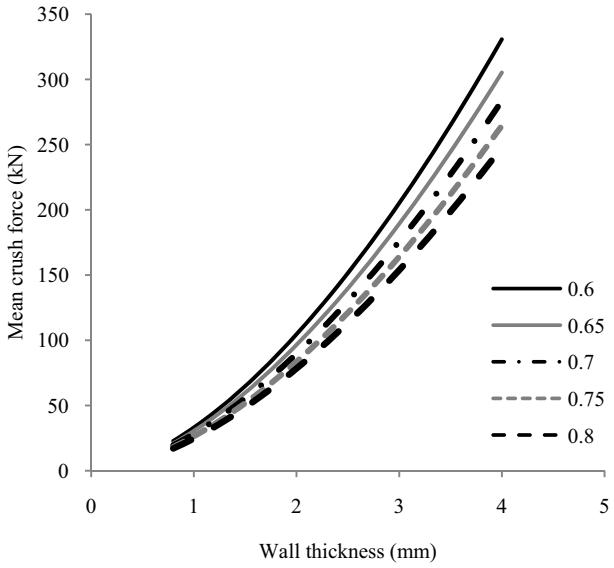

Figure 4.13

Effect of ϱ parameter on the mean crush force

The influence of energy equivalent flow stress on the mean crush force of C2W configuration is shown in figure 4.15. Similar to the effect of effective crush distance, due to the linear relationship between mean crush force and energy equivalent flow stress, increasing the thickness increases the difference between mean crush force predictions.

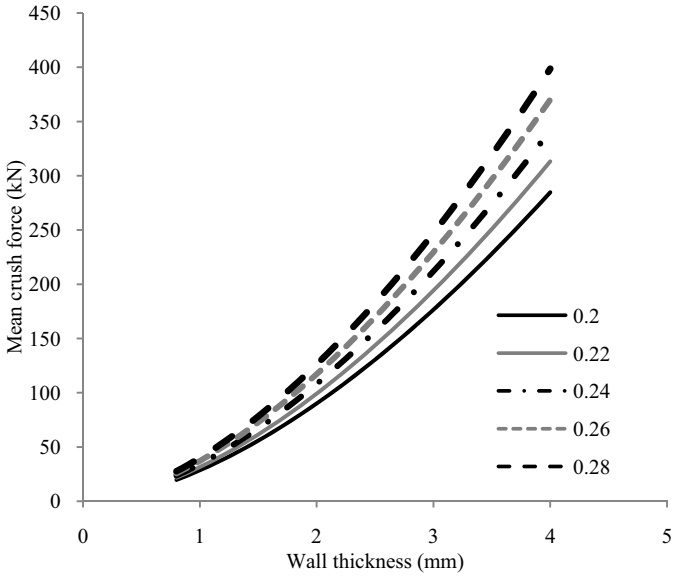

Figure 4.14

Effect of energy equivalent flow stress on the mean crush force

It is seen that the calculation of mean crush force is highly dependent on the proper selection of effective crush distance and energy equivalent flow stress. However, specifying a proper effective crush distance becomes difficult in multi-cell tubes. Energy equivalent flow stress can be specified more accurately by identification of strain in each separate localized region separately. As discussed earlier, including Baushinger effect also improves the performance of the analytical approach presented here.

4.4.3 Comparison with existing models

Chen and Wierzbicki (Chen 2001) and Zhang and Cheng (Zhang 2007) studied the performance of multi-cell tubes for energy absorption. The main feature of the multi-cell tubes they considered that they have equal-sized cells with right angle corners. The simulation-based results for average crush force are compared with the analytical predictions for W2W configuration that has right angles in Table 4.4. The analytical

models in Chen and Wierzbicki (Chen 2001) and Zhang et al. (Zhang 2006) were applied to single-cell and multi-cell tubes with the intersecting walls having an orthogonal arrangement.

For the application of Chen and Wierzbicki equation, model W2W configuration divided into *m* separate flanges with the material cross-sectional area denoted as A resulting in the average crush force formula: $P_m = \left(\frac{2}{3}\right)\sigma_0 t\sqrt{\pi\, m\, A}$. For the Zhang et al.'s equation, with the number of two-flange elements denoted as N_1 and three-flanges as N_2 (for T shape), the formula for the average crush force becomes $\mathrm{P_m} = \sigma_0 \mathrm{t}\sqrt{(\mathrm{N_1} + 2\mathrm{N_1})\pi \mathrm{t}\, \mathrm{L_c}}$. It is worth noting that the energy-equivalent flow stress in Zhang et. al study is derived from $\sigma_0 = \sqrt{\sigma_y\, \sigma_u/(1+\mathrm{n})}$ where σ_y and σ_u represent the yield strength and ultimate stress of the material, respectively, with *n* as the exponent of the power law that seems to underestimate the actual energy equivalent flow stress of the material. They have also mentioned that it is required to use a dynamic correction factor of 1.2 to 1.4 which that seems inappropriate because of the presence of trigger mechanism and the rate independent material.

Table 4.4

Comparison between mean crush force calculation based on present study and that of shown in Chen and (Chen, 2001), and Zhange et al. (Zhang 2006) for W2W model

	Chen& Wierzbicki	Zhang et. al	Present study	Simulation
P_m	120	105	138	131
P_m-difference (%)	8.40%	19.85%	5.34%	N/A
H_{eq}	9.4	8.6	4.8	5.8
H_{eq}- difference (%)	62.07%	48.28%	17.24%	N/A

4.4.4 Dynamic effect

As described in section 4.3.1 the effect of strain rate sensitivity is applied based on Symonds-Cowper (Symonds 1965) to modify the energy equivalent flow stress. Therefore, equation 4.90 will be modified using equation

$$P_{md} = \frac{\sigma_0\, t}{\varrho b_{eq} H_{eq}}\left(1 + \left(\frac{h\, V_0}{4\, b\varrho HD}\right)^{1/p}\right)\left(A\, {b_{eq}}^2 H_{eq} + B\, {H_{eq}}^2 t + K b_{eq} {H_{eq}}^2 + F\, b_{eq} C t + G\, b_{eq} n C t\right) \tag{4.91}$$

Since in this research particular attention paid on the aluminum alloys, these materials are approximately rate independent. Hence, the mean crush force of the dynamic and static loading is almost equal.

4.5 Summary

In this chapter, the analytical calculation of mean crush force for a single-cell tube based on the super folding element theory was described in detail. A comprehensive description of the application of the upper-bound theorem for mechanics of plastic collapse in terms of super folding element was also provided. Inspired by upper bound theorem, the analytical solution procedure for mean crush force was classified by defining the system energy balance in terms of the external work and plastic energy dissipation, defining a kinematically admissible deformation, internal energy contributions of each localized region defined in kinematics, constitutive equation, extermum condition of energy equation and effective crush distance. Different features, key assumptions, range of validity and proof of the minimization of crush force were described. Deformation pattern of corner elements was presented by identification of

basic deformation pattern within observed in the finite element analysis. The deformation pattern can be highly affected by the configuration of trigger mechanism. Thus, kinematics of deformation should be reconsidered once the initial perturbation changes. Results showed a very good agreement between analytical method and finite element analysis. The assumptions and capabilities for the energy absorption characterization in FEA and super folding element (SFE) approach were comparable. Some of the important features of these methods in the context of energy absorption are listed in table 4.5. Based on the results of previous chapters and the experimental observations, dynamic load can change the crush behavior of tubes. Effect of strain rate sensitivity can be added to the developed analytical equation provided that the mode of deformation remains the same. Inertia effect or stress-wave propagation that mainly affects the crush mode and increases the crush mode at the beginning of crush process cannot be captured within this framework. It has been observed that in high velocities effective crush distance is reduced. Comparison between mean crush force of multi-cell tubes from analytical equation and simulation showed a very good agreement. It also was able to predict the trend of mean crush force in different thicknesses and different configurations. A sensitivity analysis on two major parameters including energy equivalent flow stress and effective crush distance showed that the mean crush force is too sensitive to changes in these two parameters. These parameters can vary in different cross-sectional geometries. Similar to kinematically admissible deformation, these parameters should be assigned and cannot be determined from the solution.

Table 4.5

Comparison between finite element simulation and analytical method for energy absorption characterization

	FEA	SFE
Material behavior	Piecewise linear isotropic hardening with J2 plasticity.	energy equivalent flow stress with rigid perfectly plastic model
Rate dependency	Cowper-Symonds equation modifies the yield in each element	Cowper-Symonds equation modifies the energy equivalent flow stress
Kinematics	Kinematic of deformation is predicted from solving differential equations based on defined base-function within each element	Kinematic of deformation needs to be known based on experiment/simulation analysis of deformation history
Energy dissipation	Calculated in each element based on actual relation of stress strain behavior. Integration points consider the stress distribution through shell thickness. First-order shear deformation theory used with shear correction factor of 0.833	Calculated based on the defined kinematics and single value of energy equivalent flow stress
Lobe contact	Imposed by penalty algorithm as constraint on the element penetration	aIs modeled by defining the effective crush distance
Crush force	Contact force	Directly from the energy balance equation
Crush distance	Stroke advancement	Effective crush distance
Wave propagation	Can be captured	Cannot be captured
Solution	Nonlinear explicit solver of governing equation. Implicit solver for plasticity model	Algebraic analytic solution
Error sources	Round off, hourglass, element density, element distortion,	Averaging kinematic parameters H_{eq} and b_{eq} on the multi-cells, energy equivalent flow stress. Nonuniform distribution of strain is ignored Ratio of the effective crush distance
Capability	Ability to model the actual boundary value problem, crush mode identification, dynamic and quasi static, contact definition	Rapid evaluation of design concepts. Identification of the mechanism of deformation

CHAPTER V

SUMMARY AND CONCLUSIONS

The energy absorption behavior of thin-walled, multi-corner tubes under axial compression was investigated using both numerical and analytical approaches. Moreover, the effects of different factors such as: shell element formulation, trigger mechanism, inelastic behavior, cross-sectional geometry, and dynamic loading and loading rate sensitivity were examined.

The results of explicit nonlinear quasi-static finite element analysis with commercial software (LS-DYNA) showed that both the crush mode and crush load of single-cell multi-corner tubes were affected by the choice of shell element formulation. Among those that provided converged solution, the element formulation of Hughes-Liu and Belytschko-Tsay offered the best performance. The results also indicated that a minimum of three integration points through the shell thickness was required to obtain a converged solution. The addition of trigger mechanism as well as is location could help reduce the second peak load. It was shown that low failure strain can affect the mean crush force very considerably. Increasing material hardening increased the crush force. Toughness was found to only affect the crush force when the inelastic region of stress-strain curve has a higher yield stress and steeper hardening modulus. Crush force fluctuation was found to be directly influenced by wall thickness such that increasing the thickness leads

to greater fluctuation. It was found that the effective crush distance was due to double bending. Stress-strain response evaluation showed that the material experiences both loading and unloading during the process of progressive collapse.

The result of nonlinear transient dynamic FEA showed that the shell element formulation can influence the collapse mode of single-cell, multi-corner tubes. The effect of trigger mechanism was observed on the magnitude of the second peak in crush force-crush distance plot. It was observed that without a trigger mechanism, crush force is slightly higher than in the case with trigger mechanism at the initial stages of crushing. This behavior is mainly because the buckling load in the tubes with no trigger is higher than the load required to crush a tube with trigger mechanism. Collapse mode was found to change with thickness, especially in the cases without trigger mechanism. It was also observed that thin-walled, single-cell tubes can show mixed deformation mode. However, the collapse mode could be stabilized in high energy modes, such as the symmetric mode, by increasing the wall thickness. Increasing the initial velocity of striking mass increased the crush force considerably. The inclusion of rate-sensitivity parameters indicated that the crush force was highly affected under dynamic loading.

The effect of cross-sectional geometry on the energy absorption was studied by analyzing several multi-cell multi-corner tube models. The geometric features of interest included the arrangement of the interior tube walls and their connectivity with the exterior tube walls that resulted in acute or obtuse angles. FE simulation results showed that the multi-cell tubes have less crush-force fluctuation than a single-cell tube of equal mean crush force. Detailed evaluation of crush mode and folding length in each wall showed a more complex deformation pattern in multi-cell configurations due to different

corner angles, number of webs connected at each corner and the size of each web. The actual and projected fold lengths were different because of these factors. The energy absorption of multi-cell tube models proposed here was found to be superior to those with multiple rectangular cells based on the results of dynamic and quasi-static loading conditions.

Inspired by the upper-bound theorem, the analytical solution procedure for mean crush force was presented by considering the mechanics of plastic collapse and the super folding element theory. The analytical procedure required the system energy balance between the external work and plastic strain dissipation, defining a kinematically admissible deformation, internal energy contributions of each localized region defined by the kinematics of collapse, constitutive equation, extermum condition of energy equation and effective crush distance. Different features, key assumptions, range of validity and proof of the minimization of crush force were described. It was shown that the analytical method developed here is highly dependent on the accurate mathematical description of kinematically admissible deformation, which, as indicated by FE simulation results, can change due to existence and the type of trigger mechanism used. Plastic work in each localized region was defined based on uniaxial stress that was dominant in each region. As was observed in the FE simulation results obtained here and the experimental observations reported in the literature, dynamic loading can change the crush behavior of multi-corner tubes. To include the effect of strain rate sensitivity in the analytical equation, the mode of deformation must remain the same. The inertia effect or stress-wave propagation that mainly affect the crush force and increases the crush mode at the beginning of crush process cannot be captured within the analytical framework. It was

also observed that in high velocities (40m/s), effective crush distance can be reduced. The comparison between mean crush force of multi-cell tubes found from the analytical equation and that based on FE simulation showed a very good agreement. The analytical model was also able to predict the trend in mean crush force for different thicknesses and different cross-sectional configurations. A sensitivity analysis on two major parameters including energy-equivalent flow stress and effective crush distance showed that the mean crush force was highly sensitive to changes in these two parameters, which can vary in different cross-sectional geometries. Similar to kinematically admissible deformation, these parameters should be assigned a priori as they cannot be determined from the solution.

The closed form crush force formula together with nonlinear transient dynamic FE simulations were used to study the influence of cross-sectional geometry on the crush characteristics of multi-cell multi-corner tubes made of ductile materials. Force-displacement response, crush pattern, and crush distance for different multi-cell, multi-corner models were also investigated.

5.1 Future work

Despite the extensive research dedicated to energy absorption characterization of thin-walled tubes over several decades, many questions still remain. For instance, both the initial imperfection and trigger mechanism could change the behavior and performance of multi-corner tubes. Therefore, a study on a wider range of trigger mechanisms would be useful for design of efficient energy absorbing components and a broader exploration of possible crush modes.

Since failure and damage can have a large influence on the energy absorption capacity and performance of thin-walled tubes, a future investigation of failure and damage could provide important information.

As was shown in this study, material behavior in inelastic regime plays an important role in crush behavior of multi-corner tubes. The inclusion of physics based constitutive models in FE simulations could provide a very broad opportunity for material-process or material-process-product design. Understanding the relation between microstructural features and material behavior such as yield, hardening, recovery, Baushinnger effect, strain rate effect and plastic heating could enable designers to explore new materials and manufacturing processes to improve the crush performance of thin-walled tubes.

A very limited set of experimental data is available for multi-cell metallic tubes. It would be crucial to have test data to physically identify the features of these designs, especially in compatibility regions.

All of the proposed topics listed above are intended to enhance the capabilities of computer-based analysis tools that can be used for energy absorption evaluation of different tube models. The next step in this research is the coupling of such analysis tools with numerical design optimization, which is currently in progress.

REFERENCES

Abramowicz, W. "Extermal Paths In Progressive Plasticity." *International Journal of Impact Engineering* 18, no. 7-8 (1996): 753-764.

Abramowicz, W. "The Effective Crushing Distance in Axially Compressed Thin-walled Metal Columns." 1, no. 3 (1983): 309-317.

Abramowicz, W. "The Effective Crushing Distance in Axially Compressed Thin-walled Metal Columns." *International journal of Impact Engineering* 1, no. 3 (1983): 309-317.

Abramowicz, W. "Thin-Walled Structures As Impact Energy Absorbers." *Thin-Walled Structures* 41, no. 2-3 (2003): 91-107.

Abramowicz, W., Jones, N. "Dynamic Axial Crushing of Square Tubes." *International Journal of Impact Engineering* 2, no. 2 (1984): 179-208.

Abramowicz, W., Wierzbicki,T. "Axial Crushing of Multicorner Sheet Metal Columns." *Journal of Applied Mechanics* 56 (1989): 113–120.

Alexander, J.M. "An Approximate Analysis of the Collapse of Thin Cylindrical Shells Under Axial Loading." *The Quarterly Journal of Mechanics and Applied Mathematics* 13, no. 1 (1960): 10-15.

Bathe, K.J. *Finite Element Procedures (Part1-2).* Prentice Hall, 1995.

Belytschko, T., Neal M.O. "Contact-Impact By The Pinball Algorithm With Penalty Projection and Lagrangian Methods,"." *International journal of Numerical Methods in Engineering* 31 (1991): 547–572.

Belytschko, T., Liu, W.K., Moran, B. *Nonlinear Finite Elements for Continua and Structures.* New York: John Wiley & Sons, 2000.

Bower, A.F. 2008. http://www.solidmechanics.org/.

Calladine, C.R. *Plasticity for Engineers: Theory and Applications.* Horwood Publishing Ltd, 2000.

Calladine, C.R., English, R.W. "Strain Rate and Intertia Effects in the Collapse of Two Types of Energy-Absorbing Struture." *International Journal of Mechanical Sciences* 29, no. 11-12 (1984): 689-701.

Chen, W., Wierzbicki, T. "Relative Merits of Single-Cell, Multi-Cell and Foam-Filled Thin-Walled Structures in Energy Absorption." *Thin-Walled Structures* 39, no. 4 (2001): 287-306.

Chung, T.E., Lee, Y.R., Kim, C.S., Kim, H.S. "Design of Aluminum Space Frame for Crashworthiness Improvement." *SAE international.* 1996. 960167.

de Kanter, J.L.C.G. "Energy Absorption of Monolithic and Fiber Reinforced Aluminum Cylinders." PhD dissertation, Delft University of Technology (TUDelft), The Netherlands, 2006.

DiPaolo, B.P., Monteirob, P.J.M., Gronsky, R. "Quasi-Static Axial Crush Response of a Thin-Wall, Stainless Steel Box Component." *International Journal of Solids and Structures* 41, no. 14 (2004): 3707-3733.

Dipaolo, B.P., Tom J.G. "A Study on an Axial Crush Configuration Response of Thin-Wall, Steel Box Components : The Quasi-Static Experiments." *International journal of solids and structures* 43, no. 25-26 (2006): 7752-7775.

Dunne, F., Petrinic, N. *Introduction to Computational Plasticity.* Oxford University Press, 2005.

Faruque, O., Saha, N. "Extruded Aluminum Crash Can Topology for Maximizing Specific Energy Abdorption." SAE technical paper series, 2008.

Halquist, J. "LS-DYNA Theoretical Manual." Livermore Software Technology Corporation, 1998.

Halquist, J. "LS-DYNA User's Manual version 971." Livermore Software Technology Corporation, 2006.

Hanssen, A.G., Langseth, M., Hopperstad, O.S. "Static and Dynamic Crushing of Square Aluminum Extrusions With Aluminum Foam Filler." *International Journal of Impact Engineering* 24, no. 4 (2000): 347-383.

Hayduk, R.J., Wierzbicki T. "Extensional Collapse Modes of Structural." *Computers and structures* 18, no. 3 (1984): 447-458.

Heinbockel, J.H. *Introduction to Tensor Calculus and Continuum Mechanics.* Trafford Publishing, 2001.

Hiermaier, S.J. *Structures under Crash and Impact Continuum Mechanics, Discretization and Experimental Characterization.* Springer, 2008.

Hill, R. *The Mathematical Theory of Plasticity* . Oxford University Press, 1998.

Holzapfel, G.A. *Nonlinear Solid Mechanics: A Continuum Approach for Engineering.* Wiley, 2000.

Hughes, T. J. R.,. " Nonlinear Dynamic Finite Element Analysis of Shells, Nonlinear Finite Element Analysis in Structural Mechanics, ." *Proceedings of the Europe-U.S. Workshop, Ruhr-Universitat Bochum,* . Germany, 1981. 151-168.

Hughes, T.J.R. *Finite Element Method - Linear Static and Dynamic Finite Element Analysis.* Prentice-Hall, Englewood Cliffs, 2000.

Jones, N. *Structural Impact.* Cambridge University Press, 1998.

Jones, N. "Several Phenomena in Structural Impact and Structural Crashworthiness." *European journal of mechanics. A. Solids* 22, no. 5 (2003): 693-707.

Jones, N., Wierzbicki, T. *Structural Crashworthiness.* Butterworths, 1983.

Karagiozova, D. "Dynamic Buckling of Elastic-Plastic Square Tubes under Axial Impact. Part I - Stress Wave Propagation Phenomenon." *International Journal of Impact Engineering* 30 (2004a): 143-166.

Karagiozova, D., Jones, N. "Dynamic Buckling of Elastic-Plastic Square Tubes under Axial Impact. Part II – Structural Response." *International Journal of Impact Engineering* 30 (2004b): 167-192.

Karagiozova, D., Alves, M. "Dynamic elastic-plastic buckling of structural elements: A review." *Applied Mechanics Reviews* 61, no. 4 (2008): 040803-1 – 040803-26.

Kim, H. S., Chen W., and Wierzbicki T.,. "Weight and Crash Optimization of Foam-Filled Three-Dimensional “S” Frame." *Computational Mechanics* 28 (2002): 417-424.

Kim, H.S. "New Extruded Multi-cell Aluminum Profile for Maximum Crash Energy Absorption and Weight Efficiency." *Thin-Walled Structures* 40, no. 4 (2002): 311-327.

Kokkula, S. "Bumper Beam-Longitudinal System Subjected to Offset Impact Loading An Experimental and Numerical Study." PhD Thesis, Department of Structural Engineering, Norwegian University of Science and Technology, 2005.

Langseth, M., Hopperstad, O. S. "Static and Dynamic Axial Crushing of Square Thin-Walled Aluminum Extrusions." *International Journal of Impact Engineering* 18, no. 7-8 (1996): 949-968.

Lindberg, H.E., Florence A.L. *Dynamic Pulse Buckling: Theory and Experiment.* M. Nijhoff, 1987.

Lu, G., Tongxi, Y. *Energy Absorption of Structures and Materials.* Woodhead Publishing, 2003.

Lubliner, J. *Plasticity Theory.* Dover Publications, 2008.

Mahmood, H.F., Aouadi, F. "Characterization of Frontal Crash Pulse." *Crashworthiness, Occupant Protection, and Biomechanics in Transportation Systems.* AMD-Vol. 246/BED-Vol49, 2000.

Meguid, S.A., Attia, M.A., Stranart, J.C., Wang W. "Soultion stability in the dynamic collapse of square aluminium columns." *International journal of impact engineering* 34 (2007): 348-359.

Mohr, D, Wierzbicki, T. "Crushing of Soft-Core Sandwich Profiles: Experiments and Analysis." *International journal of mechanical sciences* 45, no. 2 (2003): 253-271.

Mohr, D., Mulalo, D. "Deformation Induced Folding Systems in Thin-Walled Monolithic Hexagonal Metallic Honeycomb." *International journal of solids and structures*, 2004: 3353-3377.

Najafi, A., Rais-Rohani, M. "Influence of Cross-Sectional Geometry on Crash Characteristics of Multi-Cell Prismatic Columns." *49th AIAA/ASME/ASC/AHS/ASC Structures, Structural Dynamics and Materials Conference.* Schaumburg, IL., 2008.

Ottosen, N.S., Ristinmaa, M. *The Mechanics of Constitutive Modeling.* Elsevier, 2005.

Otubushin, A. "Detailed Validation of A Non-Linear Finite Element Code Using Dynamic Axial Crushing of A Square Tube." *International Journal of Impact Engineering* 21, no. 5 (1998): 349-368.

Rais-Rohani, M., Solanki, K.N., Eamon, C. "Reliability-Based Optimization of Lightweight Automotive Structures for Crashworthiness." *11th AIAA/ISSMO Multidisciplinary Analysis and Optimization Conference, Portsmouth, VA*. 2006.

Reddy, J. N. *Introduction to the Finite Element Method.* McGraw-Hill, 1993.

Reid, J. D. "Towards the Understanding of Material Property Influence on Automotive Crash Structures." *Thin-Walled Structures* 24, no. 4 (1996): 285-313.

Reid, S.R., Reddy, T.Y., Gray, M.D. "Static and Dynamic Axial Crushing of Foam-Filled Sheet Metal Tubes." *International Journal of Mechanical Sciences* 28 (1986): 295–322.

Santosa, S. P. "Crash Behavior of Box Columns Filled with Aluminum Honeycomb or Foam." Master's Thesis, Mechanical Engineering, MIT, Cambridge, MA, 1997.

Santosa, S. P. "Crashworthiness analysis of Ultralight Metal Structures." Ph.D. Dissertation, Mechanical Engineering, MIT, Cambridge, MA, 1999.

Simo, J.C., Hughes, T.J.R. *Computational Inelasticity.* New York: Springer, 2000.

Symonds, P.S. "Viscoplastic Behavior in Response of Strutures to Dynamic Loading." In *Behavior of Materials Under Dynamic Loading*, by N.J. Huffington, 106-124. ASME, 1965.

VonKarman, T., Duwez, P. "The propagation of Plastic Deformation in Solids." *Journal of Applied Physics* 21 (1950): 987-994.

Wierzbicki, T. "Crushing Analysis of Metal Honeycombs." *International Journal of Impact Engineering* 1, no. 2 (1983): 157-174.

Wierzbicki, T., Abramowicz, W. "On the Crushing Mechanics of Thin Walled Structures." *Journal of Applied Mechanics* 50 (1983): 727-734.

Wierzbicki, T., Recke, L., Abramowicz W., Gholami, T. "Stress Profiles in Thin-Walled Prismatic Columns Subjected to Crush Loading, Part I Compression." *Computers and Structures* 51, no. 6 (1994a): 635-641.

Wierzbicki, T., Recke, L., Abramowicz W., Gholami, T. "Stress Profiles in Thin-Walled Prismatic Columns Subjected to Crush Loading, Part II Bending." *Computers and Structures* 51, no. 6 (1994b): 635-641.

Wierzbicki, T., Schneider, F. "Energy Equivalent Flow Stress in Crash Calculations." Impact and Crashworthness laboratory, MIT, 1999.

Wriggers, P. *Computational Contact Mechanics.* Wiley, 2002.

Zhang, A. N., Suzuki, K., Lixue, C. "Effect of Stiffeners On Quasi-Static Crushing of Stiffened Square Tube With Nonlinear Finite Element." *Journal of Ship Mechanics* 9, no. 4 (2005): 61-68.

Zhang, X., Cheng, G. "A Comparative Study of Energy Absorption Characteristics of Foam-Filled and Multi-Cell Square Columns." *International Journal of Impact Engineering* 34, no. 11 (2007): 1739-1752.

Zhang, X., Cheng, G., and Zhang, H. "Theoretical Prediction and Numerical Simulation of Multi-Cell Square Thin-Walled Structures." *Thin-Walled Structures* 44, no. 11 (2006): 1185-1191.